

INFORMATION TO USERS

This manuscript has been reproduced from the microfilm master. UMI films the text directly from the original or copy submitted. Thus, some thesis and dissertation copies are in typewriter face, while others may be from any type of computer printer.

The quality of this reproduction is dependent upon the quality of the copy submitted. Broken or indistinct print, colored or poor quality illustrations and photographs, print bleedthrough, substandard margins, and improper alignment can adversely affect reproduction.

In the unlikely event that the author did not send UMI a complete manuscript and there are missing pages, these will be noted. Also, if unauthorized copyright material had to be removed, a note will indicate the deletion.

Oversize materials (e.g., maps, drawings, charts) are reproduced by sectioning the original, beginning at the upper left-hand corner and continuing from left to right in equal sections with small overlaps. Each original is also photographed in one exposure and is included in reduced form at the back of the book.

Photographs included in the original manuscript have been reproduced xerographically in this copy. Higher quality 6" x 9" black and white photographic prints are available for any photographs or illustrations appearing in this copy for an additional charge. Contact UMI directly to order.

UMI

**A Bell & Howell Information Company
300 North Zeeb Road, Ann Arbor MI 48106-1346 USA
313/761-4700 800/521-0600**

REACTIVE MELT TRANSPORT IN THE
MANTLE AND PETROGENESIS OF
HAWAIIAN POST-EROSIONAL MAGMAS

by

Peter William Reiners

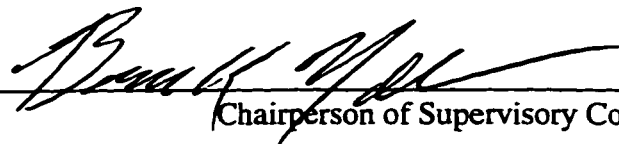
A dissertation submitted in partial fulfillment of the
requirements for the degree of

Doctor of Philosophy

University of Washington

1997

Approved by



Chairperson of Supervisory Committee

Program Authorized
to Offer Degree

Geological Sciences

Date 24 June 1997

UMI Number: 9807021

UMI Microform 9807021
Copyright 1997, by UMI Company. All rights reserved.

**This microform edition is protected against unauthorized
copying under Title 17, United States Code.**

UMI
300 North Zeeb Road
Ann Arbor, MI 48103

© Copyright 1997

Peter William Reiners

Doctoral Dissertation

In presenting this dissertation in partial fulfillment of the requirements for the Doctoral degree at the University of Washington, I agree that the Library shall make its copies freely available for inspection. I further agree that extensive copying of this dissertation is allowable only for scholarly purposes, consistent with "fair use" as prescribed in the U.S. Copyright Law. Requests for copying or reproduction of this dissertation may be referred to University Microfilms, 1490 Eisenhower Place, P.O. Box 975, Ann Arbor, MI 48106, to whom the author has granted "the right to reproduce and sell (a) copies of the manuscript in microform and/or (b) printed copies of the manuscript made from microform."

Signature *Peter Saviers*

Date *24 June 1997*

University of Washington

Abstract

**REACTIVE MELT TRANSPORT IN THE
MANTLE AND PETROGENESIS OF
HAWAIIAN POST-EROSIONAL MAGMAS**

by Peter William Reiners

Chairperson of the Supervisory Committee: Associate Professor Bruce K. Nelson
Department of Geological Sciences

Basaltic magmas reflect the compositions of their mantle sources only to the extent that they have not been modified by melt-mantle reaction during trans-mantle migration. Modeling of reactive melt transport in the mantle, including the effects of diffusive exchange, mineralogic reactions in the solid matrix, and changes in melt fraction provide a series of robust predictions of the geochemical consequences of reactive melt transport on erupted magmas. Two particularly important predictions are: 1) a temporal-compositional trend in cogenetic melt batches emerging from a reactive column of mantle that reflects the gradual exhaustion of the reactive capacity of the solid mantle, and 2) chromatographic decoupling of concentration and isotopic variations of elements with different bulk distribution coefficients in cogenetic melt batches. Chemical and isotopic analyses of stratigraphically-controlled sequences of post-erosional lavas of the Koloa Volcanics on the Hawaiian island of Kaua'i were used to look for evidence of these effects and the possibility that reactive melt transport may explain the strong incompatible-element enrichments in post-erosional magmas. Koloa lavas from individual eruption sequences show systematic trends of decreasing incompatible element concentrations with time. In contrast, incompatible element concentrations throughout multiple eruptions of the entire post-erosional stage show the opposite trend. Excellent inter-element and element-isotope correlations indicate no chromatographic decoupling,

and therefore preclude reactive melt transport as the origin of post-erosional magma compositional variation. Instead, trace-element and Sr- and Nd-isotope variations indicate that post-erosional magmas represent mixtures of melts from a range of mantle sources with different trace-element and isotopic compositions. Magmas with high incompatible element abundances and high La/Lu are derived from mantle sources with relatively enriched isotopic signatures (high $^{87}\text{Sr}/^{86}\text{Sr}$ and low ϵ_{Nd}), while magmas with low incompatible element abundances and low La/Lu are derived from isotopically depleted mantle sources. Systematic temporal-compositional trends within individual eruption sequences probably represents a melt-mixing process, between low-degree melts of relatively isotopically-enriched mantle and high-degree melts of isotopically-depleted mantle, that is associated with melt migration. The overall increase in incompatible element abundance through the entire post-erosional stage on Kauaï probably represents a gradual decrease in the extent of partial melting of the mantle with time.

TABLE OF CONTENTS

LIST OF FIGURES	iv
LIST OF TABLES	vii
INTRODUCTION.....	1
CHAPTER 1: REACTIVE MELT TRANSPORT IN THE MANTLE AND GEOCHEMICAL SIGNATURES OF MANTLE-DERIVED MAGMAS.....	3
ABSTRACT OF CHAPTER 1	3
INTRODUCTION TO CHAPTER 1 AND BACKGROUND.....	4
TYPES OF MELT-MANTLE REACTION.....	7
MODELING REACTIVE MELT TRANSPORT.....	10
Mass-balance incremental method	11
Continuum method	13
Model parameters & assumptions	13
RESULTS: EXAMPLES OF REACTIVE MELT TRANSPORT EFFECTS ON MELT COMPOSITIONS.....	18
Pure diffusive exchange, no mineralogic reaction.....	19
Diffusive-reactive exchange: Lherzolite to dunite at constant ϕ	23
Diffusive-reactive exchange: Lherzolite to pyroxenite at constant ϕ	24
Diffusive-reactive exchange: increasing ϕ with constant matrix mode.....	26
Diffusive-reactive exchange: Decreasing ϕ with constant matrix mode	27
Diffusive-reactive exchange: Lherzolite to dunite with increasing ϕ	27
DISCUSSION: KEY FEATURES OF REACTIVE MELT TRANSPORT	29
The melt front and zone-refining/AFC.....	30
Chromatographic effects.....	31
Mineralogic reaction: Changes in D and ϕ	33

Inferring mantle source characteristics.....	35
The physical characteristics of melt transport.....	38
Geochemical predictions and comparisons to real lava sequences: The need for time-series of monogenetic eruptions.....	40
CONCLUSIONS	44
CHAPTER 2: MELT MIGRATION, REACTION, AND MIXING IN THE MANTLE: ISOTOPIC AND TRACE ELEMENT CONSTRAINTS FROM STRATIGRAPHIC SEQUENCES OF PRIMITIVE, ALKALIC MAGMAS OF KAUA'I, HAWAI'I.....	
ABSTRACT OF CHAPTER 2.....	61
INTRODUCTION TO CHAPTER 2	62
REACTIVE MELT TRANSPORT	64
THE KOLOA VOLCANICS.....	67
RESULTS.....	67
Basin-wide stratigraphic-petrologic relations.....	69
The Palikea breccia member in the Lihue basin.....	70
Trace element and isotopic compositions.....	71
DISCUSSION.....	72
Reactive melt transport.....	74
Mixing of melts from distinct mantle sources.....	76
Temporal trace element trends and the mechanism of melt-mixing.....	82
CONCLUSIONS	84
CHAPTER 3: STRATIGRAPHY AND GEOCHEMISTRY OF VOLCANIC AND DEBRIS-FLOW DEPOSITS OF THE LIHUE BASIN AND EASTERN KAUA'I, HAWAI'I	
ABSTRACT OF CHAPTER 3.....	109
INTRODUCTION TO CHAPTER 3	110
GEOLOGY OF KAUA'I AND THE LIHUE BASIN.....	110

SAMPLE LOCATIONS & ANALYSES.....	114
RESULTS.....	115
Palikea Ridge.....	115
Lihue Basin Drillhole Samples.....	116
DISCUSSION.....	118
Stratigraphic-geochemical trends in the Koloa Volcanics.....	118
Waimea Canyon Basalt lavas near the bottom of the basin	119
CONCLUSIONS	123
BIBLIOGRAPHY	137
APPENDIX A: MASS-BALANCE INCREMENTAL METHOD.....	148
APPENDIX B: CONTINUUM METHOD DERIVATION AND FINITE	
DIFFERENCE SOLUTION	150

LIST OF FIGURES

<i>Number</i>	<i>Page</i>
Figure 1. Physical scenario of reactive melt transport for modeling and mechanisms of melt-mantle trace element exchange.....	47
Figure 2. Model scenarios for two different model methods.	48
Figure 3. ϕ , D , and N_D in the reactive mantle column, for varying values of r	49
Figure 4. Example, purely diffusive exchange.	50
Figure 5. Example, diffusive-reactive exchange: lherzolite to dunite at constant ϕ	52
Figure 6. Example, diffusive-reactive exchange: lherzolite to pyroxenite at constant ϕ ...	54
Figure 7. Example, diffusive-reactive exchange: increasing ϕ , constant mode.....	55
Figure 8. Example, diffusive-reactive exchange: decreasing ϕ , constant mode.....	56
Figure 9. Example, diffusive-reactive exchange: lherzolite to dunite, increasing ϕ	57
Figure 10. Example, diffusive-reactive exchange: lherzolite to pyroxenite, decreasing ϕ	58
Figure 11. Zone-refining.....	59
Figure 12. Inferred REE concentrations of mantle source of melt that has reacted with a large volume of mantle.	60
Figure 13. Example of geochemical predictions of reactive melt transport, with and without mineralogic reaction.	90
Figure 14. Generalized geologic map of Kaua'i.....	92
Figure 15. Stratigraphy of the HTZ drillhole and the Lihue basin.	93
Figure 16. P_2O_5 and TiO_2 (wt.%) in Koloa Volcanics in the Lihue basin.....	95
Figure 17. Concentrations of incompatible elements and ratios of highly to moderately incompatible elements, with respect to stratigraphic position in the HTZ and Lae O Kilauea sections.....	96

Figure 18. Sr- and Nd-isotope compositions of Koloa lavas.....	97
Figure 19. Rare earth element (REE) compositions of Koloa samples and tholeiitic/hawaiitic breccia.....	98
Figure 20. La and Nd concentrations of Koloa lavas.....	99
Figure 21. La and Nd concentrations of Koloa samples and non-modal batch partial melts of garnet lherzolite and pyroxenite.....	100
Figure 22. La and Nd concentrations of Koloa samples and predictions of reactive transport of 5% melt of depleted mantle through similar depleted mantle matrix.....	101
Figure 23. P ₂ O ₅ and La/Lu versus ⁸⁷ Sr/ ⁸⁶ Sr and ε _{Nd} of samples with predictions of the reactive transport model.....	102
Figure 24. La and Nd concentrations of Koloa lavas with partial melting trends of depleted lherzolite, pyroxenite, and enriched lherzolite, and melt-mixing trends.....	103
Figure 25. P ₂ O ₅ and La/Lu versus ⁸⁷ Sr/ ⁸⁶ Sr and ε _{Nd} of samples with predictions of melt- mixing using melts derived from incompatible element-depleted mantle sources.....	104
Figure 26. Th and Sr concentrations of lavas from the Koloa and Honolulu Volcanics.	105
Figure 27. La/Lu versus ⁸⁷ Sr/ ⁸⁶ Sr of Koloa lavas and post-erosional, post-shield alkalic, and tholeiitic lavas from Haleakala and Koolau volcanoes.....	106
Figure 28. ⁸⁷ Sr/ ⁸⁶ Sr and ε _{Nd} of Koloa magmas versus P ₂ O ₅ (wt.%) and La/Lu, with melt- mixing trends, enriched mantle sources.....	108
Figure 29. Generalized geologic map of Kaua'i.....	127
Figure 30. Landsat MSS image of Kaua'i.....	128
Figure 31. Photomicrographs of breccia samples from the Lihue basin and Palikea ridge.....	129

Figure 32. Major-element compositions of samples from Palikea ridge and the Lihue basin drillholes.....	131
Figure 33. P_2O_5 and TiO_2 versus stratigraphic position for Koloa lavas in each drillhole.....	132
Figure 34. Generalized stratigraphic section of the Lihue basin.....	133
Figure 35. Sr- and Nd- isotope compositions of Kaua'i lavas.....	134
Figure 36. Detailed stratigraphy of the HTZ drillhole, Lihue basin.....	135
Figure 37. Photomicrograph of alkali gabbro from one of the intrusive bodies at Puu Lua, on the west rim of Waimea Canyon.....	136

LIST OF TABLES

<i>Number</i>	<i>Page</i>
Table 1. Parameters used in reactive transport modeling.....	46
Table 2. Major- and trace-element and isotopic compositions of samples from the HTZ drillhole, Lihue basin, Kaua'i.....	86
Table 3. Major- and trace-element and isotopic compositions of samples from Lae O Kilauea vent, Kaua'i.....	88
Table 4. Melting and melt-mixing model parameters.	89
Table 5. Major element compositions of Lihue basin drillhole and Palikea Ridge Breccia Samples	124
Table 6. Isotopic compositions of Lihue basin and Waimea Canyon Basalt samples	126

ACKNOWLEDGMENTS

I would like to acknowledge a number of individuals and groups for their logistical and technical help with this study, including Richard Volk of the Kilauea Point National Wildlife Refuge for allowing me to access and sample the Lae O Kilauea vent on Kauaī. Peter Mouginis-Mark and NASA's Virtually Hawaii Program for permission to use the Landsat MSS image of Kauaī in several places including this dissertation, Dottie Beakert and Jeff-the-pig-hunter for valuable help in accessing and navigating the jungle of the western Lihue Basin, and Sven Maaløe for kindly sending me a large number of geochemical data on the Koloa Volcanics. I am also very grateful to Dave Everitt and Steve Thompson for courageous and loyal help in the field, and apologize again to Steve for adjusting the position of his nose on the Palikea breccia.

I am very grateful to those groups that have provided financial assistance to my scholarship, lab research, field work, and morale. I would like to thank the Geological Society of America for several generous grants, including two H.T. Stearns Fellowships, that made much of this field work possible. The University of Washington Department of Geological Sciences deserves great thanks for their generous support of this research, especially through the Graduate Research Fund, and the David Johnston, Howard Coombs, Peter Misch, and Livingston Wernicke Awards.

I am grateful to a number of individuals for their academic help, advising, and enthusiasm. First on this list is my advisor, Bruce Nelson, for all of his help and support throughout my graduate career, and for teaching me how to pitch scientific ideas. Also thanks to the members of my committee: Mark Ghiorso, George Bergantz, and Stu McCallum, for their help and advice over the years. I gratefully acknowledge the help of Dave McTigue in modeling transport processes, Jerry Hinn for expert and patient help in

isotope analyses, and valuable camaraderie, and Scott Kuehner for valuable petrologic discussions through the years. Thanks to a number of volcanologists and geologists for introducing me to, and helping me interpret, Hawaiʻian geology, namely Scot Izuka, Don Swanson, Robin Holcomb, and Dave Clague.

My fellow graduate student, "big-idea-sounding-board," and friend Nuni Anders deserves credit for introducing me to Hawaiʻian geology in the wilds of Waianae; her hard work and enthusiasm paved the way for our group to study Hawaiʻian problems. I gratefully acknowledge the graduate students at U.W. who have helped me in many ways through the years--just some of them are: Kevin Schmidt, Sarah Konrad, John Buffington, Scott Barboza, Juliet Crider, Leon Sawyko, Steve Macias, Kari Cooper, Erich Cowgill, Justin Casserly, Seth Moran, Ken MacLeod, and Marc Hirschmann. I would like to thank my parents, Bill and Norma Reiners for their continuous support and faith in me, and for being discrete while photographing me in front of my AGU posters. Finally, thanks to Juliet McKenna for all the support, confidence, and inspiration she has given me over the last several years. Her patient tolerance of my sometimes misguided ambitions and trivial rants and raves has not gone unappreciated; her unselfish support and understanding serve as a model for me everyday.

INTRODUCTION

This dissertation is structured as three separate but complementary studies organized into three chapters. The first chapter covers the theoretical background and modeling of the process of reactive melt transport in the mantle. Although melt-mantle reaction has been and continues to be a process of considerable interest because of its theoretical potential to strongly affect magma compositions, few studies have outlined its geochemical consequences in the context of potentially observable effects on erupted magmas, and the way in which observations of real lavas may implicate or preclude it as an important petrogenetic process. The end-member models in the first chapter make a number of robust predictions of the effects of reactive melt transport on compositions of erupted magmas, and the conditions under which they may be observed, if the process has occurred.

The second chapter presents the results of a study in which these predictions were used to guide a new way of sampling and analyzing Hawai'ian post-erosional magmas, a type of magma whose geochemical signatures have been suggested to be the result of large extents of melt-mantle reaction. Compositions of post-erosional lava flows from long stratigraphic sequences on Kaua'i were analyzed in order to look for systematic temporal-compositional changes and chromatographic effects in cogenetic lavas. While systematic temporal-compositional trends are observed in magmas from individual eruptions (and in magmas from multiple eruptions over the entire post-erosional volcanic stage), other geochemical features such as the lack of chromatographic decoupling preclude reactive melt transport as an origin for the geochemical signatures of post-erosionals magmas. However, these new data do provide several new rigorous constraints on the petrogenesis of post-erosional magmas. In particular, they indicate two or more distinct mantle source

regions for post-erosional magmas, and lavas from individual eruptions represent mixtures of melts from different sources in systematically varying proportions with time.

The study of long stratigraphic sequences of volcanics in the Lihue basin of Kauaī also provides a number of constraints on the sub-surface stratigraphy and geologic history of the island, and these are presented and discussed in the third chapter. Among other findings, this study showed that there are abundant hawaiite and mugearite lava flows in the subsurface of eastern Kauaī and in the island's central highlands, documenting a more voluminous post-shield alkalic stage than previously recognized. The stratigraphic relations in the basin also indicate that the Lihue basin formed by caldera- or landslide-collapse, not fluvial erosion.

CHAPTER 1: REACTIVE MELT TRANSPORT IN THE MANTLE AND GEOCHEMICAL SIGNATURES OF MANTLE-DERIVED MAGMAS

ABSTRACT OF CHAPTER 1

Geochemical compositions of basaltic magmas reflect the compositions of their mantle sources only to the extent that they have not been modified by reaction with the mantle during melt migration and ascent. Mantle xenoliths and massifs clearly show large compositional changes resulting from reaction with migrating melts, and compositions of some magma types are consistent with theoretical expectations of large amounts of melt-mantle reaction. However, because the effects of melt-mantle reaction on single batches of magma are similar to the effects of small degrees of melting, it is not clear whether compositions of erupted melts are significantly affected by reactive transport. Modeling of reactive melt transport in the mantle, including the effects of diffusive exchange, mineralogic reactions in the solid matrix, and changes in melt fraction provide a series of robust predictions of the geochemical consequences of reactive melt transport. Key predictions of these endmember models are 1) the first melt batch to emerge from a column of reactive mantle in a single transport event should be strongly enriched in incompatible trace elements, and 2) successive melt batches should show a compositional trend reflecting exhaustion of the reactive capacity of the mantle column, generally reflected in decreasing abundances of incompatible elements. Chromatographic effects on trace element abundances (though not isotopic compositions) may also be smoothed or masked by the effects of mineralogic reaction in the form of changing melt fraction or matrix mode. Although these models assume end-member conditions and maximum extents of melt-mantle reaction, if reactive melt transport is an important petrogenetic process that influences trace element compositions of erupted magmas these predictions should be observed in carefully-chosen stratigraphic sections of primitive alkalic magmas

such as post-erosional lavas of Hawai'i. Demonstrating the petrogenetic significance of reactive melt transport requires sampling and analysis that provides detailed temporal-compositional relationships of monogenetic eruptions of such lavas.

INTRODUCTION TO CHAPTER 1 AND BACKGROUND

Basaltic magmas provide the best constraints on the composition of the earth's mantle and the heterogeneities within it by providing chemical information about their mantle sources (e.g., Hofmann, 1997). In addition to mantle source composition however, chemical signatures of primary (unfractionated) basaltic melts are also influenced by the partial melting process that generated them. With some assumptions, theoretical and experimental models of partial melting combined with knowledge of the contrasting behavior of various elements during these processes allow back-calculation of mantle source compositions from magma compositions. At least several fundamentally distinct mantle reservoirs have been recognized and explained in the context of global tectonics and earth differentiation through this method (Weaver, 1991; Hart et al., 1992).

This approach also led to the now generally accepted idea that the two main types of oceanic magmas, tholeiitic and alkalic basalts, despite their geographic and temporal coincidence, are derived from fundamentally different source regions with differing source compositions and histories (Gast, 1968; Kay & Gast, 1973; Sun & Hanson, 1975). Alkalic basalts are distinguished from tholeiites by large enrichments in incompatible elements, a feature that has led most studies to conclude that the source regions for alkalic basalts are correspondingly enriched in incompatible elements relative to depleted or primitive mantle and relative to the source regions of typical tholeiites. Radiogenic isotope studies of most alkalic basalts also further constrain this source enrichment to be relatively recent (less than 100-200 Ma prior to melting). Thus the source regions of alkalic basalts are generally thought to be distinct, and have histories that are distinct from, the source regions of typical tholeiitic magmas.

But this observation of incompatible element enrichment has at least two other possible explanations. If alkalic basalts are the products of very small extents of partial melting (commonly less than 0.2%), instead of the larger extents for tholeiites (typically about 7-15%), then this requirement of a incompatible-element enriched source is obviated (Alibert et al., 1983; Sims et al., 1995; Frey & Roden, 1987). In the past, theoretical difficulties with segregating and extracting such low-degree melts from the mantle however, have led to favor of the special source hypothesis (although several more recent studies (McKenzie, 1989; Riley & Kohlstedt, 1991; Jin et al., 1994) suggest that very low degrees of melting may indeed be realistic). The other possible hypothesis, first put forward some decades ago and essentially untested, is that alkalic melts react with large volumes of solid mantle during melt migration and ascent, and acquire a geochemical signature highly enriched in incompatible elements reflecting equilibration with mantle outside of their source region (Harris, 1957; Green & Ringwood, 1967; Alibert et al., 1983).

Several recent studies have revisited the question of reactive melt transport, demonstrating that in addition to the initial mantle source composition and the extent of partial melting, the dynamics of melt migration processes can strongly influence trace element compositions of mantle-derived magmas (McKenzie, 1984; McKenzie & O'Nions, 1991; Spiegelman, 1996; Navon & Stolper, 1987; Iwamori, 1993a,b; Richter, 1986; Richter & McKenzie, 1984; Nielson & Wilshire, 1993; Kelemen, 1986; Kelemen et al., 1995; Sims et al., 1995; Lundstrom et al., 1995; Bodinier et al., 1990; Spiegelman & Elliott, 1993; Vasseur et al., 1991; Godard et al., 1995; Van der Wal et al., 1996). These studies emphasize that the extent to which melt reacts with solid mantle along the melt migration path can have dramatic effects on magma trace element compositions. The possibility that melt could remain in equilibrium with, or otherwise react with, mantle during ascent raise the possibility that variations styles of melt migration and melt-mantle reaction, rather than, or in addition to mantle source variations and total extents of melting, are responsible for basalt geochemical signatures. Theoretical proposals that the

characteristic incompatible trace element enrichments of alkalic basalts may be due to extensive melt-mantle reaction during melt migration is not new. Most of these studies show that reactive melt transport can dramatically affect melt compositions and illustrate the fundamental ambiguity in inverting mantle source compositions from magma compositions when the details of melt migration are not known. But while many theoretical and modeling-based inroads have recently been made into understanding reactive melt transport, finding direct, measurable effects of melt-mantle reaction on magmas, and thereby evaluating its significance in the origin of their geochemical signatures is problematic.

Mantle xenoliths and massifs worldwide show clear evidence that migration of melt strongly modifies both major and trace element compositions of solid mantle (Hauri et al., 1994; Bodinier et al., 1990; Godard et al., 1995; Van der Wal, 1996; Kelemen et al., 1995; Sen, 1988; Sen et al., 1993; Sen & Leeman, 1991). In ophiolites and other types of massifs, widespread dunite and harzburgite zones and veins can clearly be shown to be former melt migration channels resulting from dissolution of pyroxenes and reprecipitation of olivine (Kelemen et al., 1995a,b; Kelemen & Dick, 1995). Other melt-mantle reaction evidence comes from both modal and trace element modification of mantle adjacent to dikes and veins of minerals precipitated directly from migrating melts (Sen, 1988; Sen & Leeman, 1993; Bodinier et al., 1990; Irving, 1980). But despite widespread evidence that the composition of solid mantle is strongly modified by reaction with migrating melts, it is difficult to relate the compositions of erupted melts to such processes. The question of whether *magma* compositions are significantly affected by reactive melt transport is of great importance, if only because it hampers confident inferences of mantle source compositions.

In this paper, I approach the problem of reactive melt transport in the mantle from an end-member perspective, seeking robust predictions of the geochemical effects of the process on melt compositions. End-member models of several types of reactive melt transport

through the mantle predict a number of spatial-temporal-compositional patterns that should be evident in certain types of magmas, if reactive transport affects melt compositions significantly. These predictions can be used to guide sampling and analytical programs to look for the effects of reactive melt transport on basaltic magmas and thus evaluate its significance in modifying or contributing to magma geochemical signatures.

TYPES OF MELT-MANTLE REACTION

Currently there is considerable debate concerning the significance of reactive melt transport in influencing magma compositions (for illustrative discussion see Navon et al., 1996; Nielson & Wilshire, 1996). Once melt leaves its source region it is out of equilibrium with the surrounding mantle and must react with it to some degree, changing its major and trace element composition in response. The extent of this reaction, and the extent to which it modifies a "primary" magma geochemical signature is unknown. Part of the reason for this is our poor understanding of the physical mechanisms and rates of melt transport in the mantle. Important unknowns are the lengthscales over which melts migrate via porous flow or hydrofracturing in different regions of the mantle and melt velocities either within or outside the melting region. Because each of these factors alone can be expected to strongly affect the efficiency of element exchange with surrounding mantle, it is difficult to rule out the potential for compositional modification during trans-mantle migration from our limited knowledge of the physical mechanisms of melt movement alone. Addressing the question of reactive melt transport requires predicting endmember geochemical consequences of the process on erupted melts and then seeking evidence of these compositional consequences in real melts.

A complete model of geochemical exchange between migrating melt and solid mantle would need to include the effects of a long list of complex factors. Among these would be variable mechanisms of elemental exchange including dissolution and reprecipitation of

minerals in the solid, diffusion of elements into and out of solid grains, within the melt phase, and along grain boundaries, volatile transfer between melt and solid, and propagation of veins of reacting and differentiating melt. Many aspects of the physical characteristics of the melt-solid system also undoubtedly affect the efficiency and style of element exchange, such as the nature of melt movement (e.g., porous flow versus hydrofracturing), melt velocity, solid compaction, and surface area and grain size of reacting solids. Kinetic effects, such as rates of elemental diffusion in both the solid and melt, and dissolution and precipitation rates of minerals, add important temporal considerations to the reaction. Although some models have focused on various aspects of these parameters (Navon & Stolper, 1987; Iwamori, 1993a,b; Vasseur et al., 1991), many of these considerations are difficult to address in a geochemical model of reactive melt transport, and including all of them in a single model would be prohibitively difficult. For these reasons, instead of seeking a detailed model of melt-mantle reaction including as many physical, chemical, and kinetic parameters and variables as possible, it is necessary to adopt simplistic endmember approaches to the problem.

Two exchange mechanisms, two endmember models

Two endmember scenarios of reactive melt transport can be evaluated rather simply by considering two main types of elemental exchange between a column of solid mantle and melt flowing through it (Fig. 1).

The primary mechanisms of trace element exchange between melt and solid mantle during melt migration considered in this study are 1) diffusion of trace elements in and out of solid grains and into and out of the liquid (diffusive exchange, Fig. 1a), and 2) dissolution of minerals from solid and reprecipitation of minerals from melt (reactive exchange, or mineralogic reaction, Fig. 1b). It is worth considering the effects of each of these types of trace element exchange because mantle xenoliths and massifs show evidence for both of these types of exchange mechanisms (Bodinier et al., 1990; Godard et al., 1995; Irving, 1980; Hauri & Hart, 1996), and, as will be shown below, each has

very different effects on melt composition. Additionally, these two different exchange mechanisms, solid diffusion and dissolution/precipitation, occur at very different rates. Typical diffusion rates for trace elements in mantle minerals at near solidus temperatures range from approximately 10^{-11} to 10^{-15} cm²/s (Hart, 1993; Hofmann and Hart, 1978). In contrast, dissolution and precipitation rates for typical mantle minerals near equilibrium with melt range from approximately 10^{-7} to 10^{-10} cm/s (Edwards, 1996; Brearley & Scarfe, 1986).

Diffusive exchange assumes an approach to trace element equilibrium in the melt-solid system dictated by distribution coefficients of each element and driven by concentration gradients in the solid and melt (Fig. 1a). The endmember scenario of diffusive exchange modeled here is that of local equilibrium between the solid and melt at every point in the reactive column at every timestep. This implies that melt is flowing through the solid matrix at a velocity that is small relative to the rate of elemental diffusion in the solid grains.

The other type of exchange modeled here is reactive exchange, where, in addition to diffusive exchange with the solid, the mineralogic mode and melt-fraction of the melt-solid system is changing as a result of dissolution and reprecipitation (reactive exchange). Reactive exchange assumes that trace element exchange is dictated by phase equilibria (Fig. 1b)—dissolution and reprecipitation of certain minerals changes the mode of the matrix and melt fraction of the melt-solid system, repartitioning trace elements between melt and solid. The mineralogic reactions used in this study are modeled after melt-mantle reactions determined from phase equilibria or evidence from xenoliths or massifs.

The two endmember scenarios that are modeled in detail here are: 1) diffusive exchange without mineralogic reaction or change in melt fraction (without reactive exchange), and 2) a combination of diffusive and reactive exchange mechanisms (Fig. 1). The latter could be envisioned as the case where melt is flowing through solid slowly enough to

maintain diffusive equilibrium with the grains, but the mineralogy of the solid also changes, as dictated by phase equilibria.

MODELING REACTIVE MELT TRANSPORT

The modeling presented here seeks to predict spatial and temporal changes in trace element compositions of melt batches migrating through, and emerging from a reactive column of mantle. The physical scenario envisioned is a single, one-dimensional column of reactive mantle through which melt flows, from the bottom to the top of the column. As progressively more melt flows through the column and reacts with the volume of solid mantle in it, the solid begins to reach trace-element (and mineralogic, in some cases) equilibrium with the melt. As this occurs, the extent of melt-solid reaction and compositional modification of any individual batch of melt flowing through the column decreases. This should generate a sequence of melt compositions emerging from the top of the column that show a progressive decrease in melt-mantle reaction effects. This sequence of emerging melt compositions could then serve as a standard with which to compare compositions of real cogenetic lavas erupted during monogenetic eruptions.

The modeling presented here attempts to avoid one significant problem with most previous models of reactive melt transport. Typical models (McKenzie, 1984; Navon & Stolper, 1987; Godard et al., 1995) presume an initial condition of solid matrix with a pre-existing porosity and mineralogy that is filled with melt already in equilibrium with the solid. These models begin with this resident melt being forced up and out of the column by flow of new melt, with a different composition, into the bottom of the column. While this type of conceptualization illustrates some of the main points and geochemical results of reactive melt transport, it neglects the initial infiltration of melt into the mantle column. By beginning the model with the initial infiltration and propagation of the leading melt batch (melt front), two purposes are served. First, it allows one to track the changing composition of the melt front as it reacts with progressively larger volumes of

mantle (the melt front is the first melt to emerge from the column, so knowing how its composition changes with propagation and progressive reaction is critical). Second, since the melt is progressively infiltrated from bottom to top, solid and melt composition, mineralogy, and melt fraction (porosity) in any portion of the column are all a function of integrated melt flux through that portion of the column. Models that begin with a column pre-filled with melt in equilibrium with column solid ignore this.

Two different modeling approaches are outlined here: a mass-balance or incremental method, and a continuum method. Each has advantages and disadvantages. The mass balance method, while approximate and not very elegant, calculates melt and solid compositions during initial melt infiltration into the column. The continuum approach is slightly more elegant, but requires a solution by finite difference methods and presumes a matrix already filled with melt. Combining these two different models in two stages provides a new and useful set of predictions of the geochemical consequences of reactive melt transport on mantle melts. Each of these models also allows for both trace element exchange mechanisms outlined above: diffusive and reactive (mineralogic reaction) exchange.

MASS-BALANCE INCREMENTAL METHOD

This method assumes an initially solid column of mantle with density ρ_s and trace element concentration C_s , infiltrated with melt from below with density ρ_f and concentration C_f (Fig. 2). As the melt propagates upwards into the column it establishes porosity ϕ in the column in a way that could be imagined as either melt pushing open voids in the rock, or shouldering aside portions of the solid rock on either side. Note that porosity here actually refers to the relative volumes of melt and solid in equilibrium within the column--these models make no assumptions about geometry of melt flow its spatial distribution. As the melt migrates through the solid it remains in trace element equilibrium with the solid so that

$$C_s = DC_f \quad (1.1)$$

at every point and time in the column, where D is the bulk solid/melt distribution coefficient. The column is divided up into a series of i one-dimensional cells, and in each of the j timesteps melt advances one cell while the solid remains stationary. Simple mass balance (Appendix A) yields the concentration of an element in the melt in cell i and time step j :

$$C_{f_i}^j = \frac{\rho_f \phi_{i-1}^{j-1} C_{f_{i-1}}^{j-1} + \rho_s (1 - \phi_i^{j-1}) C_{s_i}^{j-1}}{\rho_f \phi_i^j + \rho_s (1 - \phi_i^j) D} \quad (1.2).$$

This equation can be solved for a sequence of cells in a sequence of timesteps to simulate equilibrium transport of melt with an initial concentration C_f^0 , through a column with an initial solid concentration C_s^0 . Similar approaches were taken by Liang & Elthon (1990) and Vollmer (1987) in modeling metasomatic processes on solid mantle compositions.

The simplest case of reactive transport that can be modeled with this equation is one of purely diffusive exchange in the column with constant ϕ and D (no mineralogic reaction, no change in porosity or melt fraction). But this equation also allows for temporally and spatially varying ϕ and D in the reactive column, and thus can be used to simulate mineralogic reaction, via dissolution and reprecipitation (and the accompanying reactive exchange), simultaneously with diffusive exchange.

In models with reactive exchange, D in each cell changes from an initial to a final value, and in any cell is a function of the integrated melt flux through that cell (as more melt flows through and equilibrates with the solid, more of the matrix is changed from the initial to the final modal assemblage). Changing ϕ implies changing melt and solid masses (crystallization or melting) within each cell, and changes uniformly in each cell from an initial to final value in order to conserve mass.

CONTINUUM METHOD

Another way of modeling reactive transport in the melt-mantle column involves a continuum approach, solved by a finite difference method (Appendix B). This scenario requires the assumption of a column of solid mantle with pre-existing porosity ϕ and ratio of solid to melt densities ρ , that is already filled with melt in equilibrium with the solid with bulk distribution coefficient D (Fig. 2). At the first timestep, melt begins flowing through the column (and new melt begins entering the bottom) with a velocity v . The concentration of a trace element in the melt (C_f) at any point and timestep in the column is:

$$\left[\rho(1-\phi)D + \phi \right] \frac{\partial C_f}{\partial t} + \phi v \frac{\partial C_f}{\partial z} = \rho C_f \left[(\phi-1) \frac{\partial D}{\partial t} + (D-1) \frac{\partial \phi}{\partial t} \right] \quad (1.3)$$

This equation was used by Godard et al. (1995) and Van der Wal & Bodinier (1996) for modeling trace element effects of recrystallization fronts on residual solid in mantle massifs. The first term on the left side accounts for diffusive exchange of the trace element between the solid and melt, the second term for advection of the trace element up through the column, and the right side accounts for reactive exchange of the element (changes in ϕ and D). If the ϕ and D do not change during melt flow and exchange is purely diffusive, then the right side of equation 1.3 reduces to zero, and this equation is equivalent to equation 1b of Navon & Stolper (1987). In cases of reactive exchange and changing ϕ and D , the reactions are assumed to proceed as in the incremental mass-balance model.

MODEL PARAMETERS & ASSUMPTIONS

A variety of types of reactive melt transport and the resulting geochemical effects on melts can be illustrated with the models presented above. The simulations presented here are designed to model trace element evolution of melt flowing through, and reacting with.

a one-dimensional column of mantle matrix. Discussion will focus primarily on the trace element compositions of melt batches emerging from this column at different times; changing melt compositions within the column, and the exhaustion of the reactive capacity of the solid mantle with respect to different elements. The temporal-compositional variation of melts emerging from the column are of greatest concern, because these will provide predictions that can be compared to appropriate sample suites and serve as tests of the significance of reactive melt transport in their petrogenesis.

Important parameters that control geochemical changes of the melt phase in these simulations are: 1) the initial melt composition, 2) the initial mantle matrix composition, 3) the initial matrix mineralogy (which determines D), 4) the initial matrix porosity ϕ , 5) how D and ϕ of the matrix change during reaction (the stoichiometry of the mineralogic reaction), and 6) the relative rates of mineralogic reaction and melt advection.

Initial melt and solid compositions and matrix mineralogy

Since the majority of the earth's upper mantle is considered to be "depleted mantle," or mantle that is depleted in incompatible elements relative to a bulk or primitive earth composition, the initial model mantle matrix used here has a typical depleted mantle trace element composition with lherzolitic mineralogy (Table 1). The model melt that migrates through this mantle matrix is a small-degree, nonmodal, 5% batch partial melt of the same model lherzolitic depleted mantle (Table 1).

Mineralogic reaction

Simulations that involve mineralogic reaction in the mantle matrix simultaneous with melt migration employ two different endmember reactions, guided by evidence of reactions from mantle massifs and xenoliths, and thermodynamic simulations using the MELTS thermodynamic software package (Ghiorso & Sack, 1995). All the simulations involve lherzolite as the initial mineralogy of the solid mantle matrix (Table 1), with a

progressive change in modal proportions to one of two end-member product mineral assemblage as melt continues to flow through the matrix.

One of the end-member mineralogic reactions used here is that of melt + lherzolite \rightarrow melt + dunite. Studies of ophiolites clearly indicate that mid-ocean ridge basalts (MORB) are in equilibrium with dunite, not the surrounding residual harzburgite (Kelemen et al., 1995). Several studies have shown that this is because melts under mid-ocean ridges migrate upwards through lherzolite and harzburgite by dissolving pyroxene and crystallizing olivine. This results in formation of porous channels of dunite towards, and through, which subsequent melts migrate (Kelemen et al., 1995; Kelemen & Dick, 1995). Thus, under some conditions, reaction of migrating basaltic melt with a matrix of lherzolite results in a residual matrix that is depleted in pyroxenes and enriched in olivine relative to the initial matrix mode. Thermodynamic studies and evidence from ophiolites suggests that this reaction is often accompanied by an increase in the porosity of the mantle matrix, because more pyroxene is dissolved by the melt than olivine is precipitated (Kelemen et al., 1995). Thus one of the end-member mineralogic reactions used in these models is conversion of lherzolite to dunite, with increasing ϕ (and increasing melt mass).

A second mineralogic reaction used here is that of melt + lherzolite \rightarrow melt + pyroxenite. There are two primary lines of evidence suggesting that under some conditions melt-mantle reaction results in precipitation of a residue with greater modal proportion of pyroxene than the initial mantle matrix. The first comes from mantle massifs and xenoliths. Composite xenoliths, which most commonly contain veins and dikes of pyroxenite enclosed by lherzolite, indicate that as alkalic magmas flow through the mantle they react with surrounding lherzolite and precipitate primarily clinopyroxene +/- garnet or spinel (Sen, 1988; Sen et al., 1993; Sen & Leeman, 1991; Irving, 1980). Mantle massifs also suggest similar relations (Kelemen et al., 1995; Kelemen & Dick, 1995, Bodinier et al., 1990; Pearson et al., 1993). Thermodynamic modeling using MELTS also

shows that because of the increased stability of pyroxenes and decreased stability of olivine at higher mantle pressures, the higher the pressure of melt-mantle reaction, the larger the proportions of pyroxene the residual mantle matrix. Decreasing magma mass, by cooling during this reaction also increases the amount of pyroxene precipitated during reaction with mantle. Thus the second end-member mineralogic reaction used in these models is conversion of lherzolite to pyroxenite, with decreasing ϕ (and decreasing melt mass).

Models that include changes in matrix mode caused by mineralogic reaction use a changing bulk distribution coefficient of the matrix, from that of an initial mineralogic assemblage with D_i , to a final assemblage, with D_r . This modal change in any cell of the column is assumed to be proportional to the total melt flux through that cell; as more melt flows through the matrix, the greater the change in mode in that cell (Fig. 3). For these models, the D of the matrix in each cell is a function of the difference between the D in the same cell in the previous timestep and D_r , and a unitless reaction rate r ($r \ll 1$, typically $r \sim 0.05$), such that:

$$D^j = D^{j-1} + r(D_r - D^{j-1}), \quad (1.4)$$

where D^j and D^{j-1} are the D in the same cell in the current and previous timesteps, respectively.

As melt propagates into a cell for the first time, the melt front encounters solid mantle of the initial composition and mineralogy, so D in the cell of the melt front is always D_i (an alternative procedure could require D in the melt front cell to be one increment of reaction from D_i towards D_r). As the leading melt batch moves on, and more melt begins to flow through this cell and react with the solid mantle matrix in it, the D changes according to the equation above (Fig. 3). Since each cell has experienced varying amounts of melt flux at any time, each cell will have a different D at any time. Since the rate of change of D in each cell is dependent on the difference between the D of that cell

and D_p , the rate of change of D (and thus of mineralogic reaction) varies in each cell, and is a function of integrated melt flux through that cell (D in each cell changes fastest when the initial melt batch reaches that cell, then the rate of change slows as D approaches D_p) (Fig. 3).

A slightly different scenario is used for changes in ϕ (and relative masses of solid and melt) resulting from melt-solid reaction. Porosity can change either as melt crystallizes within the column, or as minerals are dissolved out of the matrix, as a result of reaction. In order to conserve mass within the column, in simulations involving ϕ change, it changes at a uniform rate in all cells of the column (Fig. 3).

Reaction/advection rates

Particularly important in the geochemical consequences of these simulations are the relative rates of mineralogic reaction, and advection of melt within the column at any time. Large reaction rate, relative to advection rate, indicates a strong reactive exchange influence on the melt composition, whereas large advection rate, relative to reaction rate, indicates a larger relative influence from diffusive exchange and advection of melt. The relative magnitudes of reaction and advection are signified by the Damkohler number, which is a dimensionless ratio of the characteristic time of reaction to the characteristic time of advection. These characteristic times t_{rxn} and t_{adv} , can be expressed as:

$$t_{rxn} = \frac{1}{R}, \text{ and } t_{adv} = \frac{L}{v_f}, \quad (1.5)$$

where R is the reaction rate (s^{-1}), L is a characteristic length scale (m), and v_f is the velocity of the melt (m/s). For any cell within the column at any time j , and for any modal reaction from D_i to D_p , the reaction rate, can be expressed as

$$R = \frac{\left(\frac{D^j - D^{j-1}}{D_f - D_i} \right)}{\Delta t}, \quad (1.6)$$

where Δt is the time elapsed between the change of D in the cell from D^{j-1} to D^j . Simultaneously, the melt is moving through each cell (with a length Δx), at a velocity v_f . So the ratio of characteristic times of reaction and advection in any cell at time j is:

$$\frac{t_{rxn}}{t_{adv}} = \frac{\Delta t v_f}{\left(\frac{D^j - D^{j-1}}{D_f - D_i} \right) \Delta x} = N_D^D, \quad (1.7)$$

where N_D^D is the Damkohler number with respect to modal changes (changes in D). A similar Damkohler number N_D^ϕ , can be written for changes in ϕ . Larger N_D signify a slow reaction rate relative to advection (thus a small reactive exchange influence relative to diffusive exchange) and smaller N_D signify a fast reaction rate relative to advection (thus a large exchange influence relative to diffusive exchange). Figure 3 shows N_D in each cell for varying r in equation 1.4.

RESULTS: EXAMPLES OF REACTIVE MELT TRANSPORT EFFECTS ON MELT COMPOSITIONS

The following examples illustrate some of the important features of the trace element evolution of melt migrating through a reactive mantle column. La, Zr, and all of the rare-earth elements (REE) are used as examples in the first model (purely diffusive exchange, no mineralogic reaction) to demonstrate the effects of purely diffusive exchange on elements with a range of bulk solid-melt distribution coefficients (bulk D 's from 0.003-0.3 in lherzolite). Zr and all the REE are shown for the other models, showing the effects of combined diffusive and reactive exchange involving mineralogic reaction and

changing porosity during reactive melt transport. The initial input melt used in these models is a 5% non-modal batch melt of garnet lherzolite with typical depleted mantle trace element abundances (Table 1). The melt flows through and reacts with a matrix of the same mineralogy and trace element composition as the melt source, with an initial ϕ of 0.05. These models employ a combination of the incremental mass-balance and continuum techniques outlined above, using a column divided up into 30 cells. The incremental model is used to simulate infiltration the initial melt into the column and the first stages of reaction between the melt and matrix. Once the melt has infiltrated the length of the column, the compositions in each of the cells are then used as the initial condition for continued melt flow and reaction using the continuum model outlined above. Solid-melt distribution coefficients for trace elements are shown in Table 1. Further details are provided in each example.

PURE DIFFUSIVE EXCHANGE, NO MINERALOGIC REACTION

Figure 4 shows the evolution of La, Zr, Ni, and rare earth element (REE) concentrations in melt migrating through a reactive column under conditions of purely diffusive exchange (no change in mode or porosity). D for all cells and all time steps is that of garnet lherzolite, and ϕ of the column remains constant at 0.05.

Figure 4a shows La ($D = 0.00316$) concentrations in the leading batch of melt and throughout the column melt every five timesteps. Several important features characterize the behavior of La in the melt. First, as the melt front infiltrates the column and this leading batch of melt reacts with progressively more mantle, La concentrations in the melt front increase by more than a factor of ten. The melt/mantle volume ratio for this leading batch of melt at any stage is $[n(1-\phi)]/\phi$, where n is the number of cells through which the melt front has propagated. In this case, the melt emerges from this column after reaction with 30 cells, and has reacted with a volume of mantle 570 its own volume, or, in this case of an initial 5% batch melt, 28.5 times the volume of its source region.

This increase in La concentration in the melt front slows as the melt reacts with progressively more mantle. If this melt front were to react with an infinite volume of mantle of the composition used here, La concentration in the melt would reach a limiting value, defined by C_i^0/D , where C_i^0 and D are the original La concentration and bulk D of the matrix, respectively. With respect to this leading batch of melt only, this process of reaction with progressively more mantle (without change in ϕ or D) is zone-refining (Pfann, 1952; Harris, 1957), and this steady state value of C_i^0/D is equivalent to the La concentration in an incipient partial melt of the matrix. The volume of mantle required to reach this steady state concentration varies for each element; incompatible elements require reaction with larger volumes of mantle than compatible elements. Because La is highly incompatible, its concentration approaches, but does not reach, this steady state value ($C_i^0/D = 65$ ppm) before this melt front emerges from the column (with a concentration of 57 ppm).

A second important feature of Fig. 4a is that La concentrations are high near the melt front, but low and essentially equal to the initial input concentration of the original source melt just behind this leading batch of melt. A steep La concentration gradient forms in the column, ahead of which melt is in equilibrium with the initial solid matrix (La concentration = C_i^0/D), and behind which melt has the original input concentration. This concentration gradient, or concentration front, propagates through the column at a rate that is less than the velocity of the melt. This is the chromatographic effect (Hofmann, 1972; McKenzie, 1984; Navon & Stolper, 1987, others), by which trace elements move through a reactive column more slowly than the melt. Following the notation of Navon & Stolper (1987), in the case of constant ϕ and D , the velocity of this concentration front (or any point of constant concentration in the column) is given by:

$$\left(\frac{\partial z}{\partial t}\right)_{C_i} = \frac{\phi \rho_f V_f}{\phi \rho_f + (1 - \phi) \rho_s D} \quad (1.8)$$

Thus the velocity of a trace element concentration front, and in fact, the average velocity of the trace element, is inversely proportional to its bulk distribution coefficient. Incompatible elements move through the reactive column faster than compatible elements. The velocity of the La (bulk $D = 0.00316$) concentration front in this example is 0.93 times the melt velocity. The original input concentrations of La behind the concentration fronts in Fig. 4a also reflect the fact that the reactive capacity of the solid matrix is exhausted in those regions, and melt migrates through those regions unchanged (with respect to La concentrations). Thus the reactive capacity of solid matrix in the column is exhausted faster for more incompatible elements than for compatible elements.

Fig. 4b shows that only the first several melt batches to emerge from the column have high La concentrations. Between timesteps 30 and 35, the steep La-concentration front emerges from the column, and La in melt emerging from the column decreases from 57 ppm to 5 ppm. La concentrations in all successive melt batches are essentially at the concentration of the original source melt (4 ppm). Thus the capacity of the mantle matrix to exchange La with the melt is quickly exhausted, the mantle comes into equilibrium with the melt quickly, and no further reaction occurs (with respect to La). The trend of La concentrations in melt batches emerging from the column is a rapid decrease from near the C_i^0/D concentration in the melt front, to that of the input melt for all succeeding melt batches.

Fig. 4c shows the evolution of Zr ($D = 0.03005$) concentration in melt migrating through the column, again with no change in ϕ or D . As in the La case, two important features are worth noting. First, as the melt front reacts with progressively more mantle, the Zr concentration in the melt front increases and approaches the steady state value (C_i^0/D). But relative to the La case, the Zr concentration in the melt front approaches this steady state value quite rapidly and has essentially reached this concentration by the time it has reached only the 10th cell in the column, or reacted with only 190% of its volume in solid

mantle. At this point, the Zr concentration in the melt front is 99.7% of the steady state value (at this same point, the La concentration is only 52.6% of its steady state value).

Fig. 4d shows that Zr concentration in melt emerging from the column remains high, at this steady state value, for several timesteps before emerging melt concentrations come back down to those of the input melt. Whereas the La concentration in emerging melts returned to that of the input melt after only about five melt batches emerged from the column, approximately thirty to forty melt batches emerge from the column before Zr returns to its input melt concentration. This reflects the larger D of Zr and the larger integrated melt flux required to exhaust the reactive capacity of the column for Zr.

Fig. 4e shows the evolution of Ni ($D = 6.9$) concentration in melt migrating through the column with no mineralogic reaction. Very little change in Ni concentration is observed anywhere in the column because the melt is so close to equilibrium with the matrix with respect to Ni. A series of Ni concentration fronts do propagate through the column, between a slightly lower concentration in equilibrium with the initial matrix and a higher concentration of the original input melt. But these concentration fronts only propagate less than five cells into the column during the 120 timesteps, owing to the extreme compatibility of Ni in the matrix (using equation 1.8, the concentration front velocity is 0.006 of the melt velocity).

Fig. 4f shows the REE concentrations (normalized to chondrites) of melt batches emerging from the column at various timesteps. The first melt to emerge from the column (the melt front) is strongly enriched in the light rare-earth elements (LREE) and slightly depleted in the heavy rare-earths (HREE), relative to the original input melt. This melt is the closest to the steady state (C_i^0/D) composition of melt that has reacted with a large volume of mantle. Successive batches of melt to emerge from the column have decreasing REE as the reactive capacity of the solid is exhausted and the melt returns to its original input composition. However, it is the most incompatible elements (those with

lowest D — the lightest REE) that return to their concentrations in the original melt first, followed by progressively less incompatible elements (those with progressively higher D — progressively heavier REE) (Navon & Stolper, 1987). This results in the transient LREE-depleted and MREE-enriched patterns of melts that emerge before the melt compositions finally return to the input melt pattern.

DIFFUSIVE-REACTIVE EXCHANGE: LHERZOLITE TO DUNITE AT CONSTANT ϕ

Fig. 5 shows the effects of combined diffusive-reactive exchange, where the reactive exchange is a simple change in the mode of the matrix. In addition to diffusive equilibration between the melt and matrix, the matrix reacts with the melt by changing its mode, from lherzolite to dunite, with no change in porosity or melt mass. This could be considered dissolution of pyroxene and precipitation of olivine at constant porosity (Kelemen et al., 1995a, 1995b). Due to decreasing modal pyroxene and garnet and increasing olivine during reaction, D of incompatible trace elements decrease, while D of several compatible elements (Ni, Co, etc.) increase due to their extreme compatibility in olivine.

In this and all subsequent models involving changing ϕ or D , the reaction rate is specified by setting $r = 0.05$ in equation 1.4. In each cell, following the arrival of, and reaction with, the melt front, D changes according to equation 1.4 during reaction with the next melt batch. As each cell reacts with progressively more melt, the reaction rate in that cell decreases and N_D^D increases, signifying the decreasing influence of reactive exchange. Fig. 5a shows the this temporal variation in N_D^D in each cell. In all subsequent models, ϕ and/or D change at the same rate as in this example.

Lherzolite to dunite reaction changes the D of Zr from 0.03 to 0.001 (Fig. 5b). As in the purely diffusive example, the Zr concentration in leading batch of melt increases rapidly to the steady state concentration C_s^D/D as the melt front infiltrates the matrix. The melt

front always has this Zr concentration because it always encounters fresh, unreacted lherzolite matrix. Behind the melt front however, lherzolite is converted to dunite as more melt flows through each cell, decreasing D and partitioning Zr from the matrix into the melt. Zr increases behind the melt front to a concentration above that of the steady state C_i^0/D concentration, but continued flux of input melt at the column entrance brings the concentration back down in this region. A concentration front still propagates through the column, but instead of a sharp front between two compositions, it has developed into a hump-shaped front with a high just behind the melt front. The velocity of this propagating concentration front also increases because of decreasing D . This hump-shaped propagation front causes Zr concentrations in melts emerging from the column to first increase from the steady state melt-front concentration to even higher concentrations, then decrease as the reactive capacity of the matrix is exhausted (Fig. 5b).

As in the case of purely diffusive exchange, the first melt to emerge from the lherzolite to dunite reaction column is strongly LREE-enriched (Fig. 5c). Successive melt batches have LREE-depleted patterns, similar to the purely diffusive exchange case. But the middle- and heavy-rare earths (MREE & HREE) show a different behavior. These elements are enriched in the melt behind the melt front due to the mineralogic reaction, and, as in the case of Zr, develop hump-shaped concentration fronts that propagate at velocities that are progressively lower from the light-, to middle-, to heavy-REE. These hump-shaped concentration fronts emerge in succession, producing the distinctive MREE-enriched patterns emerging in intermediate timesteps, followed by HREE-enriched patterns. Again, eventually all the REE concentrations return to those of the input melt, once the reactive capacity of the matrix is exhausted.

DIFFUSIVE-REACTIVE EXCHANGE: LHERZOLITE TO PYROXENITE AT CONSTANT Φ

Fig. 6 shows the effects of combined diffusive-reactive exchange, where the reactive exchange is changing matrix mineralogy from lherzolite to pyroxenite, with constant

porosity. In this case, due to increasing modal pyroxene and garnet and decreasing olivine during reaction, D for most incompatible trace elements increase (e.g., D of Zr increases from 0.0301 to 0.1951).

Because the melt front reacts with only fresh, unreacted lherzolite, Zr concentration in the leading melt batch again reaches the steady state C_i^0/D concentration and remains there with further infiltration (Fig. 6a). Behind this melt front however, lherzolite is converted to pyroxenite, increasing D , and partitioning Zr from the melt to the matrix. Because of this, Zr decreases behind the melt front to a concentration below that of the input melt, but continued flux of input melt at the column entrance brings the concentration back up in this region. This produces a propagating trough-shaped concentration front, with a low just behind the melt front. The velocity of this propagating concentration front also decreases as a result of increasing D , so the trough-shaped front moves much more slowly than the hump-shaped front in the above example. The propagation of this trough-shaped front results in a series of emerging melts in which the concentrations rapidly decrease from the steady state melt front concentration to lower concentrations (Fig. 6b). Eventually, Zr concentrations increase again, as the reactive capacity of the matrix is exhausted, but because the Zr D increases by nearly an order or magnitude, Zr concentrations remain low in emerging melts for quite some time (Fig. 6b).

The REE patterns of emerging melts batches in the lherzolite to pyroxenite reaction model are quite different from other models (Fig. 6c). Conversion of lherzolite to pyroxenite increases the modal abundance of pyroxenes and garnet in the column, which removes middle and heavy rare-earths from the melt as it flows through the matrix. This results in LREE-enriched patterns of all emerging melts, and a sequence of parallel REE patterns with decreasing overall abundances.

DIFFUSIVE-REACTIVE EXCHANGE: INCREASING ϕ WITH CONSTANT MATRIX MODE

Fig. 7 shows the effects of combined diffusive-reactive exchange, where the reactive exchange is increasing porosity, with constant matrix mode. As porosity increases, the melt mass also increases and solid mass decreases. This is essentially modal melting of the matrix as the melt flows through it and diffusively equilibrates with it.

As in other models, Zr concentration in the melt front increases as it infiltrates the matrix (Fig. 7a). But because melt fraction is increasing, diluting incompatible element concentrations in the melt, Zr concentrations in the melt front approach, but do not reach, the steady state C_i^*/D concentration. Behind the melt front the increasing melt fraction dilutes Zr concentrations, producing a trough-shaped propagating concentration front with a low just behind the melt front. Thus the effects of this reaction are similar to those of the pyroxenite reaction above. One difference is that because the mode, and therefore D , of the matrix remains constant, the concentration front propagates at a uniform velocity. This allows a comparatively speedy recovery to input melt concentrations in emerging melts behind the concentration front.

Zr concentrations of emerging melts decrease from near the steady state C_i^*/D concentration to below the original input melt concentration, then gradually increase to the original input melt concentration (Fig. 7b).

REE patterns of emerging melts (Fig. 7c) are similar to those of the purely diffusive reaction model, with an initially LREE-enriched melt (at slightly lower overall REE abundances than the purely diffusive model caused by increased melt fraction), followed by successive melt batches with LREE-depleted patterns, followed by a return to the input melt REE pattern.

DIFFUSIVE-REACTIVE EXCHANGE: DECREASING ϕ WITH CONSTANT MATRIX MODE

Fig. 8 shows the effects of combined diffusive-reactive exchange, where the reactive exchange is decreasing porosity, with constant matrix mode. As porosity decreases, the melt mass also decreases and solid mass increases. This is essentially crystallization of the melt (in modal proportions equivalent to the matrix) as it flows through and diffusively equilibrates with the matrix.

As in other models, Zr concentrations in the melt front increase as it infiltrates the matrix (Fig. 8a). Because melt fraction is decreasing and therefore concentrating incompatible elements in the melt, Zr concentrations actually exceed the steady state C_0^*/D concentration in the melt front. Behind the melt front the decreasing melt fraction increases Zr concentrations, producing a hump-shaped propagating concentration front with a peak just behind the melt front. Thus the effects of this reaction are similar to those of the dunite reaction above, except that no change in the velocity of the concentration front occurs because no change in the matrix mode occurs.

Zr concentrations of emerging melt batches begin slightly higher than the steady state C_0^*/D value, then increase dramatically as the propagating hump emerges, before decreasing to the original input melt concentration (Fig. 8b).

REE patterns in emerging melts again show the initial LREE-enrichment, followed by LREE-depletion with successive melt batches (Fig. 8c). All REE increase slightly before decreasing to input melt concentrations, due to the decreasing melt fraction in the column. The increases occur in succession, from LREE to HREE, as the hump-shaped concentration fronts for these elements successively emerge.

DIFFUSIVE-REACTIVE EXCHANGE: LHERZOLITE TO DUNITE WITH INCREASING ϕ

One of the endmember reactive exchange models outlined above is reaction from lherzolite to dunite with increasing porosity due to dissolution of pyroxenes and

precipitation of a smaller mass of olivine. This scenario has been documented in ophiolites and is thought to occur in situations of mantle migration of large-melt-fraction tholeiitic melts in environments such as beneath mid-ocean ridges (Kelemen et al., 1995a,b).

Figure 9 shows that the trace element effects of this model are similar to those of the lherzolite to dunite mineralogic reaction model. One difference however, is the smaller Zr enrichments (from changing mineralogy) behind the melt front, due to dilution of Zr in the melt by increasing melt mass. This is expected, as increasing melt mass and decreasing bulk D (from lherzolite to dunite reaction) have opposite effects on incompatible trace elements in the melt. Emerging melts show the same increase-then-decrease in Zr concentrations as the lherzolite-to-dunite reaction model.

REE patterns of emerging melts (Fig. 9c) show the familiar sequence of an initial LREE-enriched melt batch, followed by LREE-depleted patterns with successive depletions in more compatible REE. Transient MREE and HREE enriched melts are also observed at intermediate timesteps.

Diffusive-reactive exchange: Lherzolite to pyroxenite with decreasing ϕ

Another one of the endmember reactive exchange models outlined above is reaction from lherzolite to pyroxenite with decreasing porosity and melt fraction due to cooling of the magma as it migrates through the column. Such a scenario has been suggested for migration of small-volume alkalic melts at high mantle pressures. Numerous examples of melts reacting with wallrocks and precipitating pyroxenite exist from mantle xenoliths (Irving, 1980; Sen, 1988; Sen et al., 1993; Sen & Leeman, 1991) and massifs (Bodinier et al., 1990; Pearson et al., 1993; Bodinier et al., 1988; Rivalenti et al., 1995).

Figure 10 shows that the trace element effects of this model are similar to those of the lherzolite to pyroxenite reaction model. Two subtle differences however, are the higher

Zr enrichments in the melt front due to decreasing melt fraction, and the strongly decreased velocity of the trough-shaped concentration fronts caused by both increasing D and decreasing ϕ . Emerging melts show the same rapid decrease in Zr concentrations as the lherzolite-to-pyroxenite reaction model (Fig. 10b).

Emerging melts (Fig. 10c) show parallel, LREE-enriched REE patterns with decreasing overall abundances, similar to the lherzolite-to-pyroxenite model without ϕ change. One difference however, is that the melt front has a higher overall abundance of REE than the purely mineralogic reaction model.

DISCUSSION: KEY FEATURES OF REACTIVE MELT TRANSPORT

The models presented here support previous suggestions that reaction of mantle rock with migrating melt has the potential to dramatically modify magma trace element compositions. While these are end-member models that represent the maximum geochemical effects of such processes, they suggest that reactive melt transport is potentially capable of severely scrambling any mantle-source geochemical signature of mantle-derived melts. Even if the effects shown here are end-member consequences, they could illustrate geochemical consequences of melt-mantle reaction that might be observable in nature. Identifying key features or predictions of these models that are potentially observable in real lavas is the first step to constraining the actual significance of these processes in basalt petrogenesis.

With respect to melts emerging from a column of reactive mantle, the examples in this study illustrate three primary, potentially observable, chemical effects of reactive melt transport. These are 1) enrichment of incompatible elements in the melt front as it infiltrates and equilibrates with fresh, unreacted mantle, 2) chromatography, by which concentration fronts of elements in the melt propagate at different velocities causing unusual co-variations of trace element abundances (e.g., strongly LREE-depleted

patterns) and, 3) mineralogic reaction effects, by which changing porosity and mode within the column add or remove elements from the melt.

THE MELT FRONT AND ZONE-REFINING/AFC

Incompatible element enrichment in the leading batch of melt (melt front) is one of the most dramatic and robust effects of reactive melt transport. The greater the volume of mantle equilibrated with the melt front (via a longer column, lower ϕ , or both), the greater the incompatible element enrichment in this first batch of melt to emerge from the column. In the case of constant ϕ , the concentration of a trace element in the melt front approaches a steady state value defined by the concentration of the element in the matrix and the bulk distribution coefficient of the matrix (C_s^0/D). This can be seen from the equation for zone-refining in the case of constant porosity and no residual porosity (Pfann, 1952):

$$C_f = C_f^0 \exp\left(-\frac{\rho_s V_s}{\rho_f V_f} D\right) + \frac{C_s^0}{D} \left[1 - \exp\left(-\frac{\rho_s V_s}{\rho_f V_f} D\right)\right] \quad (1.9),$$

where C_f^0 is the initial concentration in the original melt, V_s and V_f are the volumes of solid and melt, and D is the bulk distribution coefficient of the element. For large ratios of solid to melt (V/V_f), the melt concentration approaches the limit

$$C_f = \frac{C_s^0}{D} \quad (1.10),$$

which is equivalent to an incipient partial melt of the matrix. Thus melt reacting with large volumes of mantle matrix approach the composition of a very small degree partial melt of the matrix, regardless of the original melt (or source) composition. It can also be seen from this equation that elements with larger D approach this limiting concentration faster, for a given V/V_f , than do elements with smaller D . Thus compatible trace elements

reach their steady state (C_0^*/D) concentrations faster than incompatible elements. Figure 11 shows that this process can generate quite large enrichments in highly incompatible elements (e.g., La, Ba), but large volumes of solid are required to reach this steady state value, whereas more compatible elements (e.g., Zr, Sc) reach the steady state value much sooner.

In the case of changing ϕ , trace element effects on the melt front are not equivalent to those of zone-refining, but assimilation-fractional crystallization (e.g., DePaolo, 1981). For incompatible elements, reaction (i.e., assimilation) combined with decreasing porosity (i.e., crystallization) drives concentrations to values higher than the steady state (C_0^*/D) concentrations (Fig. 7). Reaction combined with increasing porosity (i.e., melting) drives concentrations to values lower than the steady state (C_0^*/D) concentrations (Fig. 8). Even in cases of changing ϕ however, reactive melt transport generally results in incompatible element enrichment in the melt front. Only if there is a large increase in melt mass during reactive transport (i.e., if the matrix melts to a larger degree than the original melt source), or if the input melt is derived from very low degrees of melting of a highly-incompatible-element-enriched source, will reactive transport through typical depleted mantle result in a depletion in incompatible elements in the melt front (relative to the input melt).

CHROMATOGRAPHIC EFFECTS

While dramatic in their capacity to enrich the melt front in incompatible elements, the trace element effects of zone-refining or assimilation-fractional crystallization on the melt front do not provide an unambiguous signature of reactive melt transport in magmas. First, incompatible element enrichment in melts is easily attributed to mantle source compositional variation. When observing a single batch of magma or a limited sample suite of such magmas, incompatible-element enrichment could signify either very low degrees of melting of a depleted mantle source, larger degrees of melting of an

incompatible-element enriched source (Frey & Roden, 1987; others), or melt-mantle reaction (Alibert et al., 1983; Sims et al., 1995, others). Second, zone-refining or AFC approaches can only be used to model trace element changes to the melt front, not in the melt batches that follow it, and thus they provide no information on how the compositions of melts emerging from a single reactive column should change with time. One of the main purposes of this study is to predict temporal-compositional variation resulting from reactive melt transport, in hopes that it may provide a critical test for the process. One such effect obviously is a decrease in incompatible element enrichment in successive melt batches (e.g., Figs. 4 and 5), as the matrix reactive capacity decreases. But as can be seen from the unusual REE patterns of some of the model melts (Figs. 4-10), another important effect of reactive melt transport is chromatography, or the decoupling of abundances of trace elements with varying degrees of compatibility in emerging melt batches.

One of the most important, potentially observable, chromatographic effects on melt compositions is the sequence of REE patterns of melt batches emerging from mantle columns undergoing no mineralogic reaction or reaction from lherzolite to dunite (Fig. 4, 5, 7-9). The melt front in these cases is strongly LREE-enriched, but successive melt batches show depletions in progressively heavier REE (Navon & Stolper, 1987), resulting from their increasing compatibility. It is important to note however, that these chromatographic REE patterns are not observed in cases where the matrix reacts from lherzolite to pyroxenite (Figs. 6, 10). If they are not masked by mineralogic reaction effects, as discussed below, chromatographic effects can impart very distinctive trace element patterns to melts emerging from a column of reactive mantle. Because of efficient separation of concentration fronts of elements with even fairly similar D , chromatographic effects may be observable in REE patterns or in decoupled concentration variations for elements that are usually well-correlated. If the mantle matrix has a different isotopic composition than the input melt, there may also be chromatographic effects in the covariation of isotopic compositions (see Appendix A).

The absence of chromatographic trace element and isotopic patterns in many types of lavas has been used to argue against significant melt-mantle reaction by migrating melts (Cohen et al., 1996; Hauri et al., 1996). Mineralogic reaction within the column however, can mask some trace element chromatographic effects.

MINERALOGIC REACTION: CHANGES IN D AND ϕ

Mineralogic reaction within the mantle column has two main effects on trace element concentrations of melts. First, the reactive exchange of elements caused by either changing D or ϕ acts as a source or sink of elements in the melt within the column, and produces the characteristic trough- or hump-shaped propagating concentration fronts of melts within the column (Figs. 5-10). Decreasing ϕ increases concentrations of incompatible elements in the melt (similar to the effects of crystallization), while increasing ϕ decreases incompatible elements (similar to melting). On the other hand changes in ϕ do not significantly affect compatible elements concentrations because diffusive exchange with the matrix, which has relatively high concentrations of compatible elements, buffers their concentrations. Change in mode from lherzolite to dunite increases incompatible element abundances in melt behind the melt front, and decreases compatible element abundances, though not severely because of the buffering effect. Reaction from lherzolite to pyroxenite decreases incompatible element abundances behind the melt front, because nearly all incompatible elements have higher distribution coefficients in pyroxene and garnet than in olivine, and causes modest increases in compatible elements.

In addition to the source or sink effects of reactive exchange, changes in D and ϕ also modify chromatographic effects. Equation 1.8 shows that the rate of propagation of concentration fronts, and also the rate at which a column matrix reactive capacity is exhausted, are functions of D and ϕ . Increasing D or ϕ within the column (lherzolite to pyroxenite reaction or decreasing porosity) during reaction decreases the velocity of

concentration fronts of incompatible elements, while decreasing D or ϕ (lherzolite to dunite reaction or increasing porosity) increases the velocity of concentration fronts of incompatible elements. Mineralogic reactions that increase concentrations of incompatible elements behind the melt front (lherzolite-to-dunite or decreasing ϕ) result in a sequence of emerging melt concentrations that is different from other models. Instead of rapidly decreasing concentrations in emerging melt batches, successive melt batches in these models show an initial concentration increase to greater than the steady state C_i^0/D concentration, before beginning their decrease (Figs. 5, 8).

The most important feature of the models involving mineralogic reaction is the strong correlation of incompatible element concentrations in emerging melt batches in the case of matrix reaction from lherzolite to pyroxenite (Figs. 6, 10). In these cases the chromatographic effect that generates the strongly LREE-depleted and HREE-enriched REE patterns is not observed; all incompatible elements decrease in concentration at roughly the same rate, preserving the LREE-enriched pattern in all melt batches. In this case, the repartitioning of elements in the column behind the melt front, caused by the lherzolite to pyroxenite reaction, masks the chromatographic effects like the strongly LREE-depleted patterns in the other examples. As long as this change in mode occurs at a rate comparable to the rate of melt advection, the resulting REE patterns in emerging melts will be LREE-enriched, parallel, and steadily decreasing in overall REE abundance. This is in contrast to the other models, which predict emerging melts with strongly LREE-depleted and HREE-enriched melts that are unusual in typical magmas.

Mineralogic reaction during reactive melt transport imparts a strong geochemical signature of the product mineral assemblage to emerging melts. Even though there was no pyroxenite in the original mantle source of the melt or the initial matrix through which the melt passed, compositions of the melts emerging from the column show a clear trace elemental signature of equilibration with pyroxenite, and might lead to an interpretation (without the context of reactive melt transport) of a pyroxenitic mantle source. Such an

interpretation would be incorrect--the melt was derived originally from a lherzolitic mantle source and only reaction *en route* to the surface imparted the pyroxenitic trace element signature.

INFERRING MANTLE SOURCE CHARACTERISTICS

Trace element compositions of mantle sources

One of the most dramatic effects of reactive transport is the extreme enrichments in incompatible trace elements in the melt front caused by diffusive equilibration with mantle. Using a typical batch or fractional melting model to infer a mantle source composition from such a melt would obviously lead to an erroneous conclusion. Figure 12 shows REE concentrations of a solid mantle source inferred from the composition of a melt that has reacted with a sufficiently large volume of depleted mantle so that REE concentrations are at steady state (C_i^0/D) concentrations. Any melting model with a volume fraction of melt greater than 0.5% yields a mantle source with a LREE-enriched REE pattern. Because segregation and extraction of melts from extents of melting lower than a few percent have traditionally been considered unlikely, this has led most studies to conclude that the source regions of strongly LREE-enriched magmas are LREE-enriched. Because the isotopic compositions of these melts usually require a long-term depletion in LREE, a recent metasomatic enrichment of LREE prior to melting is also invoked. Only if the extents of melting are extremely small, typically less than 0.2% (Frey & Roden, 1987; Alibert et al., 1983; Sims et al., 1995), can the isotopic and trace element compositions of these magmas be reconciled without invoking recent, pre-melting metasomatic enrichment. Some recent studies have suggested that extraction of such low-degree melts from the mantle may not be unreasonable (McKenzie, 1989; Riley & Kohlstedt, 1991; Jin et al., 1994), and not require such special mantle source histories. But the examples of reactive melt transport shown here, and in other studies (e.g., Navon & Stolper, 1987) illustrate that extensive melt-mantle reaction can also generate strong incompatible element enrichments in relatively large degree melts of typical depleted

mantle, in agreement with isotopic constraints, and without the need for extremely low degrees of melting or recent pre-melting metasomatic enrichment.

Isotopic compositions

Isotopic compositions of primitive, oceanic basalts are typically considered to reflect the isotopic compositions of their mantle sources. If melt migrates through, and reacts with, mantle that has a different isotopic composition, then the composition of the melt will change however, and there will be a correlation between the isotopic and trace element composition of emerging melt batches. The isotopic composition ϵ , of melt migrating through reactive solid can be approximated in the context of the incremental mass-balance method (Appendix A) as:

$$\epsilon_i^j = \frac{\epsilon_{i-1}^{j-1} \rho_f \phi_{i-1}^{j-1} C_{f_{i-1}}^{j-1} + \epsilon_{si}^{j-1} \rho_s (1 - \phi_i^{j-1}) C_{si}^{j-1}}{\rho_f \phi_{i-1}^{j-1} + \rho_s (1 - \phi_i^{j-1}) C_{si}^{j-1}} \quad (1.11)$$

In general, melts that emerge early in the sequence of emerging melt batches will be incompatible-element enriched and will have the isotopic compositions of the mantle matrix. As successive melt batches emerge from the column, incompatible element concentrations will decrease, and isotopic compositions will begin to shift from those of the matrix towards those of the original melt source. This should result in a correlation between incompatible element abundance and isotopic composition. The isotopic composition front of a particular element should propagate through the column at the same velocity as the element's concentration front. Since incompatible elements return to original source melt concentrations faster than compatible elements, in a sequence of melt batches emerging from a reactive column, isotopic compositions of incompatible elements should shift from matrix to source compositions before isotopic compositions of compatible elements. Although some mineralogic reaction (e.g., lherzolite to pyroxenite) may mask chromatographic effects with respect to element concentrations, as in the case of REE patterns (Figs. 6, 10), isotopic compositions should still show a chromatographic

effect, with incompatible element isotope ratios shifting from matrix to source ratios before more compatible element isotope ratios. This could be a useful tool with which to diagnose the effects of reactive transport occurring simultaneously with mineralogic reaction. Some studies have suggested that some isotopic arrays of Hawaiian lavas may be controlled by chromatographic processes (McKenzie & O'Nions, 1991), however other studies indicate that very little or no chromatographic isotopic effects are present in Hawaiian tholeiites (Hauri et al., 1996; Cohen et al., 1996).

Source mineralogy

Changes in matrix mineralogy during reactive melt transport can impart trace element signatures of minerals to the melt that were not present in the melt source, confounding efforts to extract source mineralogy characteristics from mantle-derived basalts. A good example of this is the strong garnet and clinopyroxene trace element signature that is evident from the lherzolite to pyroxenite reaction of the models above. But other types of mineralogic reactions could also be important in terms of interpreting mantle source characteristics. Reaction of small-degree mantle melts with initially lherzolitic mantle matrix may cause precipitation of a phase that was present in neither the melt source or the initial matrix of the reactive column. It is well-known that metasomatic effects on mantle wallrocks, possibly caused by migrating melts, include formation of trace phases uncommon in typical depleted mantle rocks such as amphibole, phlogopite, zircon, apatite, and rutile (Roden & Murthy, 1985; Sen & Dunn, 1994; Bodinier et al., 1990; Menzies et al., 1985). Precipitation of such phases as a result of melt-mantle reaction will have a dramatic effect on the trace element composition of derivative melts. Interpreted in the typical context of single stage melting and instantaneous extraction, the logical, though possibly incorrect, interpretation would be that the original mantle source contained residual amphibole or phlogopite. But the distinction between residual source amphibole and amphibole formed as a result of melt-mantle reaction is quite important. Amphibole, phlogopite, or other trace phases in the mantle source suggests their presence

in a steady state solid mantle assemblage, and a somewhat special history for that mantle region, since they are not particularly common primary mantle minerals in oceanic environments. In contrast, it is quite reasonable to expect that small-degree melts of typical lherzolitic mantle will be somewhat hydrous and could precipitate amphibole as they cool and react with surrounding mantle during migration through the mantle overlying the source region. Simply including this reactive mantle matrix as part of the "source" of this magma, in order to sidestep the issue, is misleading because 1) the reactive mantle matrix may never have contained these phases prior to melt-mantle reaction, 2) melt movement and open-system reaction are integral parts of the geochemical signature, and 3) the extent of trace phase elemental signatures may be associated with other compositional factors, such as isotopic composition, which would also signify the extent of melt-mantle interaction, not isotopic source heterogeneity.

Phases that are commonly invoked as residual mantle source minerals on the basis of magma trace element compositions include amphibole, phlogopite, apatite, ilmenite, zircon, sulfides, and others (Clague & Frey, 1982; Clague & Dalrymple, 1988; Sun & Hanson, 1975; Greenrough, 1988; Halliday et al., 1995). Studies nearly always assume that trace element evidence for residual phases such as these require their presence in the original, pre-melting, solid mantle source. But very little inquiry has been made as to the possibility that these are products of melt-mantle reaction and do not require an unusual mantle source with a special enrichment history. Correlation of the extent of trace element signature of these phases with isotopic composition, or the temporal-compositional variation of these melts would help address this question.

THE PHYSICAL CHARACTERISTICS OF MELT TRANSPORT

It is worth noting again that models of reactive melt transport outlined here are endmember models that make a number of assumptions regarding the characteristics of melt flow and reaction with solid mantle. Most importantly, these models assume that

melt is in local equilibrium with surrounding solid, and is capable of exchanging trace elements via diffusion into and out of solid grains (diffusive exchange) and via solid dissolution and precipitation (reactive exchange). Reactive exchange occurs at a rate that is about four orders of magnitude faster than diffusive exchange; this has several implications. First, if diffusive equilibration is assumed, then potential changes in porosity and matrix mode need to be considered because they occur much faster than diffusive equilibration and they have dramatic effects on melt compositions. Second, if the melt maintains local equilibrium with surrounding solid mantle via diffusive exchange, the melt velocity must be sufficiently slow relative to solid diffusion rates (Navon & Stolper, 1987). Assuming an average grain radius of about 0.25 cm, a solid diffusion rate of about 10^{-10} cm²/s for near-solidus mantle temperatures at about 30–40 kbar (Hart, 1993; Hofmann & Hart, 1978), and an average melt velocity of 1.0 m/yr, a characteristic length-scale of full diffusive equilibration would be about 200 m. Thus a column of reactive mantle must be at least several hundred meters long for significant diffusive exchange to occur, if melt is traveling at this velocity. Increasing melt velocity by an order of magnitude increases the characteristic length scale of equilibration by an order of magnitude. Thus melt flowing faster than 100 m/yr would require a length scale of equilibration of about 20 km, and would not be likely to maintain equilibrium with its surroundings over length-scales appropriate for mantle extraction.

Unfortunately, there are few constraints on melt velocity in the mantle, and what constraints do exist from xenolith and U-disequilibria series studies pertain mostly to regions of melt migration in which the melt has left equilibrium with its surroundings (e.g., Spera, 1984, 1987; McKenzie, 1985; Macdougall, 1995) and is no longer reacting with the mantle to a large extent. Some evidence suggests that melt migration, at least close to the source regions of melts, may be accomplished via pervasive porous percolation over long length scales (Van der Wal & Bodinier, 1996; Kelemen et al., 1992), while other evidence suggests efficient channelization and chemical isolation of migrating melts (Kelemen et al., 1995a; Nielson & Wilshire, 1993, 1996). But this

uncertainty of melt migration mechanisms, and the likelihood that melt migrates via quite different mechanisms in different mantle depths and tectonic environments, provides the impetus for this study. Although melt is definitely out of equilibrium with its surrounding mantle once it leaves its source and therefore must react with it to some extent, the significance of this reaction in modifying magma geochemical signatures is debatable at this time (e.g., Navon et al., 1996; Nielson & Wilshire, 1996). Our best hope may be to compare predictions of these end-member models to real lava compositions in an attempt to ascertain the significance of reactive melt transport in mantle petrogenesis.

GEOCHEMICAL PREDICTIONS AND COMPARISONS TO REAL LAVA SEQUENCES: THE NEED FOR TIME-SERIES OF MONOGENETIC ERUPTIONS

The primary purpose of the endmember modeling in this study is to predict a series of geochemical results that can serve as a test of the significance of reactive melt transport on geochemical signatures of mantle-derived magmas. The next step is then to extract the most important and robust predictions of the models that are manifested in ways that are potentially observable in natural systems and are (ideally) diagnostic and unambiguously the result of, reactive melt transport. These characteristic predictions can then be compared to natural sample suites that have the greatest chance of showing such results if reactive melt transport was indeed operative in their petrogenesis.

One approach to looking for evidence of reactive melt transport in natural sample suites is to examine the solid residue of melting and melt migration such as ophiolites, massifs, and xenoliths (Godard et al., 1995; Kelemen et al., 1995a, Van der Wal & Bodinier, 1996; Irving, 1980; Sen, 1988; Sen et al., 1993; Sen & Leeman, 1991; Hauri & Hart, 1994; Liang & Elthon, 1990; Bodinier et al., 1990). In one respect this approach has been quite successful: most of these studies find abundant evidence that the trace element composition of solid mantle is dramatically affected by migrating melt. Chromatographic concentration fronts have been well-documented in mantle adjacent to dikes (Hauri &

Hart, 1994; Bodinier et al., 1990; Liang & Elthon, 1990) and in some cases, in large-scale regions of pervasive porous percolation (Van der Waal & Bodinier, 1996; Godard et al., 1995). However, demonstrating that solid mantle residue is affected by reactive melt transport does not demonstrate that the complementary melts that have migrated through the mantle have been affected to any significant extent. First, melts are highly enriched in incompatible trace elements relative to solid mantle and thus any small increment of melt-mantle reaction can be greatly modify mantle rocks with respect to incompatible elements, while melt compositions can be little affected. To affect significant incompatible element shifts in melts, large volumes of mantle are required to equilibrate with melt (volumes of mantle on the order of the melt volume). Second, passage of melt through solid mantle may result in a small amount of residual melt left behind in the solid, which can cause significant mantle trace element modification, while the melt that passes through the mantle may be largely unaffected. Examination of residual mantle may document metasomatic affects that are important for solid compositions (and perhaps future melting events), but we seek an answer to the question: Does reactive melt transport through the mantle affect the trace element composition of melts erupted as lavas at the surface, and thus our interpretations of mantle source regions?

The task of examining erupted melts for evidence of reactive melt transport is somewhat more difficult for several reasons. First, variations in trace element concentrations in primitive mantle-derived basalts can usually be interpreted as resulting from variations in the degree of partial melting of a single source, compositional variation between one or more mantle sources, or both. Unfortunately, reactive melt transport can produce trace element variations in magmas that are very similar to varying degrees of melting of a single mantle source. Nonetheless, several fairly unique features of reactive melt transport are distinguishable from these processes. Second, a number of processes besides variations in partial melting and (potentially) reactive melt transport can strongly modify magma trace element signatures; most important of these are probably differentiation via fractional crystallization and contamination via assimilation of country-rocks in shallow-

level magma storage areas; special precautions must be taken in selection of sample suites to reduce potential modification by either fractional crystallization or assimilation.

Probably the two most robust predictions of the geochemical effects of reactive melt transport are: 1) initial melts to emerge from a reactive column are highly enriched in incompatible trace elements relative to the original source melt, and 2) successive melt batches to emerge from a single column of mantle in a single transport event show a characteristic trend of decreasing trace element abundances. For some variations of reactive exchange simultaneously with diffusive exchange within the column (specifically decreasing porosity and reaction from lherzolite to dunite), this decrease in incompatibles is preceded by a transient rise. But in any case, some sort of temporal-compositional trend should exist in magma sequences that have emerged from single reactive columns in single transport events. Other important geochemical predictions of these models that could be looked for in natural sample suites are 1) chromatographic effects that produce decoupling between concentration and isotopic compositions of trace elements with varying degrees of compatibility (though mineralogic reaction in some cases may mask the trace element concentration effects of chromatography), and 2) isotopic variation within samples of a cogenetic sample suite that is correlated with incompatible element variation.

All of these potential indicators of reactive melt transport (high incompatibles in first melt to emerge from column, trend to lower incompatibles in successive melt batches, chromatographic trace element patterns, isotopic-trace element covariation) can only be identified in a suite of comagmatic melts for which a time-sequence of eruption is known. Additionally, to restrict potential confusion regarding multiple mantle sources or melting events, the samples should be erupted in the same monogenetic eruption. This limits the field of possible sample suites considerably. Add to this the requirements that melts must be unfractionated (primitive), and have a small likelihood of contamination by assimilation of country-rocks in shallow-level magma chamber, and the list of potential

sample suites is even more restricted. What is needed to test these models is a time-sequence of melt batches, erupted from the same volcanic vent in the same eruption, that are primitive and have not resided in shallow-level magma chambers for long periods of time.

Among the best possible candidates that meet these criteria (although there may be others) are primitive, highly alkalic magmas that erupt from monogenetic vents on ocean-islands. These lavas also commonly contain garnet peridotite xenoliths carried from fairly high pressures (10-25 kbar) (Clague, 1987; Sen, 1987, 1988; Sen et al., 1990; Sen & Leeman, 1993; Sen, 1983), evidence that they have migrated through large regions of mantle and not resided in shallow-level magma chambers for long periods of time. The lavas are characteristically enriched in incompatible elements (Clague, 1987; Clague & Frey, 1982; Clague & Dalrymple, 1988; Maaløe et al., 1992), although little or no data from multiple samples from single eruptions are available (however Maaloe et al. did analyze multiple samples from individual lava flows). An ideal sample suite that could serve as a test of these models would be a time sequence of lavas erupted in a single monogenetic eruption from a post-erosional vent.

Another reason to focus efforts to identify evidence for melt-mantle reaction on primitive alkalic lavas is the characteristic incompatible-element enrichments, and usually depleted-isotopic compositions, of such lavas worldwide. These observations have traditionally forced workers to invoke either an unusual recently metasomatized mantle source (Clague & Frey, 1982), extremely low (<0.2%) degrees of partial melting (Frey & Roden, 1987; Sims et al., 1995), or large extents of melt-mantle reaction (Harris, 1957; Alibert et al., 1983; Green & Ringwood, 1967). In fact, historically the trace element compositions of primitive alkalic magmas have been one of the prime motivations for even considering the effects of melt-mantle reaction. The models in this study support many earlier suggestions that the incompatible element enrichments and depleted isotopic signatures of such lavas may be explained well by reactive melt transport in the mantle.

The useful extension and potential test of this hypothesis that this study provides, however, is that during a single monogenetic eruption of these types of lavas, the earliest melts should have the highest incompatible element enrichments and successive melt batches should have decreasing concentrations of incompatibles. Chromatographic effects in trace element concentrations may or may not be present in these temporal-compositional sequences, depending on the mineralogic reaction in the transport region.

Although most primitive alkalic lavas all have strongly LREE-enriched REE patterns, some data from post-erosional basalts of Ni'ihau in Hawai'i do show clear LREE-depletions (and other highly-incompatible-element-depletions) similar to the chromatographic REE patterns in some of these models (Clague, unpublished data). If stratigraphic sequences of post-erosional lavas from individual, monogenetic vents could be obtained, they may allow the crucial comparison of temporal-compositional trends predicted in this study.

CONCLUSIONS

While reaction between mantle rocks and migrating magma has been shown to strongly affect the trace element chemistry of the solid mantle, it is unknown whether such reaction has any significant affect on the compositions of magmas erupted at the surface, and therefore our interpretations of mantle source compositions. End-member models of combined diffusive-reactive exchange between melt and solid mantle demonstrates that, under certain conditions, reactive melt transport may strongly modify melt compositions. Key predictions of the effects of reactive melt transport on migrating melts are enrichment of incompatible elements in the first melt batches to emerge from a reactive mantle column and a subsequent decrease in incompatible elements in successive melt batches to emerge from the column. While diffusive exchange is responsible for the incompatible element enrichments in melt fronts, mineralogic reactions within the melt-solid system that result in changing matrix mode and porosity also strongly affect

compositions of model erupted melts. Chromatographic trace-element concentration fronts migrating through the column can be smoothed or masked by mineralogic reactions. In particular, in contrast to depletion in progressively more compatible elements in emerging melt batches caused by chromatographic effects in a column of static mineralogy, a reaction from lherzolite to pyroxenite within the column results in decreasing concentrations of all incompatible elements simultaneously in emerging melt batches.

Evaluating the significance of reactive melt transport on erupted magmas requires comparison of these endmember model predictions to appropriate samples suites. Ideal suites would provide temporal-compositional trace element variations in a sequence of primitive melts erupted from monogenetic volcanic vents. Post-erosional volcanics on ocean-islands such as Hawai'i may provide excellent suites with which to test these models.

Table 1. Parameters used in reactive transport modeling.

Modal proportions	Melt source				Densities (kg/m ³)				
	Phase	source	melting mode	lherzolite matrix	pyroxenite	dunite	melt	solid	
olivine	0.65	0.10	0.65	0.10	1.00	2800			
orthopyroxene	0.24	0.10	0.24	0.00	0.00	3300			
clinopyroxene	0.06	0.40	0.06	0.75	0.00				
garnet	0.05	0.40	0.05	0.15	0.00				

element	Distribution coefficients ^a										Melt source bulk P
	olivine/liq	cp/liq	gpx/liq	garnet/liq	lherzolite bulk D	pyroxenite bulk D	dunite bulk D	Melt source bulk D	Melt source bulk P		
La	0.00045	0.00125	0.0370	0.0070	0.0032	0.0288	0.0005	0.0032	0.0176	0.0363	
Ce	0.00065	0.00195	0.0690	0.0210	0.0061	0.0550	0.0007	0.0061	0.0363	0.0854	
Nd	0.00115	0.00435	0.1500	0.0670	0.0151	0.1257	0.0012	0.0151	0.0854	0.1676	
Sm	0.00160	0.00640	0.2000	0.2170	0.0254	0.1827	0.0016	0.0254	0.2230	0.3914	
Eu	0.00175	0.00830	0.2350	0.3200	0.0332	0.2244	0.0018	0.0332	0.6889	1.7122	
Tb	0.00170	0.01245	0.2500	0.3200	0.0553	0.2984	0.0017	0.0553	2.3392	6.9000	
Ho	0.00180	0.01745	0.2525	1.4650	0.0938	0.4093	0.0018	0.0938	0.0004	0.0004	
Yb	0.00275	0.03880	0.2400	4.0300	0.2270	0.7848	0.0028	0.2270	0.0003	0.0003	
Lu	0.00315	0.04900	0.2350	5.6000	0.3079	1.0166	0.0032	0.3079	0.0003	0.0003	
Ba	0.00030	0.00015	0.0007	0.0001	0.0003	0.0006	0.0003	0.0003	0.0003	0.0004	
Ni	10.0	1.0	2.0	0.8	6.9000	2.6200	10.0000	6.9000	2.2200	2.2200	
P ₂ O ₅	0.0010	0.0100	0.0200	0.1000	0.0093	0.0301	0.0010	0.0093	0.0491	0.0450	
Sr	0.0015	0.0160	0.1000	0.0980	0.0112	0.0764	0.0015	0.0112	0.0112	0.0112	
Zr	0.0010	0.0100	0.2000	0.3000	0.0301	0.1951	0.0010	0.0301	0.0301	0.2011	
Sc	0.2500	1.1000	3.1000	6.5000	0.9375	3.3250	0.2500	0.9375	0.9375	3.9750	

element	Compositions (ppm, except P ₂ O ₅ , wt.%)									
	chondrites ^b	Melt source ^c	5% source melt	Initial matrix ^d	C ₁ D ₁ lherzolite	C ₁ D ₁ pyroxenite	C ₁ D ₁ dunite			
La	0.370	0.208	3.94	0.208	65.14	7.14	457.78			
Ce	0.930	0.722	13.30	0.722	118.74	13.14	1110.77			
Nd	0.720	0.815	13.50	0.815	53.83	6.49	708.70			
Sm	0.230	0.299	4.46	0.299	11.76	1.64	166.88			
Eu	0.087	0.115	1.60	0.115	3.46	0.51	85.71			
Tb	0.058	0.077	0.90	0.077	1.39	0.26	45.29			
Ho	0.087	0.120	1.10	0.120	1.28	0.29	66.67			
Yb	0.248	0.347	1.81	0.347	1.53	0.44	126.18			
Lu	0.039	0.064	0.22	0.064	0.18	0.05	17.14			
Ba		4.0	79.59	4.0	14386.49	7017.54	13333.33			
Ni		2700	394.79	2700	391.30	1030.53	270.00			
P ₂ O ₅		0.008	0.14	0.008	0.86	0.27	8.00			
Sr		13.0	220.46	13.0	1159.16	170.27	8666.67			
Zr		7.0	100.01	7.0	232.95	35.86	7000.00			
Sc		16.9	21.43	16.9	16.03	5.08	87.60			

^aREE: average of McKenzie & O'Nions (1991) and Frey et al., set 3, (1977); others: Green (1994)

^b McKenzie & O'Nions (1991)

^c "Depleted Earth" of McKenzie & O'Nions (1991)

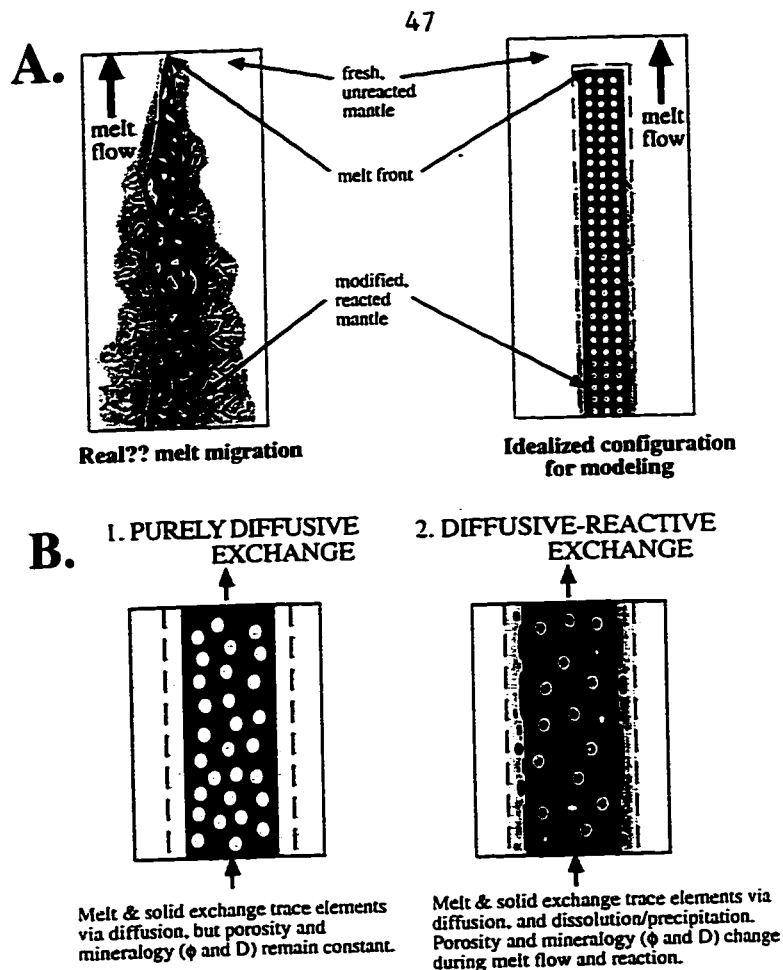


Figure 1. Physical scenario of reactive melt transport for modeling and mechanisms of melt-mantle trace element exchange.

A. Schematic representation of mantle column with reactive solid on sidewalls, in a matrix, or both. As melt flows through the column, solid and melt react by both diffusive exchange (diffusion of elements into and out of solid grains) and reactive exchange (dissolution and precipitation, changing the mineralogy of the solid and/or melt fraction in the column). Regions of the column that have a larger integrated melt flux have reacted to greater extents, so they are closer to trace element equilibrium with the input melt, and, in cases of mineralogic reaction, farther from the initial mode and closer to a final mode.

B. Mechanisms of melt-mantle trace element exchange. 1) Purely diffusive exchange between melt and solid: diffusion of elements into and out of solid grains maintains local melt-solid trace element equilibrium at all points in the column, while mode of solid matrix, porosity, and melt fraction remain constant at all points in the column. 2) Combination of diffusive and reactive exchange: diffusive exchange maintains local equilibrium, but minerals in the matrix are also dissolving and precipitating as a result of reaction. This changes the changes the mode or porosity of the matrix (and therefore melt fraction), or both, as melt flows through the column.

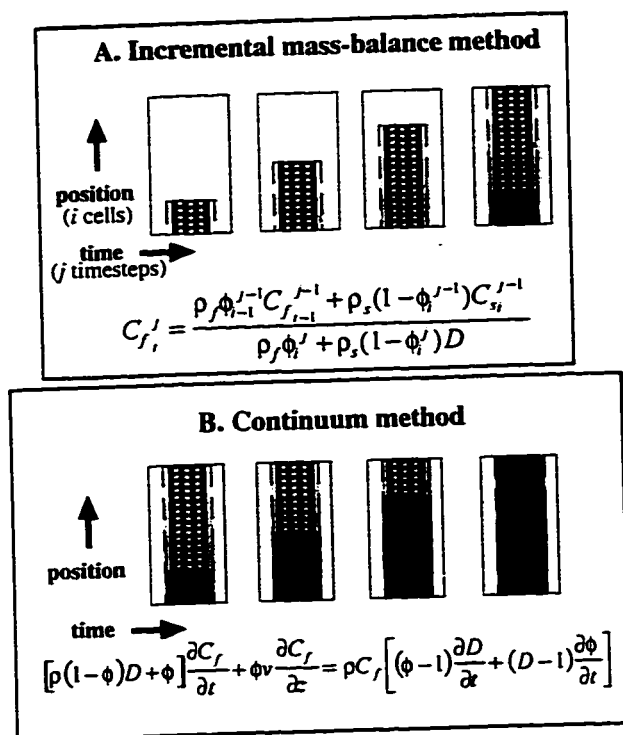


Figure 2. Model scenarios for two different model methods.

A. Incremental mass-balance method: trace element concentration in melt in the i^{th} cell and j^{th} timestep is calculated using equation 2 from the concentrations in the melt in $(i-1)^{\text{th}}$ cell in the $(j-1)^{\text{th}}$ timestep, and the solid in the i^{th} cell in the $(j-1)^{\text{th}}$ timestep (melt advances one cell each timestep, while solid remains stationary). **B. Continuum method:** A finite-difference method is used to solve equation 3 for the trace element concentration in the melt. In both of these methods, bulk distribution coefficient D , and matrix porosity (and melt fraction in each cell) ϕ , can either remain constant, in the case of purely diffusive exchange, or change during melt flow and reaction to simulate mineralogic reaction and combined diffusive-reactive exchange. Models that include modal changes in the matrix assume that D changes from D_i to D_f in each cell using equation 4, and that D begins changing only once the melt front has infiltrated that cell. In order to conserve mass, models that include ϕ (melt fraction) changes assume a similar rate of change as in equation 4, but ϕ changes uniformly in all cells so that a single ϕ characterizes all cells in any given timestep.

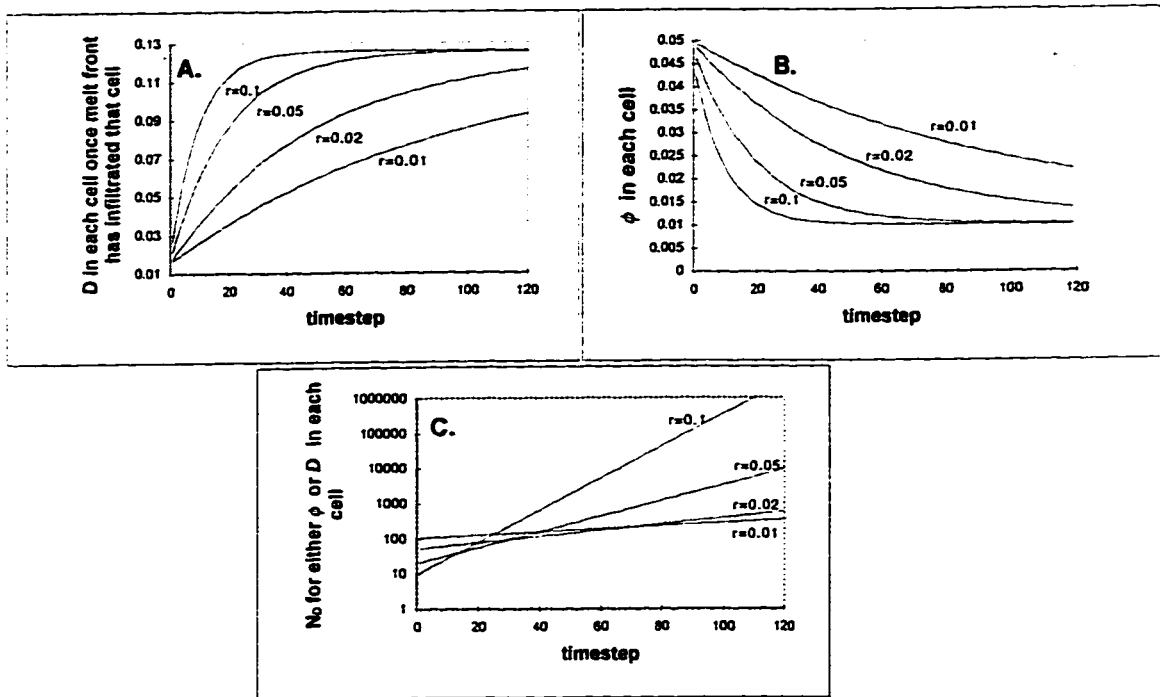


Figure 3. ϕ , D , and N_D in the reactive mantle column, for varying values of r .

A. D for Nd in each cell for reaction from lherzolite ($D = 0.0151$) to pyroxenite ($D = 0.1257$), for varying r . D in each cell only begins changing once melt has infiltrated that cell, thus a similar series of curves defines D for each cell for all timesteps. **B.** ϕ in each cell for decreasing ϕ from 0.05 to 0.01, for varying r . ϕ changes uniformly in every cell of the column throughout all of the timesteps. **C.** N_D for $v_i \Delta t / \Delta x = 1$ (melt advances one cell each timestep) in each cell for varying values of r in equation 4. For higher r values, N_D is low at early timesteps (large influence from reactive exchange relative to advection and diffusive exchange) and decreases dramatically at later timesteps (large influence from advection and diffusive exchange relative to reactive exchange). Thus higher r values mean that the reaction (from D_i to D_f or ϕ_i to ϕ_f) occurs rapidly relative to lower r values.

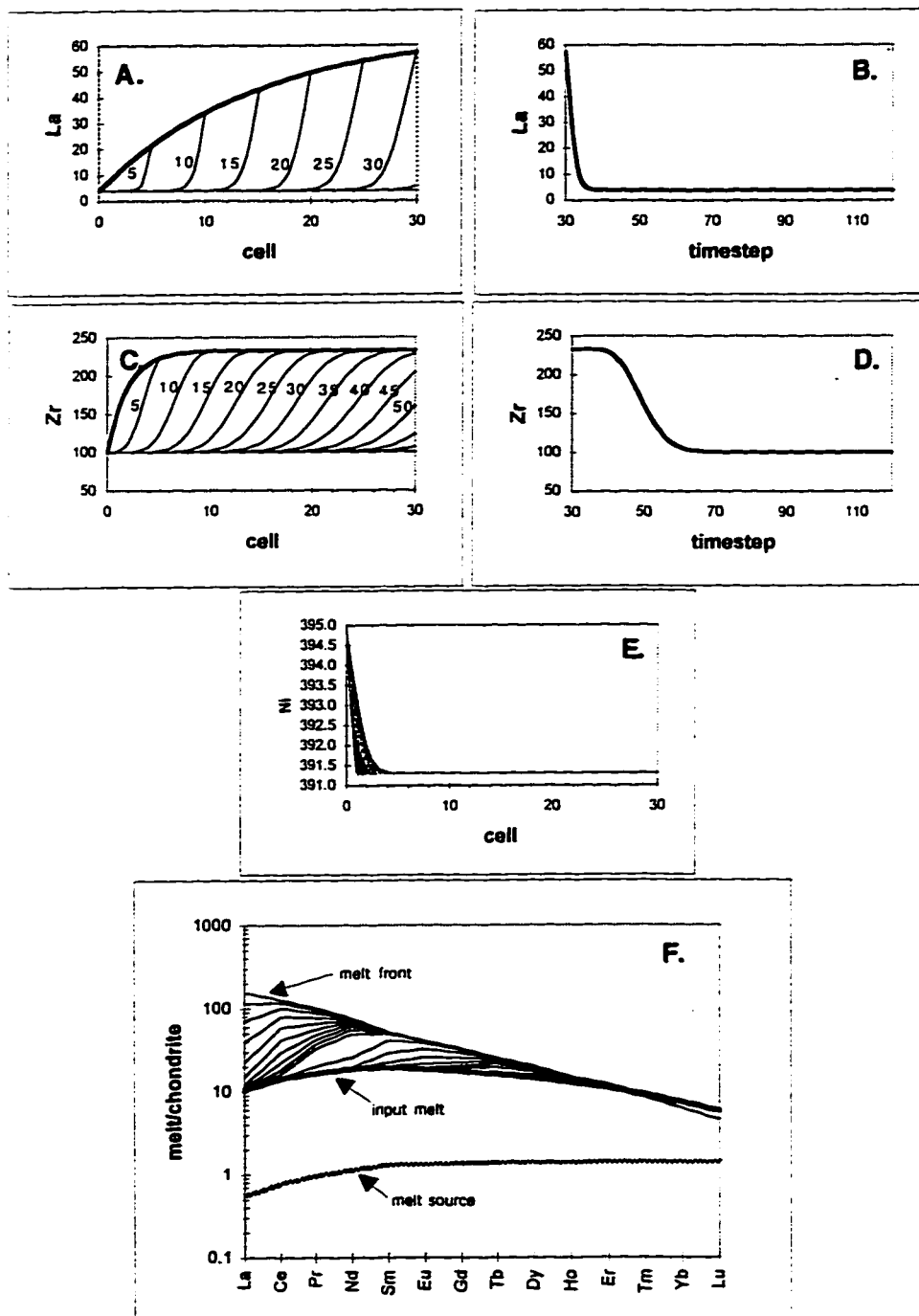


Figure 4. Example, purely diffusive exchange.

Trace element evolution in a 5% depleted mantle melt migrating through, and reacting with, a column of depleted lherzolite with $\phi = 0.05$, under conditions of purely diffusive exchange (no change in D or ϕ). See text and Table 1 for details.

Fig. 4 (continued). **A.** La melt concentrations (ppm) in all cells of the column for different timesteps. Bold curve is concentration in melt front, as it migrates through the column. Other curves are La concentration in the melt every 5 timesteps. La concentrations in the melt front increase as it migrates through the column. At any timestep, a steep concentration front exists, ahead of which La concentrations are large (melt is in equilibrium with the initial matrix composition), and behind which La concentrations are equivalent to that of the input melt. This concentration front propagates through the column and emerges from the column between the 30th and 35th timesteps. **B.** La concentration in melt batches emerging from the column in each of the 120 model timesteps. The first melt to emerge from the column has high La concentrations; successive melt batches show a rapid decrease, followed by steady state concentrations equivalent to that of the input melt. **C.** Zr melt concentrations in the column. Bold curve is concentration in melt front, other curves are Zr concentration in the melt every 5 timesteps. Zr concentrations in the melt front increase and reach a steady state value defined by the matrix mode and initial composition (C_i^0/D). A steep concentration front propagates through the column as in the La example, but this front has a lower velocity than that of La, and takes longer to emerge from the column. **D.** Zr concentration in melt batches emerging from the column. Melt batches emerging from the column in approximately the first 10 timesteps have high Zr concentrations; successive melt batches show a rapid decrease, followed by steady state concentrations equivalent to that of the input melt. **E.** Ni melt concentrations in the column. Ni concentrations are little affected by reaction with the column matrix. A steep concentration front does propagate through the column, but at a much lower velocity than that of either La or Zr, owing to the extreme compatibility of Ni in the matrix ($D = 6.9$). **F.** REE concentrations (normalized to chondrites) in melt batches emerging from the column every 5 timesteps. Also shown by bold lines are the REE concentrations in the input melt and the melt source. The first melt to emerge from the column has high REE concentrations and is strongly LREE-enriched. Successive melt batches have patterns that show decreases in progressively heavier REE (La decreases first, then Ce, etc.). This is a typical chromatographic REE pattern (Navon & Stolper, 1987).

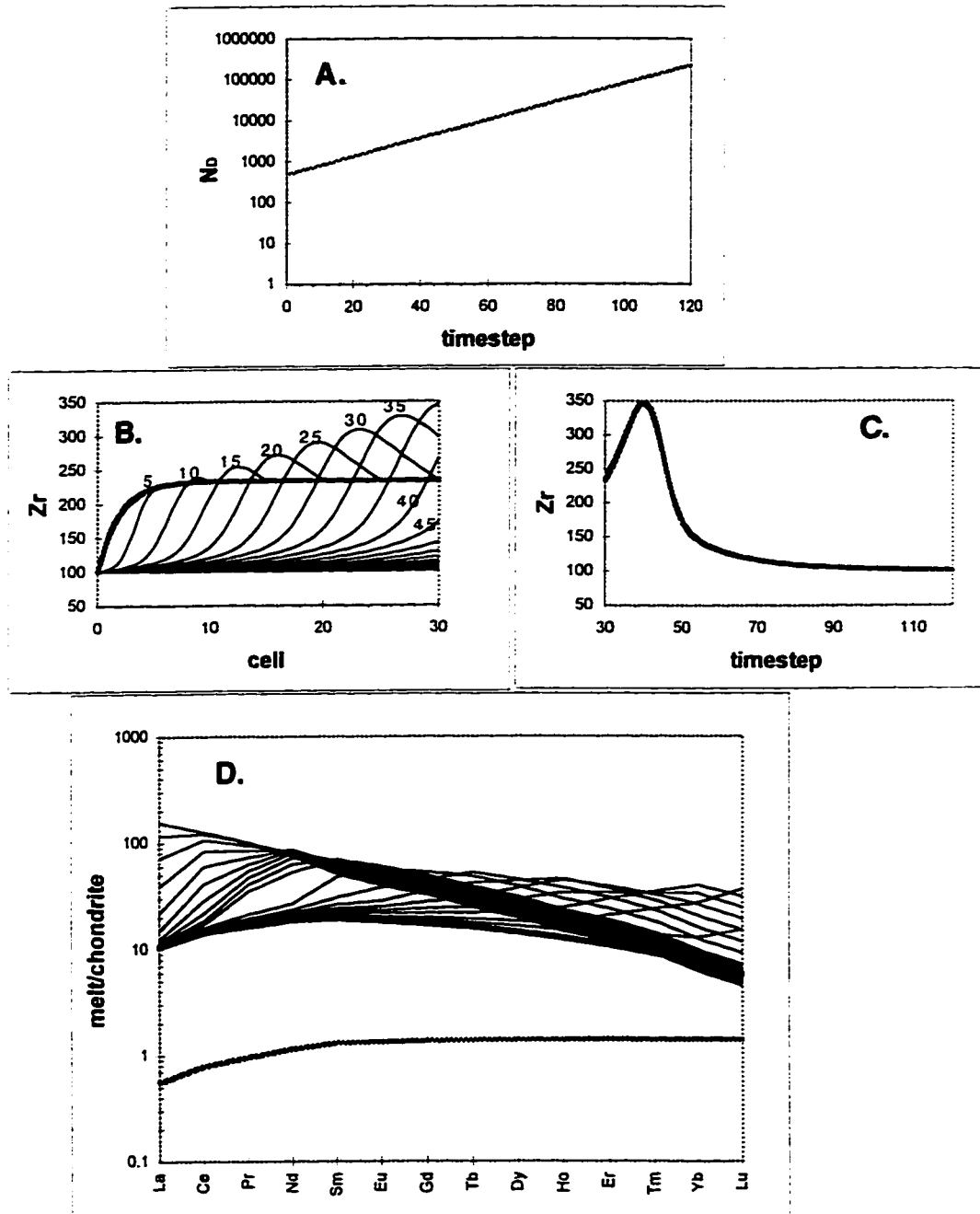


Figure 5. Example, diffusive-reactive exchange: lherzolite to dunite at constant ϕ .

Dahmkohler number and trace element evolution for combined diffusive-reactive exchange, in which the matrix mineralogy changes from lherzolite to dunite as a result of melt-mantle reaction. A. N_D^D in each cell once melt has infiltrated the cell, for $r = 0.05$.

Figure 5. (continued). Early stages of melt-mantle reaction in each cell are characterized by a rapid reaction from lherzolite to dunite, and thus low N_D^D , signifying a large influence from the reactive exchange resulting from the modal change. As the integrated melt flux through each cell increases, the reaction rate slows and N_D^D increases, signifying a decreasing influence of reactive exchange on the melt composition, relative to advection and diffusive exchange. **B.** Zr concentrations in the melt front and in the column each 5 time steps. An increase in Zr concentration behind the melt front is observed, due to decreasing D or Zr resulting from the lherzolite to dunite reaction. This creates a hump-shaped concentration front that propagates through the column with an increasing velocity (equation 8). **C.** Zr concentrations in melt batches emerging from the column. Zr increases from the steady state (C_i^0/D) concentration, to higher concentrations caused by the modal change, then decreases to the input melt concentration with successive melt batches. **D.** REE concentrations in emerging melt batches. The first melt batch to emerge has high REE and a strong LREE-enrichment. Successive melt batches show decreasing abundances, with the chromatographic effect as in the previous example, along with transient increases in the MREE and HREE.

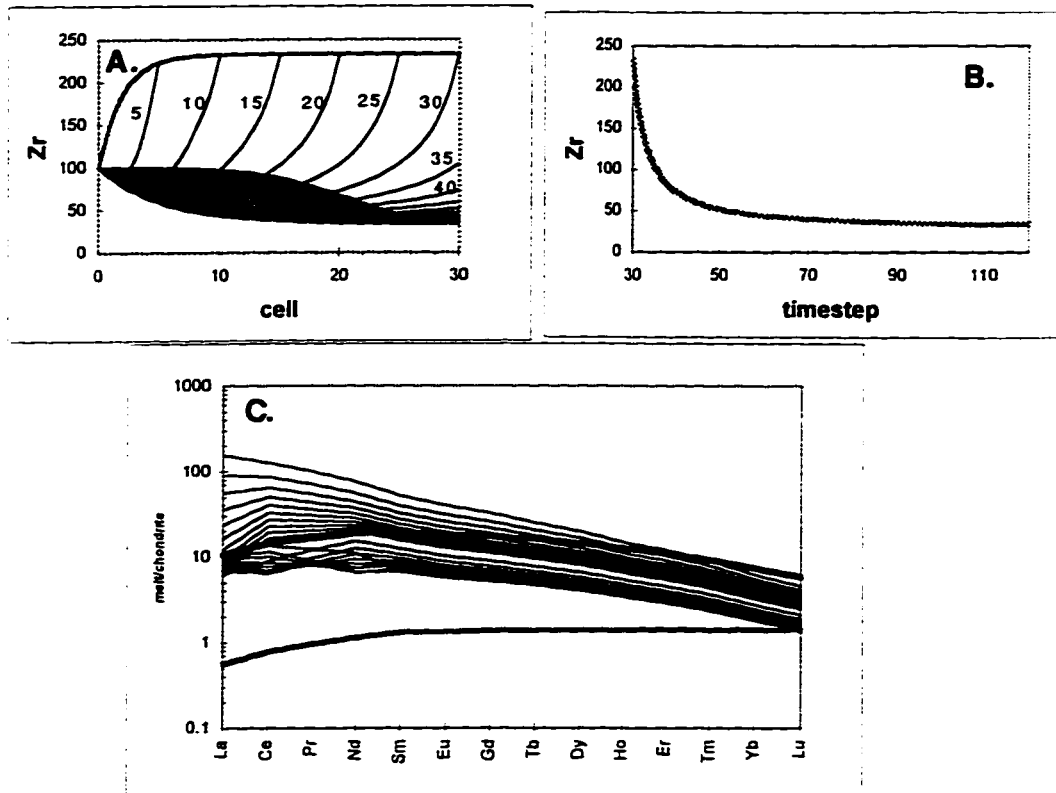


Figure 6. Example, diffusive-reactive exchange: lherzolite to pyroxenite at constant ϕ .

Trace element evolution of melt for combined diffusive-reactive exchange, in which the matrix mineralogy changes from lherzolite to pyroxenite as a result of melt-mantle reaction at the same rate as the previous example. **A.** Zr concentration in the melt front and in melt in each cell each 5 timesteps. Behind the melt front, Zr concentrations decrease as a result of increasing D caused by the lherzolite to pyroxenite reaction. This results in a trough-shaped concentration front that propagates through the column with decreasing velocity (equation 1.8). **B.** Zr concentrations in melt batches emerging from the column. The first melt batch to emerge has the steady state C_i^0/D concentration; successive melt batches show a rapid decrease to concentrations even lower than the input melt concentration because of the mineralogic reaction. Inclusion of more timesteps than are shown here would show the Zr concentrations increasing again to those of the input melt, as the reactive capacity of the column is eventually exhausted. **C.** REE concentrations in emerging melt batches. The first melt to emerge has high REE concentrations, and successive melts show overall decreasing REE abundances. Patterns of nearly all melt batches are LREE-enriched (although some show a depletion in La), and concentrations decrease in parallel REE trends. The chromatographic REE patterns are not observed in this case because they are masked by the effects of the mineralogic reaction, which removes MREE and HREE from the melt to the matrix at approximately the same rate as the LREE-depleted chromatographic signature emerge from the column.

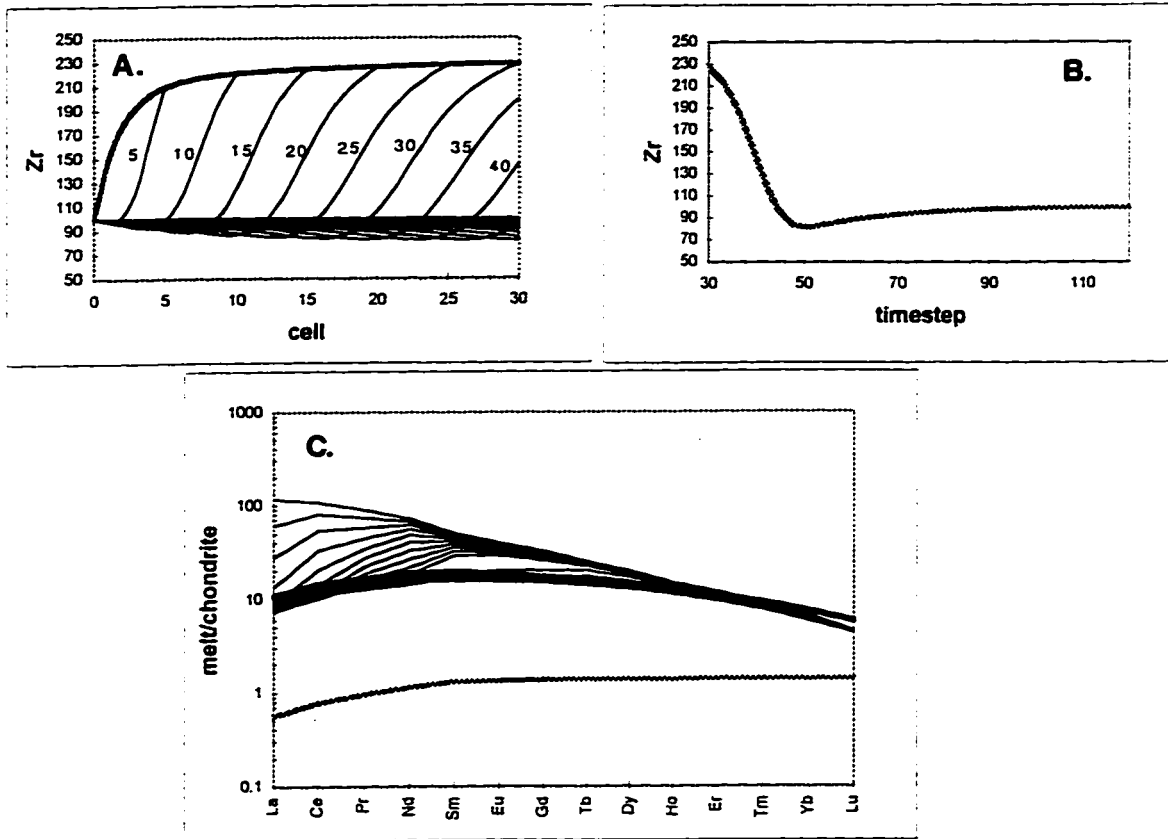


Figure 7. Example, diffusive-reactive exchange: increasing ϕ , constant mode.

Trace element evolution of melt for combined diffusive-reactive exchange, in which the matrix mineralogy remains constant, but ϕ and the melt fraction increase in all cells as a result of melt-mantle reaction at the same rate as the previous example. **A.** Zr concentration in the melt front and in melt in each cell each 5 timesteps. Zr concentrations in the melt front do not quite reach the steady state C_0^0/D concentration due to increasing melt fraction, which dilutes concentrations of incompatible elements like Zr. A trough-shaped concentration front is observed behind the melt front, which propagates through the column at an increasing velocity. **B.** Zr concentrations in emerging melt batches. Zr concentrations show a decrease, followed by a small increase, in emerging melt batches due to the changing melt fraction. **C.** REE concentrations in emerging melt batches. REE show dominantly chromatographic patterns, similar to the purely diffusive exchange model, although concentrations decrease to values lower than those of the input melt before increasing again as the reactive capacity of the matrix is exhausted.

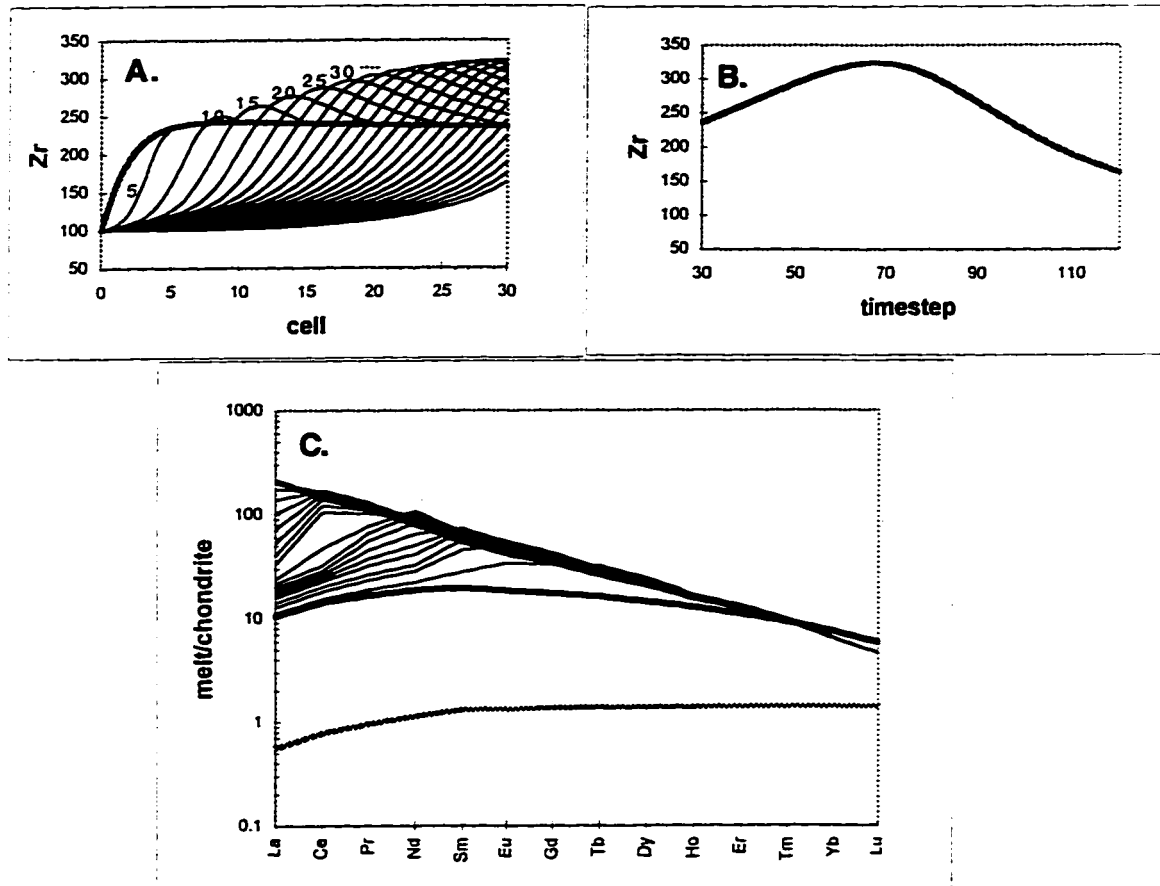


Figure 8. Example, diffusive-reactive exchange: decreasing ϕ , constant mode.

Trace element evolution of melt for combined diffusive-reactive exchange, in which the matrix mineralogy remains constant, but ϕ and the melt fraction decrease in all cells as a result of melt-mantle reaction at the same rate as the previous example. **A.** Zr concentration in the melt front and in melt in each cell each 5 timesteps. Zr concentrations in the melt front slightly exceed the steady state C_0^0/D concentration due to decreasing melt fraction, which concentrates incompatible elements like Zr in the melt. A hump-shaped concentration front is observed behind the melt front, which propagates through the column at a decreasing velocity. **B.** Zr concentrations in emerging melt batches. Zr concentrations show an increase, followed by a decrease to the input melt concentrations, in emerging melt batches due to the changing melt fraction. **C.** REE concentrations in emerging melt batches. REE show dominantly chromatographic patterns, similar to the purely diffusive exchange model, although concentrations increase to values higher than those of the input melt before decreasing again as the reactive capacity of the matrix is exhausted.

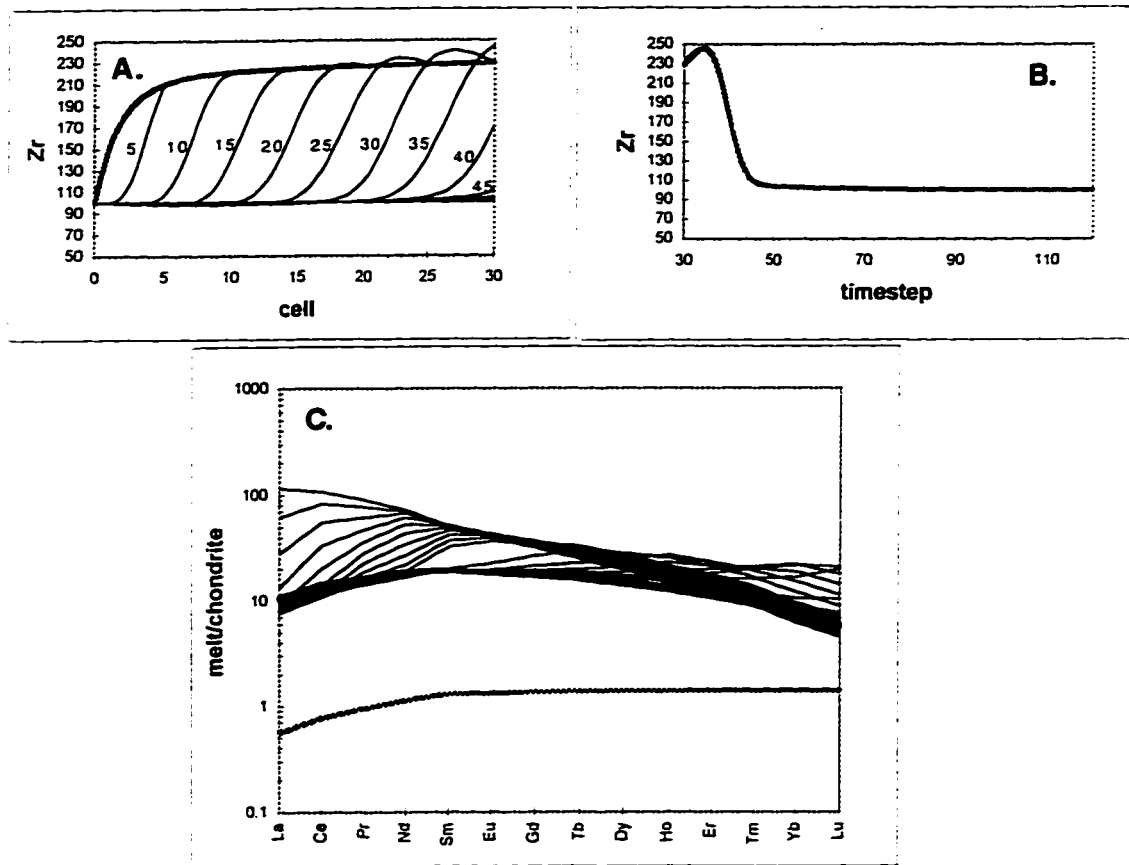


Figure 9. Example, diffusive-reactive exchange: lherzolite to dunite, increasing ϕ .

Trace element evolution of melt for combined diffusive-reactive exchange, in which the matrix mineralogy changes from lherzolite to dunite and ϕ (the melt fraction) increase in all cells as a result of melt-mantle reaction at the same rate as the previous example. See text for discussion.

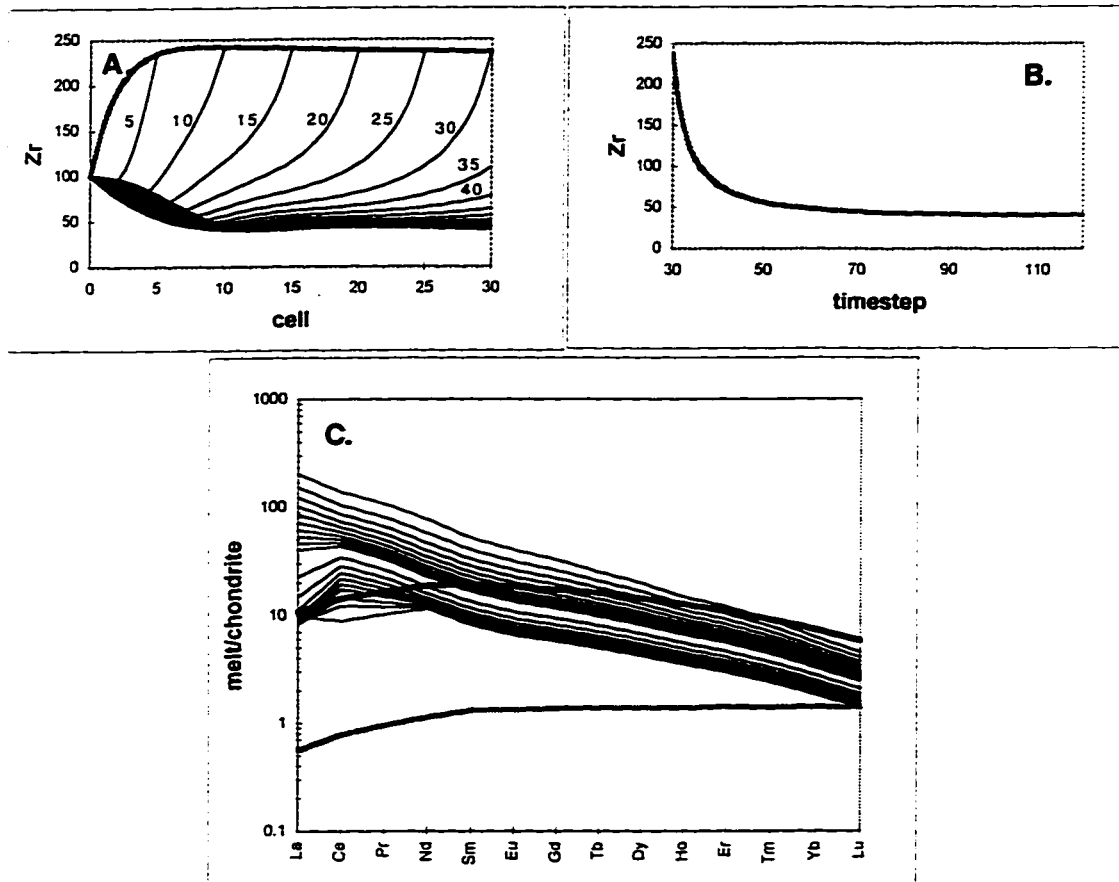


Figure 10. Example, diffusive-reactive exchange: lherzolite to pyroxenite, decreasing ϕ .

Trace element evolution of melt for combined diffusive-reactive exchange, in which the matrix mineralogy changes from lherzolite to pyroxenite and ϕ (the melt fraction) decrease in all cells as a result of melt-mantle reaction at the same rate as the previous example. Note the strikingly parallel patterns and LREE-depletions in the REE concentrations of emerging melts. See text for discussion.

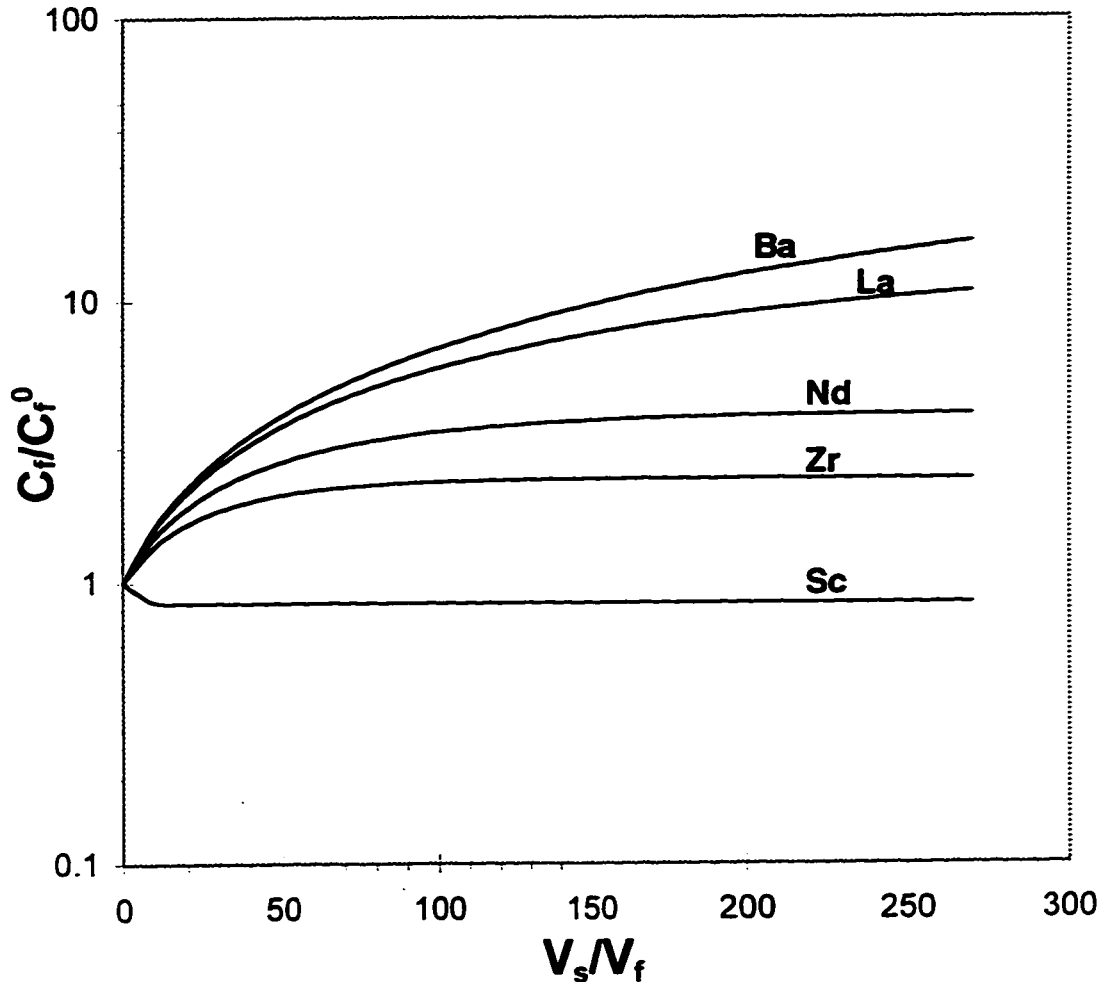


Figure 11. Zone-refining.

Evolution of several trace elements with differing D (Ba = 0.0003, La = 0.0032, Nd = 0.0151, Zr = 0.0301, Sc = 0.9375) in a single melt batch zone-refining through depleted garnet lherzolite mantle. In cases of purely diffusive exchange (no change in mode or porosity), the melt front in these models is zone-refining through the column matrix. Thus the composition of the first melt batch to emerge from the column can be calculated from zone-refining equations. The concentration of each element, normalized to its concentration in the original melt (C_i/C_i^0), is plotted against the total volume of zone-refined mantle, normalized to the volume of the melt (V_s/V_f). Solid mantle composition is assumed as 4 ppm Ba, 0.206 ppm La, 0.815 ppm Nd, 7 ppm Zr, and 16.9 ppm Sc. Concentrations of all trace elements approach steady state C_i^0/D concentrations, but the volume of mantle required to reach this concentration is inversely proportional to the D for each element. Highly incompatible elements also achieve much larger enrichments, relative to the original melt, than less incompatible elements.

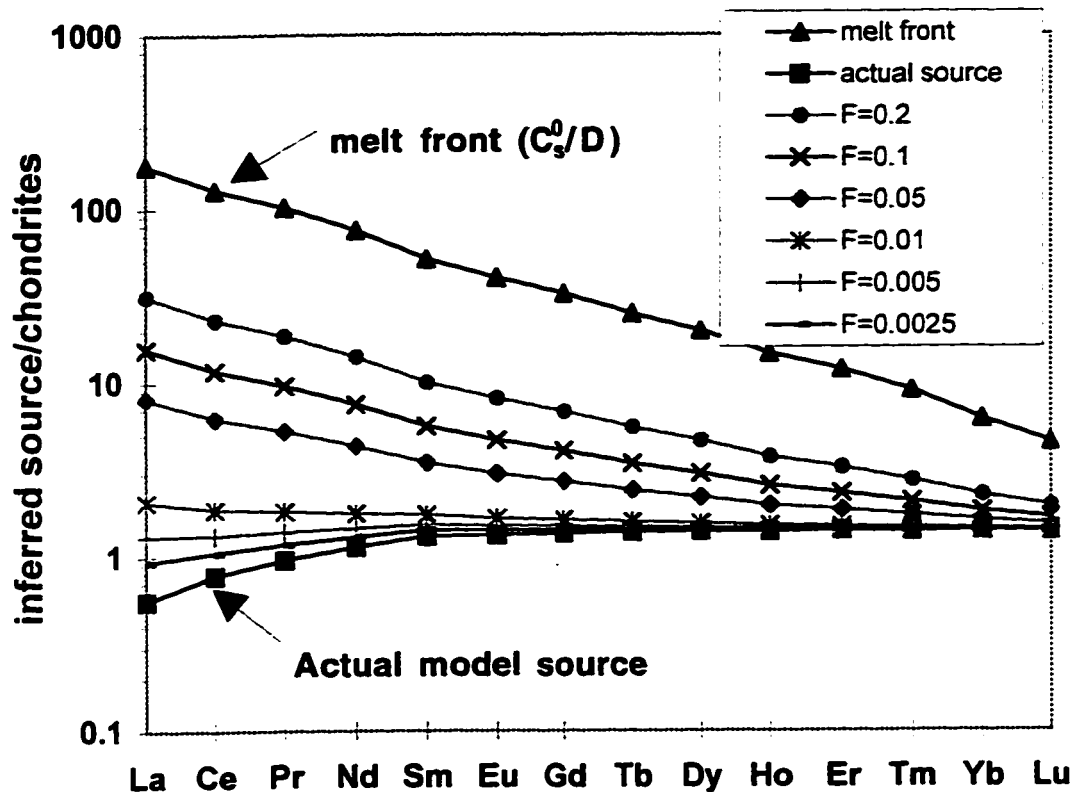


Figure 12. Inferred REE concentrations of mantle source of melt that has reacted with a large volume of mantle.

Inferred REE concentrations of a mantle source of melt that has reacted with a sufficient volume of mantle so as to achieve steady state C_s^0/D concentrations for all the REE. The inferred melting is assumed to be modal batch melting, with total extents of melting F , shown in the legend ($F = 0.2, 0.1, 0.05, 0.01, 0.005, 0.0025$). Because the C_s^0/D concentrations are those of incipient partial melting of the model source, any inferred finite extent of melting overestimates the REE abundance and LREE-enrichment in the source. Only for $F < 0.01$ is the inferred source LREE-depleted. Because typical primitive alkalic basalts are LREE-enriched but have isotopic compositions indicating a long-term LREE-depletion, they must be the products of: 1) melting of a recently LREE-metasomatized mantle source, 2) extremely low degrees of melting (typically $< 0.2\%$) of a LREE-depleted source, or 3) large amounts of melt-mantle reaction.

CHAPTER 2: MELT MIGRATION, REACTION, AND MIXING IN THE MANTLE: ISOTOPIC AND TRACE ELEMENT CONSTRAINTS FROM STRATIGRAPHIC SEQUENCES OF PRIMITIVE, ALKALIC MAGMAS OF KAUA'I, HAWAII

ABSTRACT OF CHAPTER 2

Primitive, low-silica and high-alkali magmas that erupt late in the evolution of most ocean island volcanoes are highly enriched in incompatible trace elements. In contrast, radiogenic isotope abundances in these magmas demonstrate a time-integrated mantle source history of depletion in incompatible elements. Reconciling these observations has traditionally required either extremely low degrees of partial melting of the mantle (commonly less than 0.2%), invoking an unusual mantle source recently enriched in incompatible elements, or extensive melt-mantle interaction. Analyses of stratigraphic sequences of post-erosional volcanics of Kaua'i, Hawai'i show previously unrecognized temporal variations in isotopic and incompatible element enrichments within monogenetic lava sequences that provide additional stringent requirements on models of post-erosional alkalic magma generation. Strong correlations between concentrations of elements with varying degrees of incompatibility (e.g., REE), as well as between incompatible elements and Sr- and Nd-isotope compositions, indicate little or no chromatographic effects on melt compositions. This precludes significant melt-mantle reaction *via* diffusive equilibration of melt with solid mantle, as well as variations in degree of partial melting of a single homogeneous mantle source, whether enriched or depleted in incompatible elements. Variable extents of mixing between large-degree and low-degree partial melts (0.1% and 3-10%, or 2% and 15%, depending on source concentrations) derived from distinct mantle sources with slightly different, but depleted, isotopic signatures explain these data quite well. The decreasing incompatible elements in temporal sequences of lavas during monogenetic eruptions, interpreted as decreasing

proportions of the low-degree partial melt, strongly suggest a mechanism of melt-mixing that is associated with melt transport. One possible explanation is that the large-degree melt component extracts low-degree melt from regions adjacent to its mantle source or migration path and the first melt to leave the source or migrate through the mantle extracts the largest proportion of this low-degree melt. This suggests that incompatible element enrichments characteristic of post-erosional magmas are due to mixing with a low-degree partial melt, possibly associated with melt migration.

INTRODUCTION TO CHAPTER 2

Primitive, low-silica, alkali-rich magmas characterize the waning stage of ocean island volcanism, and are commonly active at the margins of oceanic hotspots. Erupted as small-volume flows and tuffs (generally less than 1 km³) from monogenetic vents, the geochemical signatures of these post-erosional or rejuvenated stage volcanics pose an important petrogenetic problem. They are highly enriched in incompatible elements (e.g., light rare earth elements, Th, P₂O₅, etc.), while their isotopic compositions (low ⁸⁷Sr/⁸⁶Sr, high ε_{Ni}) require derivation from a source with long-term depletion in incompatible elements (Clague and Frey, 1982; Roden and Murthy, 1985; Frey and Roden, 1987). Three hypotheses are generally proposed to explain these and related magma types: 1) they are derived from mantle sources recently (less than 100-200 Ma) enriched in incompatible elements and distinct from those of tholeiites (e.g., Clague and Frey, 1982; Roden and Murthy, 1985), 2) they are derived from extremely small degrees of partial melting (typically less than 0.25%) of depleted mantle sources (e.g., Sims et al., 1995; Frey and Roden, 1987), or 3) they have reacted with solid mantle during melt migration and ascent, and their trace element compositions reflect equilibration with large volumes of mantle outside their source regions (Harris, 1957; Green and Ringwood, 1967; Alibert, 1983). Each of these hypotheses has important and very different implications for the processes of melting and melt migration in general, as well as for our ability to

confidently infer compositions of mantle source regions from basaltic magmas. Although these petrogenetic schemes have been discussed for over 30 years (e.g., Green and Ringwood, 1967; Gast, 1968; Kay and Gast, 1973; Sun and Hanson, 1975), available observations do not allow unambiguous rejection of any of the possibilities.

The best-studied post-erosional volcanics are those of the Hawaiian islands (Clague and Frey, 1982; Clague and Dalrymple, 1988; Maaløe et al., 1992). While most studies have characterized the range of chemical and isotopic compositions of post-erosional volcanics by collecting samples from different monogenetic vents, only a few analyses of clearly cogenetic lavas from individual monogenetic centers exist (Maaløe et al., 1992 analyzed multiple samples from individual post-erosional lava flows). In an effort to distinguish among the petrogenetic models for these types of magmas I have completed trace element and isotopic analyses on samples from stratigraphic sequences of lavas from individual monogenetic vents. In each monogenetic eruption sequence, there are systematic trace element and isotopic variations that indicate changing proportions of two endmember mantle sources in erupted melts as the eruption progresses. Each monogenetic eruption shows a trend from early melts dominated by a component with high incompatible element concentrations and relatively enriched isotopic compositions (i.e., high $^{87}\text{Sr}/^{86}\text{Sr}$ and low ϵ_{Nd}), to later melts dominated by a component with lower incompatible element concentrations and relatively depleted isotopic compositions (lower $^{87}\text{Sr}/^{86}\text{Sr}$ and higher ϵ_{Nd}). These temporal variations provide additional stringent requirements on models of post-erosional magmagenesis, and suggest that melting of any single mantle source (enriched or depleted), and reactive melt transport (involving diffusive equilibration of melt with mantle) are not plausible explanations for post-erosional magmatism. These variations do suggest that post-erosional magma trace element and isotopic variations are dominated by a melt-mixing process that is inherent to melt transport from source through the mantle.

REACTIVE MELT TRANSPORT

This study was designed to test one of the possible explanations for the incompatible element enrichments characteristic of post-erosional magmas: reactive melt transport through the mantle. This process, which postulates that migrating mantle melts equilibrate with solid mantle (either by melting and reprecipitation of solid phases or by diffusion of trace elements in and out of solid grains), was first suggested by workers who noted the capacity of melt-mantle reaction to greatly enrich melts in incompatible elements and generate compositions similar to those of primitive alkalic magmas (Harris, 1957; Green and Ringwood, 1967). More recent studies have revisited the question of reactive melt transport, and its potential to generate both incompatible element enrichments and U/Th isotopic disequilibria observed in magmas (Spiegelman and Elliott, 1993; Lundstrom, 1995; Spiegelman, 1996; Kelemen et al., 1997).

Testing the hypothesis that post-erosional trace element and isotopic compositions are affected by reactive transport requires comparison of model predictions with data from appropriate sample suites. A fundamental feature of reactive melt transport through the mantle is that the reactive capacity of mantle matrix (or conduit wallrock) adjacent to migrating melt is diminished as melt flows through and equilibrates with it. While the first melts to pass through the matrix may be strongly modified by reaction, reactive effects on subsequent melts will decrease, and eventually melt will emerge from a reactive column of mantle unchanged, as the matrix achieves equilibrium with the incoming melt (Navon and Stolper, 1987). Thus one of the most important geochemical consequences of reactive melt transport is a temporal change in magma compositions emerging from a reactive column of mantle (Navon and Stolper, 1987; Chapter 1). Therefore, testing the reactive melt transport model requires data on the temporal evolution of magmas erupted from individual, monogenetic vents.

Several robust and specific predictions of melt-mantle reaction models (Fig. 12) may be compared with real lava sequences (Navon and Stolper, 1987; Chapter 1). First, in

general, the earliest melt batches to emerge from a reactive mantle column should be strongly enriched in incompatible elements relative to the original melt, and should have the isotopic composition of the reactive mantle matrix (not that of the original melt source). Second, subsequent melt batches emerging from the column should have decreasing incompatible element concentrations and more source-like isotopic compositions. Third, chromatographic effects should be observed in the emerging melts, in which concentration and isotopic composition variations of different elements are decoupled (Navon and Stolper, 1987; Hauri et al., 1996; Chapter 1). Typical chromatographic effects in melts would include strongly light rare earth (LREE)-depleted rare earth element (REE) patterns and little or no correlation between abundances or isotopic compositions of trace elements with different degrees of compatibility. Mineralogic reaction may mask some chromatographic effects on trace element concentrations (Godard et al., 1995; Chapter 1), but isotopic compositions of different elements should always show some degree of chromatographic decoupling if reactive melt transport was an important petrogenetic process (Hauri et al., 1996).

A number of studies have focused on samples of residual solid mantle (e.g., xenoliths and massifs) to provide constraints on the extents and chemical consequences of reactive melt transport (Hauri and Hart, 1994; Bodinier et al., 1990; Godard et al., 1995; Van der Wal, 1996; Kelemen et al., 1995; Sen, 1988; Sen et al., 1993; Sen and Leeman, 1991). These studies have documented extensive modal and compositional modification of mantle rocks, on varying scales, by migrating melts. But such studies do not necessarily allow inference of compositional changes to the migrating melts themselves, and how these changes may affect our interpretations of mantle source regions that are inferred from erupted magmas. For example, much of the compositional modification of mantle rocks may be caused by residual melts that are isolated from, and left behind by, migrating melts. In addition, a given xenolith reflects the integrated history of melt-mantle reaction. As later melts pass through they eliminate or modify the chemical record left by preceding melt passage, thus making interpretation of how melt compositions change

with time extremely uncertain. It is also possible that the effects of melt-mantle reaction on erupted magmas may not be controlled by diffusive equilibration with solid mantle, as is usually assumed in studies of mantle xenoliths and massifs.

Regardless of the exact nature and mechanism of melt-mantle reaction during melt migration, it is difficult to escape the consequence that it should have a decreasing influence on successive batches of melt through any mantle conduit or matrix. Whether reaction is manifest as diffusive equilibration, mineralogic reaction, volatile transfer, or incipient partial melting, melts migrating through volumes of mantle that have already reacted with similar melt will not experience the extent of chemical modification that preceding melts did. Therefore, temporal chemical variations (reflecting decreasing modification from reaction with mantle) in lavas erupted from monogenetic sequences would be expected if such reaction significantly affected the magma chemistry.

Study of Hawaiian post-erosional lavas is ideal for maximizing the possibility of observing these predicted effects of reactive melt transport because: 1) they are primitive mantle melts, so fractional crystallization has not significantly overprinted mantle chemical signatures, 2) xenoliths and chemical constraints indicate ascent from depths greater than at least 80 km (Sen, 1987; Sen and Jones, 1990), so melt has had the possibility to react with large sections of mantle, 3) post-erosional lavas erupt from monogenetic vents, limiting the range of potential magma source regions and evolutionary differences between lavas of the same eruption, as well as limiting the volume of magma transported and erupted through the system, thus preserving potential early temporal-compositional trends in erupted melts, and 4) the trace element and isotopic compositions of post-erosionals and similar lavas have been used to argue for extensive melt-mantle interaction.

THE KOLOA VOLCANICS

I examined stratigraphic sections of the Koloa volcanics, the post-erosional stage of volcanism on the Hawai'ian island of Kaua'i (Fig. 14) (Clague and Dalrymple, 1988; Maaløe et al., 1992; Feigenson, 1984). The Koloa volcanics erupted from monogenetic vents scattered throughout the central and eastern part of the island from about 3.5 to 0.5 Ma and include vents, flows, and tuffs of alkalic basalt, basanite, nephelinite, and nephelinite melilitite (Clague and Dalrymple, 1988). Samples older than 1.7 Ma are restricted to the central part of the island while those younger than this age are preserved on the eastern side. The Koloa volcanics lie unconformably above tholeiitic flows of the Napali member (and in some places hawaiitic flows Makaweli and Olokele members) of the voluminous Waimea Canyon Basalt, which form the main mass of the island (MacDonald et al., 1960). Locally, Koloa lavas reach great thicknesses: as much as 650 m in the east wall of the Hanalei valley (Clague and Dalrymple, 1988) and, as discovered by samples used in this study recovered from recent drilling, more than 350 m in the Lihue basin of the eastern part of the island.

I sampled a subaerial section 30 m thick from the Lae O Kilauea vent on the northeast side of the island, and a 300 m thick section drilled through the Lihue basin (Fig. 15). The Hanamaulu Town (HTZ) drillhole contains three multi-flow eruption sequences of post-erosional lavas without apparent unconformities: one of alkali basalts (38 m thick), one of basanites (8 m), and one of nephelinites (50 m) (rock nomenclature used here is based on that of Clague and Dalrymple, 1988). Other flows within the drillhole are bounded above and below by alluvium and/or sediments, and therefore provide no information on temporal trends during individual eruptions.

RESULTS

Tables 2 and 3 show major element, trace element, and isotopic compositions of stratigraphic sequences of Koloa volcanics samples from the Lae O Kilauea vent and the

HTZ drillhole in the Lihue basin. The Lae O Kilauea vent is a large post-erosional vent on the northeast side of the island (Fig. 14) that has been eroded into a semi-circular crater. Whole-rock samples were collected from a stratigraphic section approximately 30 m in thickness, consisting of thin lava flows and tuff layers. Samples from Lae O Kilauea consist of a fine-grained matrix with medium-sized (up to 1 cm) phenocrysts of olivine. Rims of some olivine crystals have been altered to iddingsite.

The HTZ drillhole has a total depth of 305 m, and recovered samples of alkali basalt lavas from depths of 268-306 m, interbedded marine muds and gravels and basanite lavas from 177-268 m, nephelinite lavas from 117-166 m, a matrix-supported tholeiitic/hawaiitic breccia from 64-117 m, and interbedded alluvium, soil, and nephelinite lavas from 0-64 m (Fig. 15). Recovered samples from the HTZ drillhole are splits of rock cuttings collected every 1.5 m. Samples chosen for analyses from these splits were hand-picked cuttings averaging 0.5-3 cm in diameter. Little vertical mixing between cuttings was evident from the lithologic homogeneity of the majority of sample splits, including those adjacent to lithologically distinctive layers, such as shell- and coral-rich layers, as well as stratigraphic compositional and isotopic trends that are opposite to the expected effects of vertical mixing. In cases where splits did contain a minority of lithologically distinct fragments, cuttings of the dominant lithology were selected for analysis.

Some of the Koloa samples are somewhat altered, containing a fine-grained greenish material in the matrix, or serpentinized olivine phenocrysts. The weathered character of some of the samples is reflected in relatively high loss-on-ignition (LOI) in analyses, which are typically between 3 - 8 wt.%, reflecting high H₂O in clay, serpentine, or other low-temperature mineral contents in some of the samples (compositions reported here are normalized to a volatile-free basis). Many of the Koloa lavas also have unusually low Na₂O and K₂O, which is probably also a result of low-temperature alteration (alkalis are known to be preferentially mobilized Hawaiian lavas during near-surface weathering

(e.g., Clague & Frey, 1982)). However, only alkalis (and SiO_2 , to some degree) are correlated with LOI in these samples, and other major and trace elements do not appear to be affected by this alteration. Other studies of Koloa lavas (Clague & Frey, 1982) have also included samples with high $\text{H}_2\text{O} + \text{CO}_2$ (up to 11 wt.%), which, with the exception of alkalis, did not have anomalous major- or trace-element compositions. In addition, LOI or petrographic evidence of weathering are not correlated with stratigraphic position or lithology in these samples.

Alkalic basalts in the HTZ drillhole typically contain large olivine phenocrysts and smaller crystals of clinopyroxene, plagioclase, and oxides in a fine-grained matrix; basanites contain crystals of olivine and clinopyroxene in a matrix of plagioclase, occasional nepheline, oxides, and fine-grained material; nephelinites typically contain crystals of clinopyroxene and rare olivine in a matrix of nepheline, clinopyroxene, oxides, and fine-grained material. Subsamples for isotopic analyses were leached in 6.2 N HCl in an ultrasonic bath for 1.5 hours, to remove alteration effects on Sr- and Nd-isotope compositions.

BASIN-WIDE STRATIGRAPHIC-PETROLOGIC RELATIONS

Previous workers have not recognized any spatial or chronological patterns to the various lithologies of the Koloa volcanics (Clague and Dalrymple, 1988) or other Hawaiian post-erosional sequences (Clague and Frey, 1982). Flows in the Lihue basin however, including samples from additional drillholes (Reiners et al., in prep), show a stratigraphic progression, with decreasing age, of increasing concentrations of incompatible elements (Fig. 16), that is accompanied in the HTZ drillhole by changes in lithology from alkalic basalts, to basanites, to nephelinites.

THE PALIKEA BRECCIA MEMBER IN THE LIHUE BASIN

Drillholes in the Lihue basin, including the HTZ, recovered samples from several thick sections of breccia, conglomerate, and marine layers within the Lihue basin. MacDonald et al. (1960) defined any sedimentary layers, most commonly breccia and conglomerate, within or stratigraphically below post-erosional lavas on Kauaï as the Palikea member of Koloa volcanics. The thickest continuous Palikea layer in the Lihue basin is a breccia layer averaging 53 meters in thickness (Fig. 15). This breccia has a matrix of tholeiitic composition and contains clasts of hawaiite and fine- to medium-grained alkali gabbro (Chapter 3). This unit has been found in six different drillholes throughout the southern part of the basin, and correlates in elevation with subaerial exposures of a layer of the Palikea breccia member (MacDonald et al., 1960) throughout the western part of the basin. It also appears to correlate with the type section of the breccia facies of the Palikea member (Fig. 15), which reaches a minimum thickness of 213 m, suggesting a source region in the steep 1500 m cliffs or central massif to the west of the basin. Bulk samples of the breccia have isotopic compositions ranging from $^{87}\text{Sr}/^{86}\text{Sr}$ of 0.7037 - 0.7038 and ϵ_{Nd} of +5.8 - +5.3, similar to isotopic compositions of tholeiites on the east side of the island (Holcomb et al., in press; Chapter 3) and distinct from those on the west side (Feigenson, 1984; Clague and Dalrymple, 1988; Holcomb et al., in press). This basin-wide breccia layer is most-likely a massive debris flow that originated in the steep cliffs and central massif of the island to the west of the basin. The hawaiitic clasts within it suggest that the central massif of the island may contain significantly larger proportions of hawaiite and alkali gabbro than recognized in the field (MacDonald et al., 1960; Clague & Dalrymple, 1988), and suggests that post-shield alkalic volcanics on Kauaï may be more voluminous than previously thought.

TRACE ELEMENT AND ISOTOPIC COMPOSITIONS

All analyzed Koloa flows are primitive (11-14 wt.% MgO, 275-350 ppm Ni) and apparently not significantly affected by fractional crystallization (Tables 2, 3). I observe systematic trends of decreasing incompatible element concentrations in three out of the four multi-flow eruption sequences, and decreasing ratios of highly to moderately incompatible elements in all of the sequences (Fig. 17). These trends cannot be due to fractional crystallization, as compatible major and trace elements such as MgO and Ni are high throughout the sections and do not vary systematically with respect to stratigraphy (Tables 2, 3). The only major element variations that appear stratigraphically systematic to any degree are SiO₂ and Al₂O₃ in the nephelinite flows between 117-166 m. Both roughly increase upsection (in only this eruption sequence) from about 41.5 to 45.0 wt.%, and from about 10.5 to 13 wt.%, respectively.

Nd and Sr isotope compositions of acid-leached samples also show systematic variation with respect to incompatible elements in samples from the stratigraphic sections (Fig. 18). Both within and between multi-flow eruption cycles, ⁸⁷Sr/⁸⁶Sr and ε_{Nd} are well-correlated with incompatible element abundance, and with ratios of highly to moderately incompatible elements such as La/Lu.

REE patterns are typical of other Hawai'ian post-erosional lavas, showing strong LREE-enrichment (Fig. 19). Samples from individual eruption cycles have relatively restricted REE abundances; alkalic basalts have the lowest, and nephelinites the highest abundances. In general, early lavas in individual eruption cycles have relatively high LREE and middle rare-earth element (MREE) concentrations and successive lavas have progressively lower concentrations (Fig. 20).

A particularly noteworthy feature of these and other post-erosional lavas is the high-degree of correlation between elements with varying degrees of incompatibility such as the LREE and MREE. While both La and Nd systematically decrease during individual

eruption cycles, La and Nd abundances are very well correlated both within and between eruption cycles (Fig. 20).

DISCUSSION

The Lae O Kilauea section and the three continuous sequences of alkalic basalts, basanites, and nephelinites in the HTZ drillhole have a number of characteristics that suggest each comprises at least part of an individual monogenetic eruption. These include the lack of interbedded alluvium or sediment between flows, similar petrographic characteristics and chemical and isotopic compositions of samples within each sequence, and systematic chemical-stratigraphic trends within each sequence.

Three primary geochemical observations of these eruption sequences motivate the following discussion. Most notable is the clear temporal-compositional trend within each eruption sequence, from early lavas with high concentrations of incompatible elements and high ratios of highly to moderately incompatible elements, to later lavas with lower concentrations and ratios (Fig. 17). This establishes that melts from individual, monogenetic post-erosional eruptions can have a significant range of trace element compositions. Second, Sr- and Nd-isotope compositions both within and between eruption sequences are correlated with trace element concentrations: lavas with high incompatible element concentrations have relatively high $^{87}\text{Sr}/^{86}\text{Sr}$ and low ϵ_{Nd} and lavas with low incompatible element concentrations have lower $^{87}\text{Sr}/^{86}\text{Sr}$ and higher ϵ_{Nd} (Fig. 18). A similar observation was made from isotope-trace element data of multiple samples from individual post-erosional lava flows (Maaløe et al., 1992). These correlations require a systematic temporal variation in the proportions of at least two distinct mantle sources in these Koloa lavas. A third important constraint is the strong correlation between different REE (and other elements) that is observed in samples from individual eruptions (Figs. 19, 20). Models of post-erosional magmagenesis must simultaneously explain all these features.

Most previous petrogenetic models of post-erosional lavas have reconciled their incompatible element enrichment and depleted isotopic compositions in terms of a special mantle source that was recently enriched in incompatible trace elements prior to melting (Clague and Frey, 1982; Clague and Dalrymple, 1988). Figure 21 shows that melting of a mantle source with typical depleted mantle trace element concentrations could only produce samples with the highest LREE concentrations, and only then with extremely small degrees of partial melting ($< 0.2\%$). Varying degrees of partial melting of this depleted source cannot reproduce the range of REE concentrations observed for these or other Koloa samples (Maaløe et al., 1992; Clague and Dalrymple, 1988; Feigenson, 1984). Partial melting of a mantle source with a LREE-enriched composition can broadly reproduce the range of Koloa lava compositions (Fig. 21), and illustrates the motivation of previous studies to invoke an enriched mantle source to explain post-erosional chemistry. However, isotopic compositions of the samples in this study unambiguously indicate contributions from two distinct mantle sources, and furthermore the relative proportions of each source are a function of a sample's REE composition. Samples with low REE concentrations and low La/Lu have larger proportions of the low $^{87}\text{Sr}/^{86}\text{Sr}$ and high ϵ_{Nd} source, while samples with higher REE and high La/Lu have larger proportions of the high $^{87}\text{Sr}/^{86}\text{Sr}$ and low ϵ_{Nd} source. No single-stage, single-source melting model can be reconciled with these data, whether the source is depleted or enriched in incompatible elements.

Trace element covariations both within and between eruption sequences (e.g., Fig. 21) are broadly consistent with fractionation of an assemblage of clinopyroxene and garnet, only if accompanied by assimilation of solid mantle in order to maintain high concentrations of compatible elements and prevent significant changes in major elements in the melt. However, in order to model trace element *and* isotopic covariations (Fig. 18), assimilation-fractional crystallization (AFC) must involve assimilation of mantle with improbable Sr and Nd concentrations of approximately 900 and 50 ppm, respectively

(essentially the trace element composition of a 0.1% partial melt of typical depleted mantle). In such a case, it is mixing that dominates trace element abundances in the melt, while fractionation has very little effect (melt-mixing models are discussed in detail below). Thus neither crystal fractionation nor assimilation of solid mantle can explain the trace element and isotopic compositions of these eruption sequences.

Two other models may explain these data. The first involves reactive transport of melt (*via* diffusive equilibration and/or mineralogic reaction) through mantle with an isotopic composition different from that of the original melt. This causes incompatible element enrichment in the melt front and decreasing enrichment in successive melt batches, combined with isotopic shifts from matrix to source compositions as melts emerge from the vent (Navon and Stolper, 1987; Chapter 1). The other model calls on mixing of melts from two distinct mantle sources via some mechanism that results in systematically varying proportions of mixing in stratigraphic sequences of the lavas. Either model has far-reaching implications for the origin of post-erosional lavas and primitive alkalic magmas in general, as well as the geochemical consequences of melt transport in the mantle.

REACTIVE MELT TRANSPORT

Systematically decreasing incompatible element concentrations in Koloa eruption sequences are very similar to predictions of reactive melt transport models in which melt from a depleted mantle source migrates through, and diffusively equilibrates with, similar depleted mantle (Figs. 13, 17). However, the models also predict decoupling of elements with even slightly varying degrees of compatibility, such as the LREE from the MREE. In contrast, there are excellent correlations among a wide range of incompatible elements (Figs. 17, 19, 20), indicating a lack of chromatographic effects on melt compositions. If reactive melt transport is the cause of decreasing incompatible elements in eruption sequences, then diffusive exchange of trace elements between melt and mantle must be

accompanied by mineralogic reaction in the matrix, which may partially mask chromatographic effects.

Models indicate that only reaction of the solid matrix from lherzolite to pyroxenite could potentially mask chromatographic effects on REE patterns (Fig. 13). Such mineralogic reaction is capable of generating trends of decreasing REE similar to those observed in the eruption sequences (Fig. 22). Additionally, composite xenoliths and mantle massifs preserve evidence that alkalic melts migrating through lherzolite at high pressures precipitate pyroxenite (Sen and Leeman, 1991; Irving, 1980; Pearson et al., 1993). One significant problem with this scenario however, is that the maximum (i.e., initial) concentrations of incompatible elements in each eruption sequence are different, but are all linearly correlated (Fig. 22). For example, La and Nd concentrations in the nephelinite eruption sequence of the HTZ drillhole decrease from maximum initial concentrations that are much higher than those of the alkalic basalts, but which fall on the same linear trend. If reactive melt transport is the cause of decreasing incompatible elements in eruption sequences, then the maximum incompatible element concentrations of each eruption sequence would be expected to fall on a zone-refining trend (curved, bold line in Fig. 22), which would increase elements of different compatibility at different rates (e.g., La would increase in the melt more slowly than Nd). The excellent La-Nd (and other incompatible element) correlations both within and between eruption sequences are difficult to reconcile with the effects of reactive melt transport involving diffusive equilibration of melt with mantle during melt flow.

Another problem with the reactive transport model is the good correlation between highly incompatible trace elements (and ratios of highly to moderately incompatible elements) and isotopic compositions both within and among eruption sequences. Figure 23 shows predicted variations of P_2O_5 , La/Lu, and Sr- and Nd-isotopic compositions in melts resulting from reactive melt transport with mineralogic reaction from lherzolite to pyroxenite on a melt with $^{87}Sr/^{86}Sr$ of 0.70290 and ϵ_{Nd} of +9.5 and a matrix with $^{87}Sr/^{86}Sr$ of

0.70335 and ϵ_{Nd} of +6.5. Although varying parameters of the model results in a variety of trends that include many of the data, a robust prediction of the reactive transport model is that sequences of melts emerging from a reactive column will show some degree of decoupling between incompatible elements (and ratios of highly to moderately incompatible elements) and isotopic compositions (Fig. 23). The good correlations between incompatible trace elements and isotopic compositions both within and among these eruption sequences are not consistent with the effects of reactive melt transport involving diffusive equilibration between melt and mantle.

MIXING OF MELTS FROM DISTINCT MANTLE SOURCES

An alternative model that could generate melts with decreasing incompatible elements and changing isotopic compositions during eruption sequences is mixing of melts from distinct mantle sources. Figures 17 through 20 illustrate that if the lavas are the result of variable extents of mixing between two endmember melts, one endmember must have relatively high incompatible element concentrations, $^{87}Sr/^{86}Sr > 0.70335$, and $\epsilon_{Nd} < +6.5$ (melt 1), and the other must have relatively low incompatible element concentrations, $^{87}Sr/^{86}Sr < 0.70295$, and $\epsilon_{Nd} > +8.5$ (melt 2).

If the linear array of La-Nd concentrations in Figure 20 is a melt-mixing trend, then the endmember melts 1 and 2 must lie at opposite ends of this array, with melt 1 having greater than about 47 ppm La and 50 ppm Nd, and melt 2 less than about 14 ppm La and 17 ppm Nd. Similarly, Figure 18 shows that in addition to the isotopic constraints above, melt 1 must have P_2O_5 greater than 0.75 wt.% and La/Lu greater than 240, while melt 2 must have P_2O_5 less than 0.22 wt.% and La/Lu less than 75. A variety of initial mantle source concentrations and extents of melting can produce these melts. Two primary melt-mixing models will be considered here. The first involves relatively low-degrees of melting of two typical incompatible element-depleted mantle sources with slightly different isotopic compositions. This model has the advantage of relative elemental

source concentrations that are consistent with relative melt isotopic compositions developed by long-term depletion in incompatible elements. The second model has two stages, requiring relatively large degrees of melting of two mantle sources following recent enrichment in incompatible elements. The trace element concentrations of these sources were created by recent metasomatism of solid primitive (or plume-like) mantle by low-degree melt of typical depleted mantle (e.g., Chen and Frey, 1983, 1985). While more complicated by requiring a relatively recent metasomatic enrichment event, this latter model has the advantage of consistency with a larger-scale petrogenetic model for Hawai'ian magmatism.

Melt-mixing: Depleted mantle sources

A reasonable candidate for melt 1 (Figs. 18, 24) is a very small-degree melt (~0.1%) of lherzolite with typical depleted mantle trace element concentrations and $^{87}\text{Sr}/^{86}\text{Sr}$ of approximately 0.70335 and ϵ_{Nd} of +6.5 (Table 4). Reasonable choices for melt 2 (Fig. 24) are relatively large degree melts (>2% for pyroxenite, >10% for lherzolite) of either incompatible-element-depleted lherzolite with the same composition as the melt 1 source, or pyroxenite with a trace element composition typical of Hawai'ian pyroxenite xenoliths (Frey, 1980) and $^{87}\text{Sr}/^{86}\text{Sr}$ of 0.70295 and ϵ_{Nd} of +9.5 (Table 4). The slope of the strongly linear La-Nd correlation both within and among eruption sequences in Figure 24 suggests if the melt 2 (high-degree melt) source was lherzolite, then the degree of partial melting of this source was no smaller than about 10%. If, however, the source of the high-degree melt 2 was pyroxenite, then mixing with a range of degrees of partial melting greater than about 2% would satisfy the slope of the La-Nd correlation.

The strongest evidence for melt-mixing and best constraint on melt fractions and proportions of each melt component in Koloa magmas, is the isotopic-trace element correlation both within and between eruption cycles. Figure 25 shows the results of mixing between low-degree (0.1%) and high-degree (2-15%) melts derived from LREE-depleted sources. Assuming a depleted lherzolite mineralogy and typical depleted mantle

trace element concentrations for each melt source (Table 4) reproduces the data fairly well for a range of melting extents of the high-degree melt (Fig. 25). Assuming that the source of the high-degree melt is pyroxenite with trace element concentrations typical of Hawai'ian pyroxenite xenoliths (Table 4) also reproduces the data fairly well for a range of melting extents of the high-degree melt (Fig. 25).

Variable extents of melt-mixing produce linear correlations between concentrations of any two elements. In contrast, partial melting of a homogeneous source produces curved concentration trends of elements with different degrees of compatibility; the greater the difference in compatibility, the greater the curvature. Interpreting mixing lines such as Figure 24 as variable degrees of partial melting requires a source with strong incompatible element enrichments in order to reduce the curvature of such lines (hence the postulations of incompatible element-enriched sources of previous studies). However, the isotopic variation shows that these trends are the result of melt-mixing between high- and low-degree melts of isotopically different sources, not variations in extent of partial melting of any single source (Fig. 25).

Correlations between element-pair concentrations in post-erosional magmas (when scatter is not so great as to prevent any sort of correlation) are usually quite linear (Maaløe et al., 1992; Clague and Frey, 1982). This is true even for element pairs with strong differences in degree of compatibility, supporting an origin by mixing. For example, even Th and Sr, which typically have bulk distribution coefficients in lherzolite that differ by one to two orders of magnitude, show linear covariation (Fig. 26). Both Koloa volcanics and Honolulu volcanics (the post-erosional sequence on Koolau volcano; data from Clague and Dalrymple, 1982) have fairly linear concentration covariations. Fitting a partial melting trend through this correlation that approximates the overall linear correlation would require extremely high Th and Sr concentrations (~ 0.4 and 80 ppm, respectively, or about 7.3 and 10 times chondritic, respectively) and a very large range in extent of partial melting, from about 3.5 to 35%, to explain both the Koloa and Honolulu

volcanics. Using a fractional, instead of batch, melting model would require even more extreme incompatible element source enrichment and greater extents of melting. Mixing of low- and high-degree melts from incompatible element-depleted mantle sources with depleted isotopic signatures on the other hand, explains the linear correlations and accompanying isotopic variation without calling on incompatible element-enriched source compositions that are not reflected in isotopic compositions.

Melt-mixing: Enriched mantle sources and the Chen and Frey (1983) model

Instead of relatively small degrees of melting of incompatible element-depleted mantle sources, it is possible that the melt 1 and melt 2 endmembers are derived from larger-degree melting of incompatible element-enriched mantle sources (Fig. 24c). Large degrees of melting (about 5-11%, e.g., Clague and Frey, 1982) of incompatible element-enriched sources is the generally favored model for Hawaiïan alkalic magmas, and requires recent (< 200 Ma) metasomatic source enrichment of incompatible elements (Clague & Frey, 1982; Clague & Dalrymple, 1988). A model for metasomatic enrichment of Hawaiïan mantle source regions was presented by Chen and Frey (1983, 1985). In this model small-degree melts (0.1%) from a mid-ocean-ridge-basalt-like source (MORB, $^{87}\text{Sr}/^{86}\text{Sr} = 0.7023$, $\epsilon_{\text{Nd}} = +12.9$), mix with solid mantle of a plume-like, or enriched mantle (EM, $^{87}\text{Sr}/^{86}\text{Sr} = 0.7047$, $\epsilon_{\text{Nd}} = +0.23$) source (or alternatively, large-degree melts of the EM source). Mantle regions that have been extensively metasomatized with this small-degree MORB melt then have lower $^{87}\text{Sr}/^{86}\text{Sr}$, higher ϵ_{Nd} , and higher concentrations of incompatible elements. Melting of these mantle sources then produces post-shield and post-erosional magmas with depleted isotopic signatures and enriched incompatible trace element compositions.

Figure 27 shows a variation of the Chen and Frey (1983, 1985) model with respect to $^{87}\text{Sr}/^{86}\text{Sr}$ and La/Lu (Table 4), along with $^{87}\text{Sr}/^{86}\text{Sr}$ and La/Lu of tholeiitic, post-shield alkalic, and post-erosional basalts from Kauaï, Haleakala, and Koolau volcanoes. This

figure is similar to Chen and Frey's widely utilized $^{87}\text{Sr}/^{86}\text{Sr}$ -versus-La/Ce diagram, designed to illustrate the effects of variable degrees of melting and mixing of the MORB and EM sources. Chen and Frey noted an overall trend in Hawaiian magmas, from tholeiites to post-erosionals, of increasing incompatible enrichment (and La/Lu) with progressively more depleted isotopic compositions (lower $^{87}\text{Sr}/^{86}\text{Sr}$ and higher ϵ_{Nd}). But analyses of clearly cogenetic post-erosional samples in our study shows that the *opposite* is true *within* the post-erosional series, in which magmas with enriched isotopic signatures (i.e., higher $^{87}\text{Sr}/^{86}\text{Sr}$ and lower ϵ_{Nd}) are *enriched* in incompatible elements (Fig. 27). Other post-erosional lavas, from Haleakala (Chen and Frey, 1985) and Koolau (Roden et al., 1984) volcanoes, show similar overall trends. Thus, the melt-mixing model of Chen and Frey (1983, 1985), while consistent with the overall petrogenetic evolution from tholeiites to alkalic magmas, cannot explain trace element and isotopic variability among Koloa post-erosional magmas, and possibly among Hawaiian post-erosional magmas in general.

In general, post-erosional magmas that are inferred to represent relatively large degrees of melting on the basis of major element compositions and mineralogy (i.e., alkalic basalts) typically have both the lowest $^{87}\text{Sr}/^{86}\text{Sr}$ and La/Lu, while those inferred to represent small degrees of melting (i.e., nephelinites, melilitites) have the highest $^{87}\text{Sr}/^{86}\text{Sr}$ and La/Lu (Fig. 27). This supports a relationship between the degree of melting (reflected in both major element composition and La/Lu) and the isotopic composition of the mantle source, and further suggests that La/Lu variability is more sensitive to degree of melting than solid source composition. The Chen and Frey mixing model may explain the origin of the two isotopically distinct mantle sources of the Koloa post-erosional magmas, and why the high $^{87}\text{Sr}/^{86}\text{Sr}$ (melt 1) source melts to a lower degree than the low $^{87}\text{Sr}/^{86}\text{Sr}$ (melt 2) source. Chen and Frey's preferred model involves mixing between small degree melts (high La/Lu) of the MORB source, with solid EM mantle (or large-degree melts thereof). Provided that the mixing occurred between a low-degree MORB melt and solid EM

mantle (and not a melt thereof), then the melt 2 source of post-erosionals could be a region of EM mantle that mixed with a relatively large proportion of low-degree MORB melt, and melt 1 source a region of EM mantle that mixed with a relatively small proportion of low-degree MORB melt. Assuming Lu concentrations of 0.1 and 0.054 ppm for Chen and Frey's EM and MORB sources, respectively, indicates that the melt 1 source could be produced by mixing solid EM with about 2.25% of a 0.1% MORB melt, and the melt 2 source could be produced by mixing with about 6.25% of the same MORB melt (Fig. 27). To explain trace element and isotopic compositions of post-erosional magmas, melt 1 must be produced by 1.5% melting of the melt 1 source, and melt 2 must be produced by about 15% melting of the melt 2 source. Post-erosional magmas represent a mixture between these two melts (Fig. 27). Figure 28 shows that predictions of this two stage mixing-model in the context of Sr- and Nd-isotope, and P_2O_5 and La/Lu compositions provide a good explanation for the Koloa post-erosional magmas.

While more complicated than our model of mixing melts derived from two LREE-depleted sources, the two-stage metasomatism-followed-by-melt-mixing model is appealing for two reasons. First, it provides an explanation for the contrasting isotopic compositions of the two mantle sources of post-erosional magmas within the context of the larger-scale model for Hawaiian magmatism. Second, an appealing aspect of this model is the apparent correlation between extent of mantle metasomatism (by 0.1% MORB melt) of each post-erosional mantle source in the first stage of the model, and the required degree of melting of each source. It is likely that mixing of a small-degree melt with solid mantle (i.e., metasomatism) would decrease the solidus temperature of the mantle, increasing its melt-production capacity. This model requires that the melt 2 source mixes with 2.7 times more 0.1% MORB melt than the melt 1 source, and that it melts ten times more than the melt 1 source.

TEMPORAL TRACE ELEMENT TRENDS AND THE MECHANISM OF MELT-MIXING

The temporal trace element trends within eruption sequences provide a critical constraint to the melt-mixing (or any other proposed) scenario. Mixing must occur so that lavas emerging from a monogenetic vent have decreasing proportions of the low-degree melt (melt 1) and increasing proportions of the high-degree melt (melt 2) as the eruption proceeds. This suggests a mixing mechanism associated with melt transport. The first melts to either leave the mantle source region, or migrate through the mantle, or both, in any eruption sequence, must mix with the largest proportion of melt 1. At least two possible scenarios could explain this.

One possibility is that veins or lenses of peridotite or pyroxenite with a lower solidus temperature are embedded within, or surrounded by, peridotite with a higher solidus temperature. The veins or lenses melt to a large extent, producing melt 2, while the surrounding peridotite melts to a very small extent, producing melt 1. Once aliquots of melt 2 begin to leave the source region, the melts leaving first extract most of the melt 1 present in the surrounding mantle. As more melt leaves the source region, less of the low-fraction melt 1 remains and/or is mobile, and the proportion of melt 1 in the aggregate melt leaving the source region decreases with time. In the context of the Chen and Frey model, the melt 2 source would indeed be expected to melt to a larger extent because of more extensive metasomatism by 0.1% MORB melts.

Another possibility is that as the high-degree melt (melt 2) migrates from its source through the mantle, it extracts a small-degree partial melt (melt 1) from lherzolite wallrock with a slightly higher $^{87}\text{Sr}/^{86}\text{Sr}$ and lower ϵ_{Nd} than melt 2. The earliest melts through each conduit or volume of reactive mantle produce and extract the largest proportion of melt 1; successive melt batches encounter more refractory and melt-depleted wallrock, thus mixing with progressively less melt 1. Some support for this type of melt-mantle reaction comes from mantle xenoliths and massifs. Many composite mantle xenoliths and massifs record the migration of alkalic melts through lherzolite

wallrock at fairly high mantle pressures (15-25 kbar) in the form of pyroxenite dikes and veins within lherzolite. Commonly, the peridotite adjacent to these dikes is depleted in phases or trace elements that suggest extraction of low-melt fractions (Irving, 1980; Sen, 1988). If the migrating melts that produced the pyroxenite dikes scavenged and mixed with this low-degree partial melt, the trace element and isotopic results could mimic melt-mixing, and produce the temporal trend observed in the Koloa volcanics eruption sequences. This model could also provide a mechanism for extraction of small-degree (<1%) melts of the mantle. Migration of a relatively large-degree melt through a mantle region containing a small melt fraction may effectively sweep out the small degree melt that may otherwise not segregate from its source.

In contrast to decreasing incompatible element concentrations during individual monogenetic eruptions of Koloa magmas (Fig. 17), there appears to be an overall trend of increasing incompatible elements in Lihue basin lavas in the stratigraphic section from the bottom to the top of basin (Fig. 16). If the HTZ drillhole is representative of the evolution of magmas throughout the basin, as is suggested by overall increasing P_2O_5 and TiO_2 with respect to stratigraphy throughout the basin, then the earliest lavas in the post-erosional volcanic stage in eastern Kauaï contain the largest proportion of melt 2 (high-degree melt) component, and the youngest lavas contain the largest proportion of melt 1 (low-degree melt) component. This might suggest that as the post-erosional volcanic stage progressed, the relatively fertile (large melt-fraction) melt 2 component became less abundant or more depleted in the mantle beneath eastern Kauaï, and more of the post-erosional melts were derived from the less fertile (small melt-fraction) melt 1 component mantle.

It should be emphasized that earlier models of post-erosional magmagenesis were developed without benefit of the additional temporal-compositional constraints provided by the Koloa sequences. In general, isotopic and trace element mixing models provide useful limits on mantle endmember compositions and the origin of magmatic chemical

variability. When derived from observations of samples collected from many different flows and vents whose genetic relations are not clear however, data provide little constraint on the mechanism of mixing between reservoirs. Without temporal-compositional constraints and clear knowledge of magma genetic relations, it can be difficult to distinguish between mixing of solid mantle sources, mixing of melts, or melt-solid mixing and all the inherent possibilities implied by the latter such as metasomatism, assimilation, zone-refining, etc. Obtaining sample suites of detailed sequences of magmas whose genetic relations are more certain than those of scattered samples provides additional constraints on mixing mechanisms. The temporal trace element and isotopic trends observed in the Koloa eruption sequences suggest not only that mixing likely occurs during and as a consequence of melt migration, but also that the physical characteristics of melting and melt movement play an important role in determining systematically variable magma chemical signatures.

CONCLUSIONS

Stratigraphic sequences of post-erosional lavas erupted from monogenetic vents show large, systematic changes in trace element and isotopic compositions during single eruptions. The earliest lavas to emerge in an eruption have the highest incompatible element concentrations and highest ratios of highly to moderately incompatible elements: as the eruption continues, successive lavas have progressively decreasing incompatible element abundances and decreasing ratios of highly to moderately incompatible elements. In addition to these temporal trends, there are strong correlations between incompatible trace elements and Sr- and Nd-isotope compositions, as well as among elements with varying degrees of incompatibility, both within and among eruption sequences. This indicates little or no chromatographic decoupling of trace element and isotopic compositions, which would be expected if the incompatible element enrichments and temporal trends were a consequence of diffusive equilibration of melt with solid mantle.

These observations also preclude variations in degrees of partial melting of any single homogeneous mantle source, whether depleted or enriched in incompatible elements. Simple mixing between relatively large- and small-degree partial melts derived from two mantle sources with slightly different, but both depleted, isotopic compositions reproduce these data very well. From these data it is impossible to distinguish whether the mantle sources were depleted or recently enriched in incompatible elements, but varying extents of metasomatism of solid mantle with plume-like composition by 0.1% MORB melts (i.e., the Chen and Frey, 1983 model) generate plausible incompatible element-enriched mantle sources of post-erosional magmas with appropriate trace element and isotopic compositions. Mixing between a 15% melt of the more extensively metasomatized source and a 1.5% melt of the less metasomatized source produces mixing trends that reproduce post-erosional compositions from Kaua'i, Haleakala, and Koolau volcanoes very well.

Temporal trends of decreasing incompatible elements and ratios of highly to moderately incompatible elements in sequences of erupted magmas during monogenetic eruptions strongly suggest that this melt-mixing is associated with melt migration. The first lavas to emerge during a monogenetic eruption produce and/or extract the largest proportions of the low-degree melt, and successive lavas have progressively larger proportions of the high-degree melt. One likely explanation is that post-erosional magmas extract small-degree partial melts of mantle adjacent to their source regions or migration pathways as they move from sources through the mantle.

Table 2. Major- and trace-element and isotopic compositions of samples from the HTZ drillhole, Lihue basin, Kauai'i.

HTZ drillhole sub. ID, IUPAC name	cambrian			middle			basal			massif			basal			middle			basal		
	155 95HT2155	205 95HT2205	265 95HT2265	290 95HT2290	315 95HT2315	335 95HT2335	395 95HT2395	425 95HT2425	440 95HT2440	450 95HT2450	460 95HT2460	475 95HT2475	490 95HT2490	500 95HT2500	510 95HT2510	525 95HT2525	525 95HT2525	525 95HT2525	545 95HT2545		
SiO ₂	43.02	41.73	46.32	49.97	48.32	49.56	44.47	43.09	43.15	43.06	42.67	42.27	42.24	41.54	42.52	42.30	42.14	42.28			
Al ₂ O ₃	11.48	11.88	10.34	13.85	10.35	11.83	12.24	13.65	11.72	11.36	11.37	11.11	11.33	11.35	11.42	10.69	10.59	11.47			
FeO	15.06	15.87	15.37	12.53	13.16	12.86	14.62	14.62	14.48	15.10	14.63	15.20	15.50	16.31	14.91	14.32	14.74	14.63			
CaO	0.06	0.09	0.11	0.09	0.13	0.11	0.06	0.08	0.07	0.08	0.08	0.06	0.06	0.10	0.06	0.06	0.08	0.09			
MgO	12.88	12.95	15.66	7.50	15.46	11.73	12.89	9.92	13.12	14.35	13.72	13.84	13.40	13.11	12.93	14.66	14.43	13.78			
CaO	11.78	12.23	7.93	10.06	8.34	9.00	10.41	11.20	12.05	12.40	12.22	12.12	12.15	12.23	12.43	12.08	11.21	11.91			
MnO	0.19	0.21	0.18	0.18	0.21	0.18	0.18	0.19	0.21	0.20	0.20	0.22	0.22	0.23	0.21	0.20	0.20	0.20			
Na ₂ O	1.09	0.46	1.66	2.28	1.45	1.87	1.15	1.12	0.86	1.05	0.82	1.01	0.88	0.85	1.34	1.97	2.79	1.86			
K ₂ O	0.82	0.18	0.19	0.28	0.35	0.42	0.86	0.93	0.44	0.76	0.57	0.40	0.44	0.45	0.57	0.42	0.66	0.41			
P ₂ O ₅	3.19	3.73	1.99	2.82	2.01	2.45	2.42	2.81	2.75	2.74	2.77	2.86	3.04	3.10	2.83	2.60	2.55	2.71			
P ₂ O ₅	0.60	0.67	0.24	0.38	0.25	0.28	0.44	0.52	0.59	0.63	0.63	0.71	0.76	0.74	0.68	0.68	0.65	0.67			
Si	776	439	291	380	284	313	826	727	730	580	736	707	705	764	654	727	829	609			
Sc	218	251	208	252	199	212	219	218	209	210	211	204	215	224	216	211	20.6	21.1			
V	316	349	206	286	207	272	277	265	278	272	284	272	290	292	282	280	286	279			
Cr	290	333	437	281	426	362	334	209	221	297	222	302	286	259	360	357	292	317			
Co	59	56	87	56	58	49	58	46	54	58	57	59	61	59	68	61	59	59			
Ni	314	282	649	241	571	423	308	318	303	343	322	334	352	358	354	353	363	369			
Cu	63.5	61.4	68.2	92.3	59.5	65.3	68.2	85.6	71.3	71.2	68.5	65.6	69.6	65.5	61.8	74.0	77.9	72.0			
Zn	114	89.1	100	92	85.7	82.9	97.3	91.9	94.6	106	98.2	97.9	96	103	92.8	108	95.2	96.3			
Y	21.7	22.0	18.6	23.3	15.8	17.8	19.7	20.9	20.3	20.4	21.0	20.7	22.0	23.8	22.0	21.9	21.0	21.6			
Zr	191	154	91.7	142	101	111	141	159	158	159	167	134	174	179	168	167	167	165			
Ba	616	521	114	120	129	121	470	506	518	505	532	499	492	537	555	504	516	431			
Th	4.4	5.0	1.0	1.3	0.8	1.2	3.3	3.6	4.4	4.8	4.7	4.8	4.9	5.0	5.2	4.7	4.9	4.5			
La	37.5	40.5	12.0	15.4	10.9	14.1	28.8	32.2	38.6	42.1	39.6	42.4	44.4	46.4	47.3	40.9	44.3	41.2			
Ce	78.5	84.6	30.0	37.7	28.1	35.0	63.3	70.1	88.4	78.5	85.3	90.6	92.7	93.8	100.0	86.4	97.0	86.6			
Pr	9.9	10.8	4.3	5.5	3.8	4.8	8.0	8.7	10.0	9.6	10.5	11.0	11.5	11.5	12.3	10.5	11.5	10.7			
Nd	40.0	43.1	19.2	24.5	18.8	21.2	31.5	35.4	41.7	43.9	40.1	44.4	47.1	47.6	49.2	42.6	46.4	43.2			
Sm	10.2	10.4	5.6	7.3	4.8	6.3	8.1	8.9	9.9	11.0	9.9	10.7	11.3	11.4	12.1	10.3	11.5	10.7			
Eu	3.17	3.16	1.78	2.40	1.51	2.01	2.84	2.60	3.03	3.29	2.92	3.14	3.22	3.35	3.64	3.05	3.28	3.09			
Gd	8.8	9.1	5.2	6.7	4.6	5.6	6.5	7.6	8.6	9.1	8.3	8.6	9.1	9.7	9.3	10.0	9.1	8.8			
Tb	1.1	1.1	0.8	1.0	0.7	0.8	0.9	1.0	1.1	1.2	1.1	1.2	1.3	1.2	1.1	1.1	1.2	1.2			
Dy	6.4	6.3	4.7	5.9	4.1	5.1	5.5	5.9	6.2	6.6	6.4	6.4	6.8	6.5	6.9	6.9	6.7	6.4			
Er	2.4	2.5	2.1	2.8	1.9	2.3	2.2	2.4	2.3	2.6	2.2	2.3	2.6	2.5	2.3	2.3	2.3	2.3			
Tm	0.3	0.3	0.3	0.3	0.2	0.3	0.3	0.3	0.3	0.3	0.3	0.3	0.3	0.3	0.3	0.3	0.3	0.3			
Yb	1.6	1.7	1.1	1.7	1.1	1.9	1.6	1.5	1.6	1.6	1.6	1.6	1.6	1.6	1.7	1.5	1.6	1.6			
Lu	0.21	0.22	0.22	0.28	0.19	0.23	0.19	0.23	0.21	0.18	0.21	0.19	0.20	0.20	0.20	0.19	0.19	0.19			
⁸⁷ Sr/ ⁸⁶ Sr	0.703262	0.703060	0.703709	0.703748	0.703782	0.703777	nd	0.703295	0.703325	0.703282	0.703306	0.703322	0.703345	nd	0.703321	0.703346	nd	0.703355			
¹⁴³ Nd/ ¹⁴² Nd	0.512969	0.513062	0.512912	0.512929	0.512939	0.512921	nd	0.512982	0.512975	0.512995	0.512984	0.512976	0.512964	nd	0.512992	0.512960	nd	0.512978			
f _{Lu}	7.04	8.27	5.34	5.67	5.86	5.52	nd	6.71	6.57	6.97	6.88	6.60	6.36	nd	6.90	6.79	nd	6.85			

Table 2 (continued).

Sample Name	580	615	640	660	705	665	680	690	905	915	925	935	950	960	975	980	985	990	995	1000
	95HT2540	95HT2615	95HT2640	95HT2690	95HT2705	95HT2645	95HT2690	95HT2700	95HT2705	95HT2715	95HT2725	95HT2735	95HT2740	95HT2750	95HT2760	95HT2770	95HT2785	95HT2790	95HT2795	95HT2800
SiO ₂	44.33	43.52	43.22	44.37	42.47	43.03	44.06	44.27	44.63	44.84	44.94	44.50	44.80	43.82	44.11	43.90	44.33	44.20	44.39	44.34
Al ₂ O ₃	12.31	11.99	12.48	13.16	11.75	12.17	10.41	10.47	12.06	13.04	12.89	11.90	12.08	11.36	11.68	11.66	12.13	13.19	12.82	11.70
Fe ₂ O ₃	0.11	0.10	0.09	0.10	0.07	0.11	0.18	0.16	0.13	0.07	0.11	0.10	0.10	0.11	0.12	0.11	0.11	0.11	0.09	0.09
MgO	14.36	14.54	14.66	13.64	14.43	14.54	16.23	16.40	15.90	15.05	14.74	15.70	14.75	15.10	14.48	14.97	14.53	15.36	14.94	14.20
CaO	9.98	11.54	11.65	10.96	12.37	13.59	15.35	15.54	12.41	11.13	11.93	13.97	13.54	16.26	14.67	14.80	14.29	11.31	11.54	14.47
MnO	0.20	0.19	0.16	0.16	0.20	0.24	0.21	0.18	0.19	0.18	0.19	0.21	0.20	0.20	0.20	0.20	0.20	0.20	0.20	0.20
NiO	1.24	1.21	1.49	1.34	2.24	1.39	0.75	0.83	1.21	1.53	1.64	1.27	1.26	1.04	1.15	1.08	1.23	1.26	1.29	1.36
K ₂ O	0.54	0.58	0.81	0.81	0.84	0.69	0.34	0.35	0.50	0.54	0.61	0.55	0.60	0.56	0.55	0.51	0.60	0.65	0.69	0.83
TiO ₂	2.10	2.58	2.87	2.81	2.80	2.54	1.71	1.78	2.03	2.18	2.16	1.86	2.08	1.86	2.11	2.12	2.12	2.82	2.50	2.14
P ₂ O ₅	0.28	0.55	0.65	0.41	0.65	0.44	0.22	0.19	0.23	0.30	0.36	0.26	0.28	0.26	0.30	0.30	0.31	0.32	0.34	0.51
Br	330	489	718	589	809	548	192	205	302	355	432	375	388	281	370	383	389	482	445	430
Bc	224	246	255	245	232	166	317	282	280	245	239	231	244	216	237	227	225	237	235	229
V	264	297	334	304	309	243	281	252	294	305	303	283	306	272	295	285	280	319	311	293
Cr	268	325	351	423	282	222	515	527	377	296	241	338	301	464	425	280	257	289	276	373
Co	57	56	58	53	56	44	61	61	62	53	59	63	61	62	61	65	60	54	53	61
Ni	358	292	302	259	278	398	477	390	352	251	297	371	339	391	360	309	348	291	274	355
Cu	72.0	79.0	80.0	76.3	75.6	38.8	56.9	46.6	69.2	61.1	76.7	73.3	60.9	69.1	70.3	73.4	78.1	77.7	77.5	74.4
Zn	96.3	85.6	105	107	110	69.6	66	78.4	93.6	94.3	102	91.1	97.2	83.4	89.1	91.8	92	90.8	94.9	87.8
Y	15.9	16.1	22.4	20.1	23.7	19.5	15.9	13.6	16.8	18.2	18.4	10.7	16.9	14.8	16.3	16.3	16.8	18.3	18.0	16.8
Zr	100	137	170	77.7	167	77.7	83	73.7	91	98.5	108	96.2	98.3	92.7	104	96.6	105	115	114	108
Ba	234	433	543	483	594	211	158	146	242	302	322	278	275	277	315	301	382	340	341	321
Th	3.0	4.4	4.4	3.3	4.4	1.9	1.5	1.4	1.7	2.2	2.1	2.0	1.8	1.8	2.1	2.2	2.4	2.5	2.2	2.2
La	181	249	364	278	383	191	140	135	167	190	188	179	158	173	182	190	198	238	220	206
Ce	493	543	77.1	591	80.4	42.4	30.7	36.6	42.8	41.5	39.8	34.8	36.7	36.1	41.6	43.3	47.5	47.5	48.2	46.0
Pr	5.1	6.7	9.3	7.2	9.6	5.5	3.9	3.6	4.8	5.1	5.0	4.6	4.6	4.8	5.2	5.5	6.0	6.3	5.8	5.8
Nd	211	273	368	295	370	247	168	168	197	220	218	208	192	200	194	215	231	259	252	230
Sm	58	71	94	7.6	9.3	6.4	4.5	4.9	5.7	6.1	5.9	5.6	5.1	5.5	5.3	6.0	6.9	6.9	6.6	6.6
Eu	186	218	285	235	263	194	150	164	174	185	180	163	168	161	179	169	203	212	204	204
Gd	5.2	6.1	7.7	5.8	7.7	5.8	4.4	4.4	5.0	5.5	5.5	5.1	4.9	4.8	4.8	5.1	5.3	6.0	5.8	5.4
Tb	0.7	0.9	1.1	0.9	1.0	0.9	0.6	0.7	0.7	0.8	0.8	0.8	0.7	0.7	0.7	0.7	0.8	0.9	0.8	0.8
Dy	4.5	4.8	6.2	5.6	5.9	4.8	3.7	3.6	4.4	5.0	4.7	4.5	4.2	4.0	4.5	4.5	4.9	5.0	5.1	4.7
Er	2.0	2.0	2.2	2.3	2.3	2.2	1.6	1.6	2.0	2.2	2.0	1.8	1.9	1.7	2.0	2.1	2.2	2.1	2.2	2.0
Tm	0.2	0.3	0.3	0.3	0.2	0.3	0.2	0.2	0.3	0.3	0.2	0.3	0.2	0.2	0.2	0.3	0.3	0.3	0.3	0.2
Yb	1.5	1.7	1.7	1.7	1.6	1.8	1.2	1.4	1.5	1.7	1.6	1.6	1.4	1.4	1.4	1.5	1.6	1.6	1.7	1.6
Lu	0.22	0.19	0.22	0.24	0.21	0.22	0.18	0.17	0.19	0.22	0.20	0.22	0.21	0.20	0.20	0.21	0.21	0.21	0.23	0.19
⁸⁷ Sr/ ⁸⁶ Sr	0.703183	0.70296	0.703117	0.703120	0.703145	nd	0.703365	nd	0.703147	nd	0.703147	nd	0.703161	nd	0.703117	0.703066	0.703113	0.703173	0.703137	0.703092
¹⁴³ Nd/ ¹⁴⁴ Nd	0.513055	0.513071	0.513026	0.513054	0.513060	nd	0.513061	nd	0.513055	nd	0.513056	nd	0.513074	nd	0.513058	0.513070	0.513056	0.513031	0.513075	0.513056
ϵ_{Nd}	6.13	6.44	7.57	6.11	6.23	nd	6.28	nd	6.14	nd	7.77	nd	6.51	nd	6.20	6.42	6.16	7.67	6.52	6.15

Notes: Fluxed samples are interpreted as single eruption sequences, based on lack of alluvial or sedimentary interbeds, and petrography, chemistry, & isotopic compositions of samples

All major element oxides reported as weight %, volatile-free. Fe₂O₃ is total iron

Isotopic analyses performed at University of Washington, using procedures described in Nelson (1995). Subsamples analysed for neotopes were leached for 1.5 hours in 6.2 N HCl in an ultrasonic bath to avoid weathering effects on Sr- and Nd-isotope compositions. ϵ_{Nd} is deviation of (¹⁴³Nd/¹⁴⁴Nd) from that of inferred bulk earth (0.512638). ϵ_{Nd} = [(¹⁴³Nd/¹⁴⁴Nd)_{sample}/0.512638 - 1] × 10⁴. Analytical error (2σ) of isotopic analyses is +/- in last digit of ratio. Long-term reproducibility of Sr and Nd isotopic measurements are 41 ppm and 26 ppm (2σ), respectively. NBS 987 yields an average ⁸⁷Sr/⁸⁶Sr = 0.710266 (n=85 over 2 yrs) and La Jolla Nd averages, ¹⁴³Nd/¹⁴⁴Nd = 0.511841 (n=34 over 2 yrs)

Table 3. Major- and trace-element and isotopic compositions of samples from Lae O Kilauea vent, Kaua'i.

relative stratigraphic height	<u>3 (bottom)</u>	<u>4</u>	<u>6</u>	<u>8</u>	<u>10</u>	<u>12</u>	<u>14</u>	<u>16 (top)</u>
sample name	94PRKP3	94PRKP4	94PRKP6	94PRKP8	94PRKP10	94PRKP12	94PRKP14	94PRKP16
SiO ₂	43.46	43.82	43.14	44.73	44.03	43.74	43.51	43.94
Al ₂ O ₃	12.47	12.59	12.21	14.13	14.18	15.01	13.35	13.36
Fe ₂ O ₃	15.22	15.42	15.18	17.94	16.98	17.99	16.00	16.29
Cr ₂ O ₃	0.06	0.16	0.10	0.11	0.09	0.10	0.09	0.09
MgO	11.94	11.98	13.17	11.50	11.06	10.73	11.85	12.23
CaO	11.83	10.86	11.51	5.51	7.82	6.74	9.93	8.86
MnO	0.21	0.21	0.21	0.24	0.24	0.23	0.20	0.23
Na ₂ O	1.37	1.59	1.10	1.89	1.67	1.24	1.31	1.16
K ₂ O	0.27	0.24	0.29	0.48	0.49	0.44	0.48	0.54
TiO ₂	2.70	2.66	2.65	3.19	2.97	3.22	2.83	2.84
P ₂ O ₅	0.47	0.48	0.45	0.51	0.47	0.55	0.44	0.47
Sr	695	661	684	682	639	503	529	549
Sc	24.5	23.5	23.8	27.5	27.0	27.8	26.2	25.7
V	366	323	342	254	314	295	289	298
Cr	396	273	409	387	419	325	335	317
Co	67	63	65	73	72	70	66	71
Ni	372	365	388	434	424	443	400	473
Cu	96.8	95.3	84.1	103.0	95.3	83.0	91.9	86.0
Zn	101	103	121	124	121	122	107	115
Y	22.0	21.9	21.5	21.2	23.0	25.1	25.3	26.7
Zr	144	98.6	130	136	149	151	139	135
Ba	695	690	701	799	620	828	990	837
Th	4.0	4.1	4.2	4.6	4.4	4.7	4.1	4.2
La	30.5	30.8	31.2	33.5	34.2	34.8	32.2	35.0
Ce	62.8	61.7	63.2	62.8	69.0	62.3	60.6	64.0
Pr	7.5	7.5	7.6	8.0	8.3	8.4	8.0	8.3
Nd	29.9	30.3	30.4	31.4	33.6	33.6	31.8	33.1
Sm	7.7	7.8	7.8	8.3	8.6	8.5	8.1	8.6
Eu	2.32	2.40	2.47	2.58	2.84	2.71	2.48	2.60
Gd	6.8	6.7	6.8	6.8	7.1	7.6	7.2	7.8
Tb	0.9	1.0	0.9	1.0	1.0	1.0	1.0	1.0
Dy	5.4	5.4	5.4	5.2	6.1	6.1	5.8	6.0
Er	2.2	2.3	2.2	2.2	2.2	2.5	2.5	2.6
Tm	0.3	0.3	0.3	0.3	0.3	0.3	0.3	0.3
Yb	1.7	1.8	1.7	1.5	1.8	1.9	1.8	1.9
Lu	0.21	0.22	0.24	0.22	0.23	0.27	0.26	0.26
⁸⁷ Sr/ ⁸⁶ Sr	0.703212	0.703260	0.703223	0.703257	0.703200	0.703290	0.703196	0.703226
2σ	7	7	8	10	7	7	7	8
¹⁴³ Nd/ ¹⁴⁴ Nd	0.513040	0.513041	0.513040	0.513030	0.513039	0.513037	0.513041	0.513037
2σ	6	5	9	8	7	7	8	7
E _{Nd}	7.83	7.86	7.85	7.65	7.82	7.78	7.87	7.79

Notes: All major element oxides reported as weight %, volatile-free. Fe₂O₃ is total iron. Analytic procedures and isotopic accuracy as in Table 2.

Table 4. Melting and melt-mixing model parameters.

Modal proportions				
Phase	herzolite	herz. melting mode	pyroxenite	px. melting mode
olivine	0.65	0.1	0	0
orthopyroxene	0.24	0.1	0	0
clinopyroxene	0.06	0.4	0.75	0.5
garnet	0.05	0.4	0.25	0.5

Distribution coefficients^a				
element	olivine/liq	opx/liq	cpx/liq	garnet/liq
La	0.00045	0.00125	0.037	0.007
Nd	0.00115	0.00435	0.15	0.087
Lu	0.00315	0.049	0.235	5.6
P ₂ O ₅	0.001	0.01	0.02	0.1
Sr	0.0015	0.016	0.1	0.008

Compositions (ppm, except P₂O₅: wt.%)						
element	depleted herzolite ^b	pyroxenite ^c	MORB ^d	EM ^e	melt 1 source ^f	melt 2 source ^f
La	0.206	0.7	0.206	0.71	1.81	3.77
Nd	0.815	1.8	0.815	1.2	2.32	4.30
Lu	0.054	0.16	0.054	0.1	0.08	0.09
P ₂ O ₅	0.008	0.02	0.002	0.02	0.024	0.031
Sr	13.2	25	13.2	23.7	47.4	89.5
⁸⁷ Sr/ ⁸⁶ Sr	0.70295	0.70335	0.7023	0.7047	0.70290	0.70347
ε _{Nd}	+9.5	+6.5	+12.0	+0.23	+8.92	+6.04

^aREE K_d's are averages of those of McKenzie and O'Nions (1991) and Frey et al. set 3 (1977). P₂O₅ and Sr are averages of data compilations from Green (1994).

^bREE from McKenzie and O'Nions (1991). Sr from MORB source of Chen and Frey (1983, 1985). P₂O₅, ⁸⁷Sr/⁸⁶Sr and ε_{Nd} chosen to produce appropriate mixing trends in the incompatible element-depleted sources mixing model.

^cConcentrations chosen to be close to average concentrations in Hawaiian pyroxenite xenoliths (Frey, 1980) and other garnet pyroxenites (Hirschmann and Stolper, 1996) and to satisfy mixing trends.

^dREE from McKenzie and O'Nions (1991). ⁸⁷Sr/⁸⁶Sr from Chen and Frey (1983, 1985). ε_{Nd} of Chen and Frey is +12.9, adjusted to +12.0 here to agree with mixing trend. P₂O₅ is arbitrarily chosen to be ten times less than P₂O₅ of EM.

^eAll concentrations except P₂O₅ and Lu are from Chen and Frey (1983, 1985). Lu is 2 times chondrites, P₂O₅ is chosen to agree with mixing trends (but is similar to Chen and Frey's 0.031 wt.%).

^fInferred mantle sources for incompatible element-enriched mantle sources model; produced by mixing 0.1% nonmodal batch melt of MORB with solid EM in proportions of 2.25:98.75 (melt 1) and 6.25:93.75 (melt 2) similar to the Chen and Frey (1983, 1985) model (see Fig. 27).

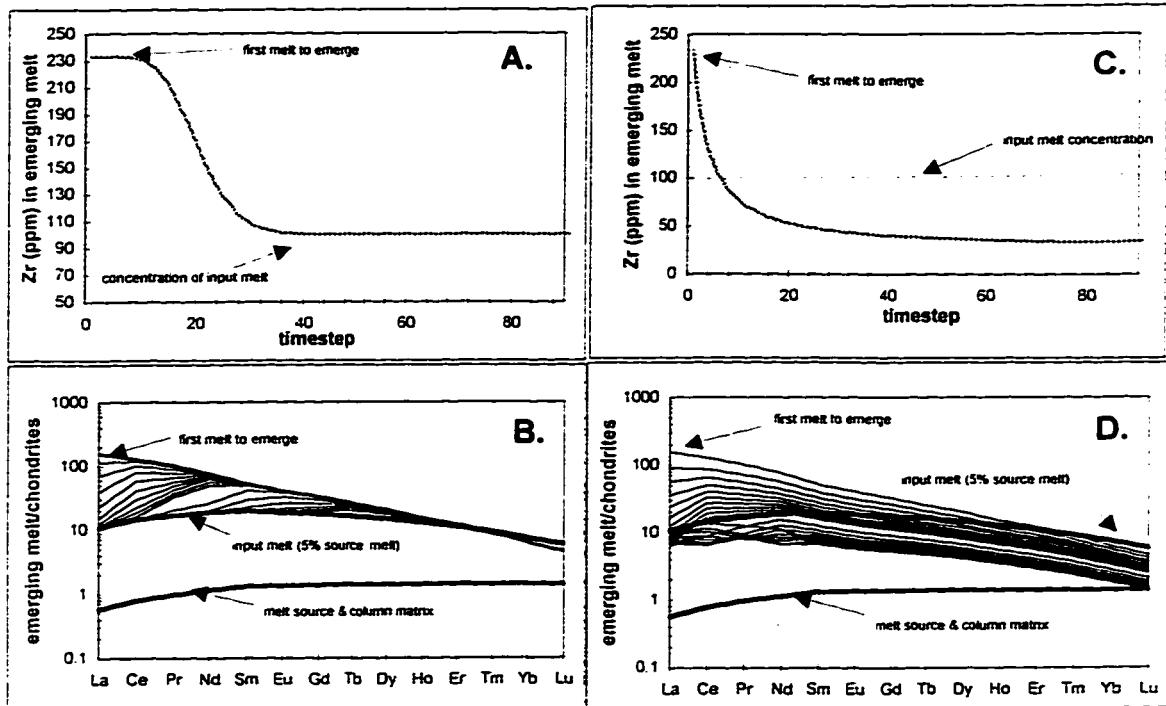


Figure 13. Example of geochemical predictions of reactive melt transport, with and without mineralogic reaction.

Plots show concentrations of Zr and rare earth elements (REE) in melts emerging from a reactive mantle column. Input melt is 5% batch melt of garnet lherzolite with typical depleted mantle trace element concentrations; initial mantle matrix is same mode and composition as melt source. **A.** Zr concentrations in melt batches emerging from reactive mantle column; melt-mantle reaction is purely diffusive exchange (no mineralogic reaction). Early melts to emerge are strongly enriched in Zr. Successive melt batches have decreasing Zr, as the matrix reactive capacity is exhausted. Eventually all melt flows through the column unchanged. **B.** Rare earth element (REE) compositions of melt batches emerging from the column, purely diffusive exchange. The first melt to emerge from the column is strongly LREE-enriched. Successive melt batches have decreasing REE, and eventually return to input melt concentrations as melt exhausts the reactive capacity of the matrix, but the most incompatible (LREE) elements return to input concentrations first, followed by progressively more compatible elements. This is the chromatographic effect that generates strongly LREE-depleted patterns.

Fig. 13 (continued). **C.** Zr concentrations in melt batches emerging from reactive mantle column where, in addition to diffusive exchange, the mode of the matrix is changing from lherzolite to pyroxenite as a result of melt-mantle reaction. The first melt to emerge is strongly enriched in Zr, and successive melt batches have concentrations that decrease even below the input value; eventually the concentrations in emerging batches return to the input values as the reactive capacity of the matrix is exhausted. **D.** Rare earth element (REE) compositions of melt batches emerging from the column under conditions of diffusive exchange with lherzolite to pyroxenite reaction. The first melt to emerge from the column is strongly LREE-enriched and successive melt batches have decreasing REE abundances, with parallel patterns, reflecting the partitioning of MREE and HREE into precipitating pyroxenes and garnet in the matrix. This mineralogic reaction partly masks the REE chromatographic effects (although some effect is still observed for La concentrations).

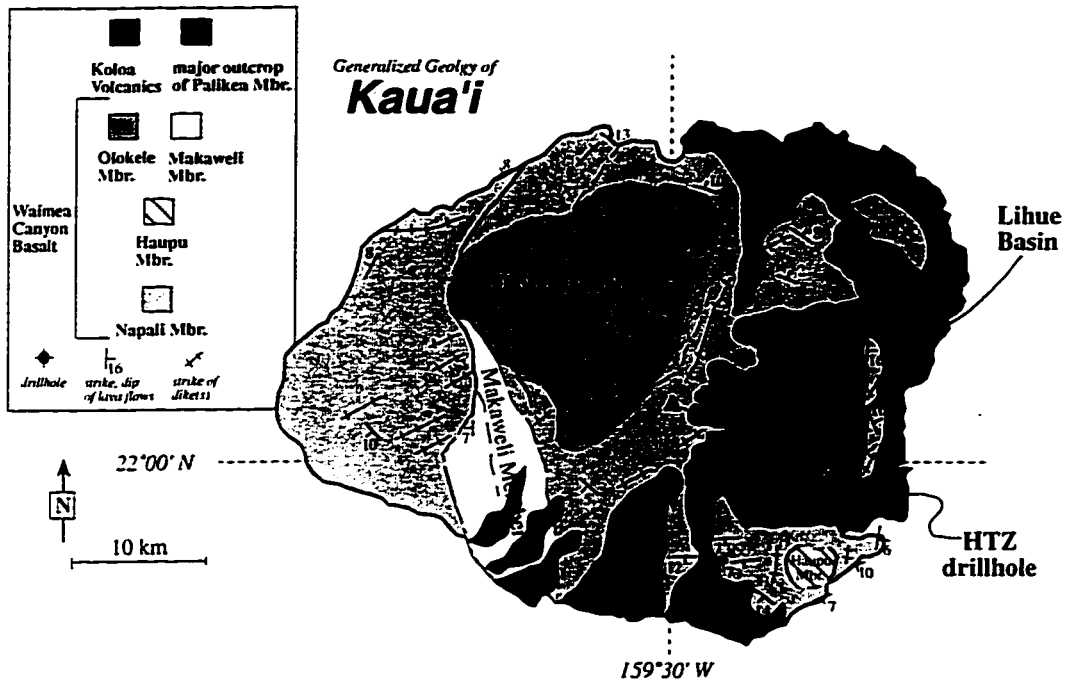


Figure 14. Generalized geologic map of Kaua'i.

Geologic map of Kaua'i (after MacDonald et al., 1960; Clague and Dalrymple, 1988) showing the primary lithologies and locations of the Lae O Kilauea vent and drillholes (including the HTZ drillhole) in the Lihue basin. The main shield and post-shield alkalic stage volcanics are termed the Waimea Canyon Basalt, and include the Napali member tholeiitic lavas, and the ponded lavas of the Olokele, Makaweli, and Hauptu members. The Hauptu member contains tholeiitic lavas ponded within a small caldera in the southeast part of the island. The Olokele and Makaweli members are dominantly tholeiites, with at least several hawaiite flows in the uppermost sections. Lavas of the Olokele member form a high, erosion-resistant plateau, bounded in some places by faults, and have been interpreted as the remnants of a central caldera. Lavas of the Makaweli member have flowed from the northeast, down into a graben-like valley, where they ponded (MacDonald et al., 1960). The post-erosional Koloa volcanics are mainly restricted to the central and eastern parts of the island, although a few flows are found in the western parts. They reach great thicknesses in the eastern part of the island, especially in the Hanalei river valley and in the Lihue basin, where the HTZ drillhole samples of this study were recovered. The Lae O Kilauea vent is a large, deeply-eroded post-erosional crater on the northeast side of the island, that erupted nephelinitic tuffs and lavas. A cross-section through the trace of A to A' is shown in Figure 15.

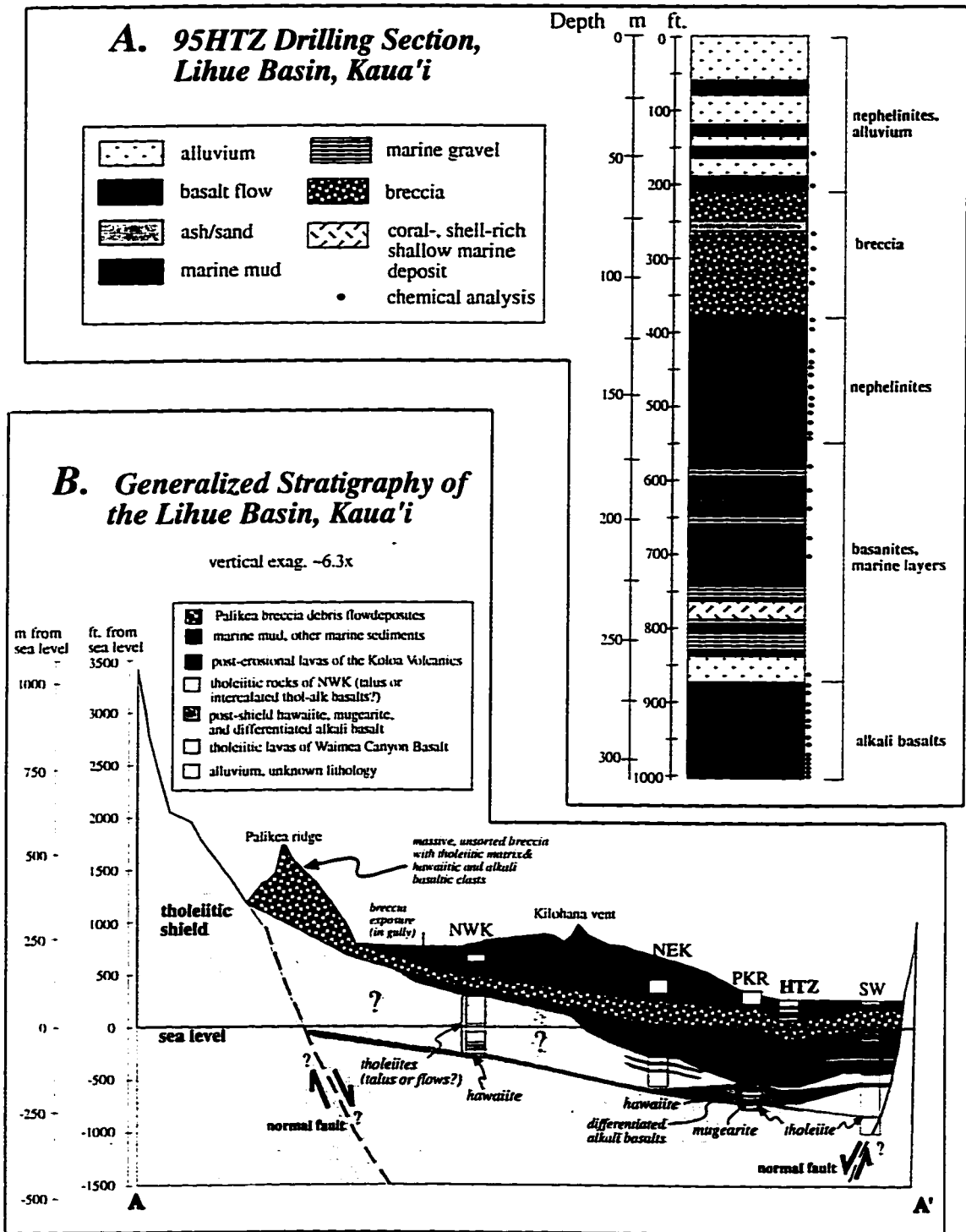


Figure 15. Stratigraphy of the HTZ drillhole and the Lihue basin.

A. Stratigraphic section of the HTZ drillhole, inferred from well-log, chemical and isotopic analyses, and thin-section petrography.

Fig. 15 (continued). Five main lithologies, shown to the right of the section, constitute the basin-fill in this region. Sequences of lavas lacking unconformities above and below, and thus representing individual eruption sequences are the a) alkali basalts from 268-305 m, b) basanites between 207-215 m, and c) nephelinites between 117-166. A thick section of breccia, correlated with surficial outcrops, is observed between about 67-113 m, and includes clasts of hawaiite with fine- to medium grained gabbroic textures, ranging from 1 mm to 5 m in diameter, within a tholeiitic matrix. This breccia is interpreted as a debris flow, and is distinct from other sedimentary interbeds within the Koloa volcanics. Interbedded with the basanites, from about 167-260 m, are marine muds and gravels containing coral and mollusk fragments. **B.** Generalized stratigraphic section of the Lihue basin through A-A' in Figure 30, based on petrography and chemical compositions of samples from drillholes shown in Figure 30. Some of the more interesting features of the basin include tholeiitic and/or hawaiitic lavas at the base of several holes, thick sections of tholeiitic rocks (interpreted as talus breccia) overlying the hawaiite in the western part of the basin, the continuity and correlation with surficial outcrops of the debris flow layer, and the apparently extremely steep boundary between tholeiitic lavas and other lithologies on the west side of the Kalepa ridge (far eastern margin of the basin). A collapse origin for the Lihue basin is required by the presence of hawaiite lavas in the bottom of the basin (Chapter 3).

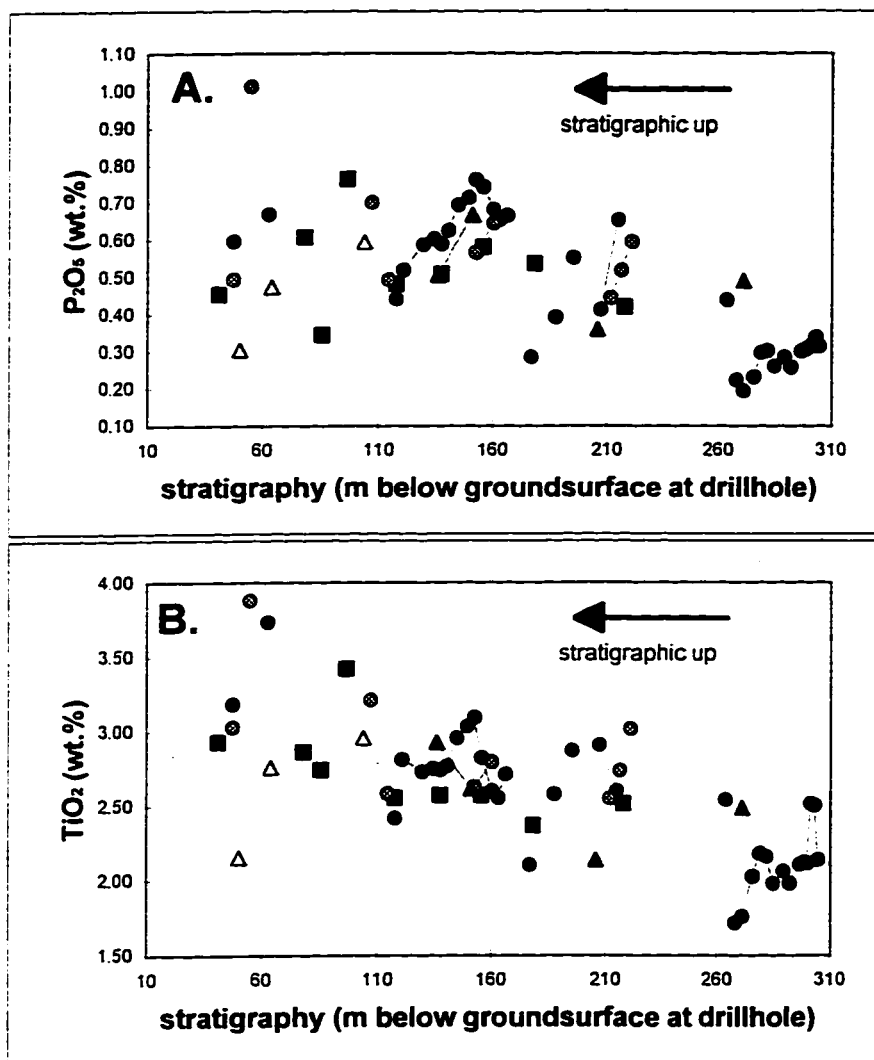


Figure 16. P_2O_5 and TiO_2 (wt.%) in Koloa Volcanics in the Lihue basin.

Weight percent P_2O_5 (A.) and TiO_2 (B.) in Koloa volcanics lavas from five drillholes in the Lihue basin (tholeiites, hawaiiites, and alluvium not included), versus stratigraphic position (feet below ground surface at each drilling site). There is a gradual decrease in concentrations of P_2O_5 and TiO_2 (and other incompatible elements) with increasing height in the basin. This suggests an overall sequence of decreasing degrees of partial melting with time, to produce the lavas that filled the basin. Symbols: Hanamaulu (HTZ) drillhole, black circles; Puakukui Reservoir (PKR), grey circles; South Wailua (SW), black squares; Northwest Kilohana (NWK), open triangles; Northeast Kilohana (NEK), black triangles.

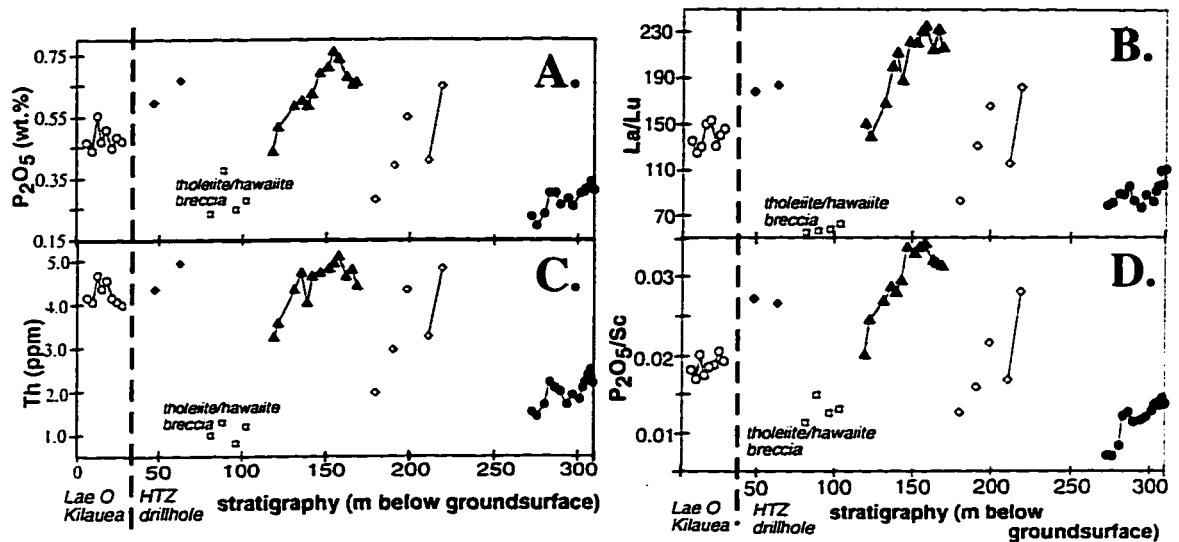


Figure 17. Concentrations of incompatible elements and ratios of highly to moderately incompatible elements, with respect to stratigraphic position in the HTZ and Lae O Kilauea sections.

A. P_2O_5 (wt.%), B. La/Lu (ppm/ppm), C. Th (ppm), D. P_2O_5/Sc (wt.%/ppm). Stratigraphic position is feet below ground surface for HTZ drillhole, and stratigraphic position relative to the youngest sample collected for Lae O Kilauea section; stratigraphic up is to the left in all plots. Samples from individual eruption sequences are joined by solid black lines. Concentrations of incompatible elements decrease with decreasing stratigraphic depth in lavas from individual eruptions in three out of the four eruption sequences. Ratios of highly to moderately incompatible elements decrease during individual eruptions in all eruption sequences. Symbols within HTZ drillhole section are: alkalic basalts, black circles; basanites, white diamonds; nephelinites below tholeiitic breccia, black triangles; tholeiitic breccia, white squares; nephelinites above breccia, black diamonds. Samples from Lae O Kilauea are white circles.

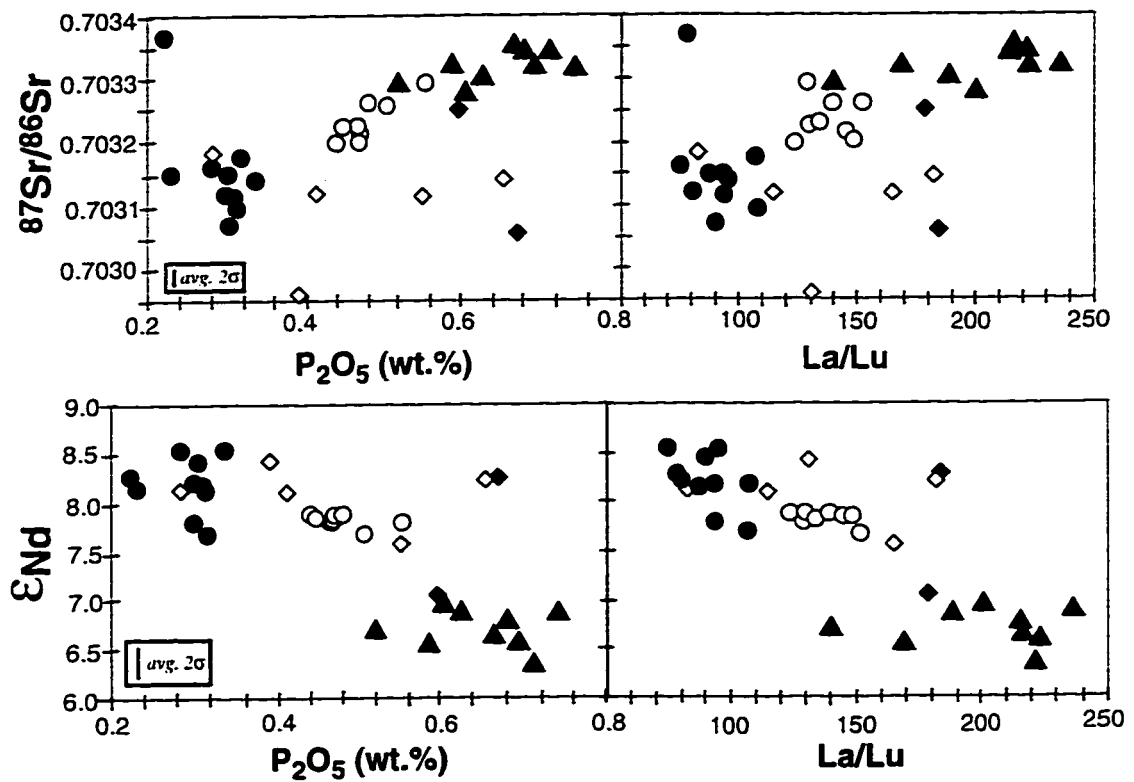


Figure 18. Sr- and Nd-isotope compositions of Koloa lavas.

Symbols as in Figure 17. There is a consistent correlation between trace element and isotopic compositions; samples with higher incompatible element abundances and higher ratios of highly to moderately incompatible elements have higher $^{87}\text{Sr}/^{86}\text{Sr}$ and lower ϵ_{Nd} .

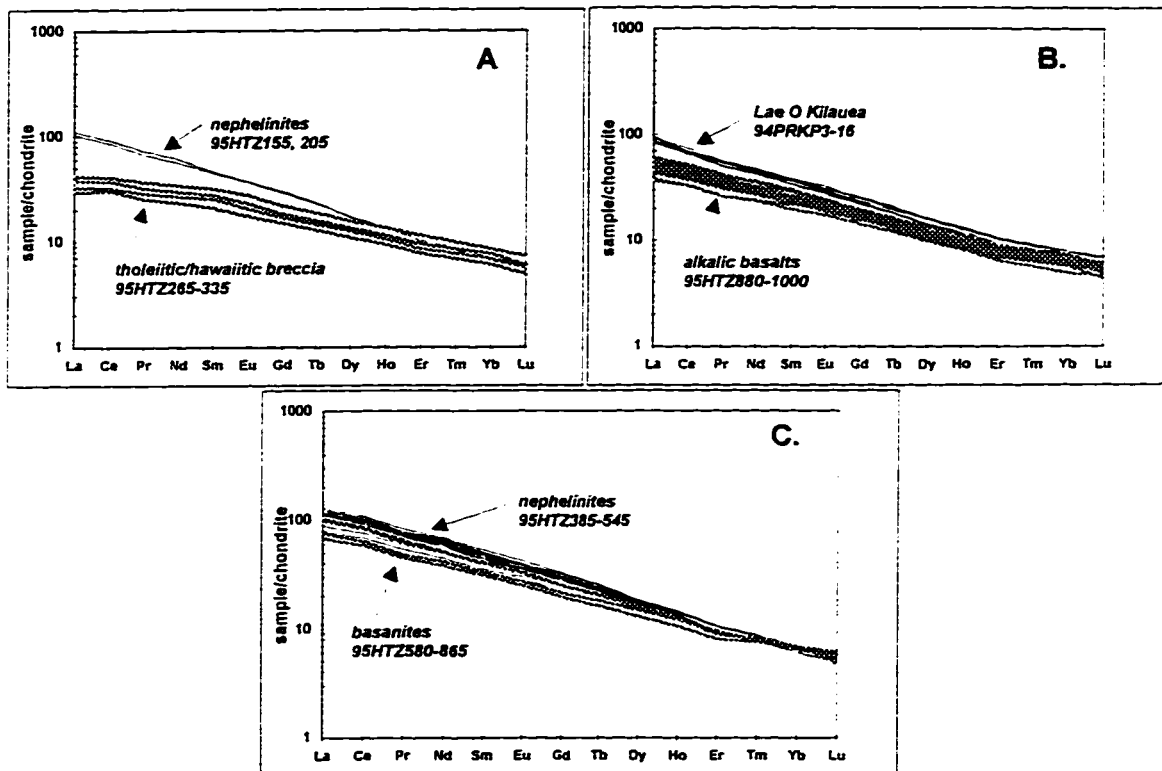


Figure 19. Rare earth element (REE) compositions of Koloa samples and tholeiitic/hawaiitic breccia.

Compositions are normalized to chondrites (normalization values from McKenzie and O'Nions, 1991). For clarity, the six main eruptive sequences are shown in three different diagrams. All Koloa samples are strongly LREE-enriched, and samples from within individual eruptions have similar REE abundances and patterns.

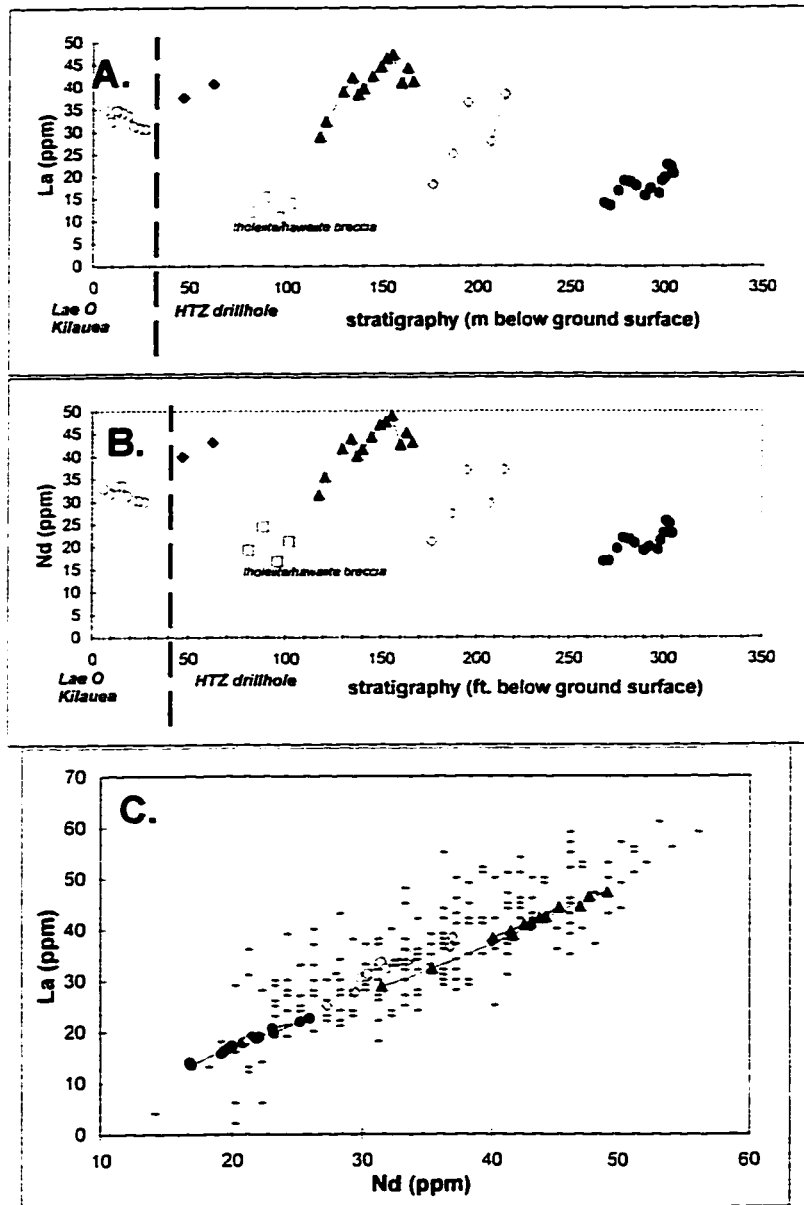


Figure 20. La and Nd concentrations of Koloa lavas.

Symbols as in Figure 17. **A.** La (ppm) versus stratigraphic position. **B.** Nd (ppm) versus stratigraphic position. Both La and Nd systematically decrease in three out of four eruption cycles. **C.** La vs. Nd (both ppm) for these samples, as well as other Koloa samples (black rectangles) from the literature (Maaløe et al., 1992; Clague and Dalrymple, 1988; Feigenson, 1984). La and Nd concentrations are highly linearly correlated in these Koloa magmas.

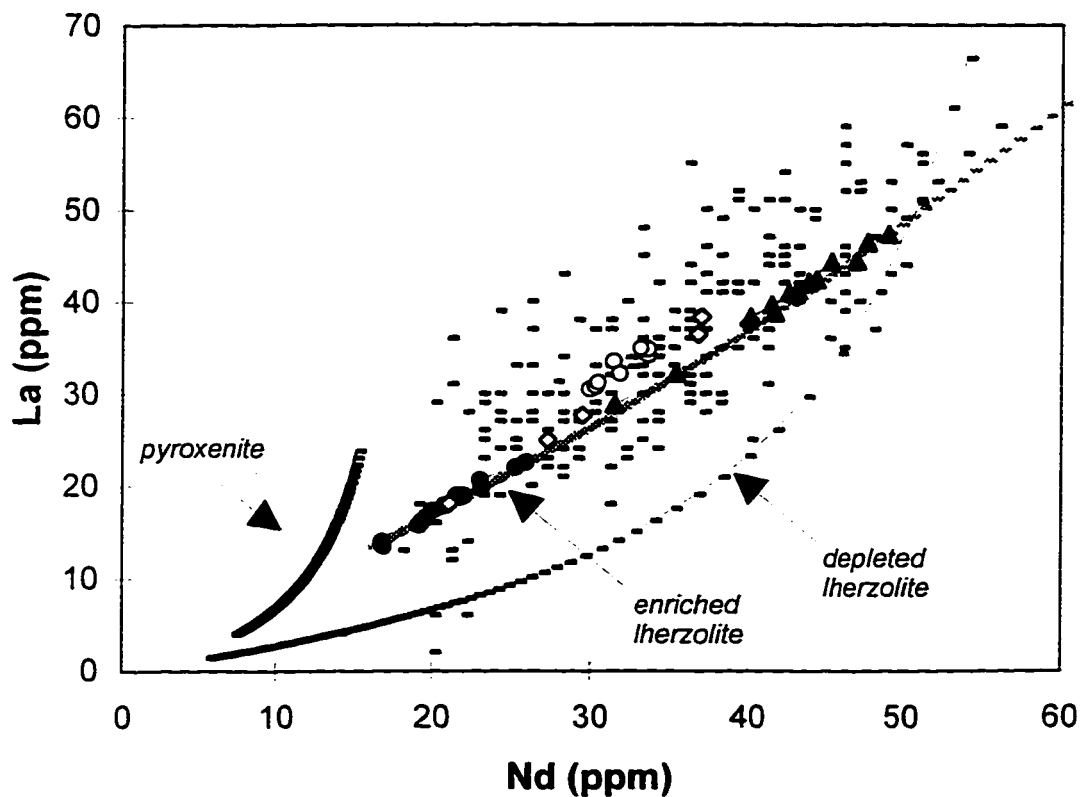


Figure 21. La and Nd concentrations of Koloa samples and non-modal batch partial melts of garnet lherzolite and pyroxenite.

Symbols as in Fig. 17. Both lherzolite and pyroxenite are assumed to have typical depleted mantle compositions for each lithology (see Table 4). Also shown is non-modal batch partial melting trend of garnet lherzolite with the enriched trace element composition of the inferred source composition for the Honolulu Volcanics, (Clague and Dalrymple, 1988, $F = 0.11$): 2.67 ppm La, 3.14 ppm Nd. Tick marks on partial melting trends are 0.1% melting increments. See Table 4 for details of melting models.

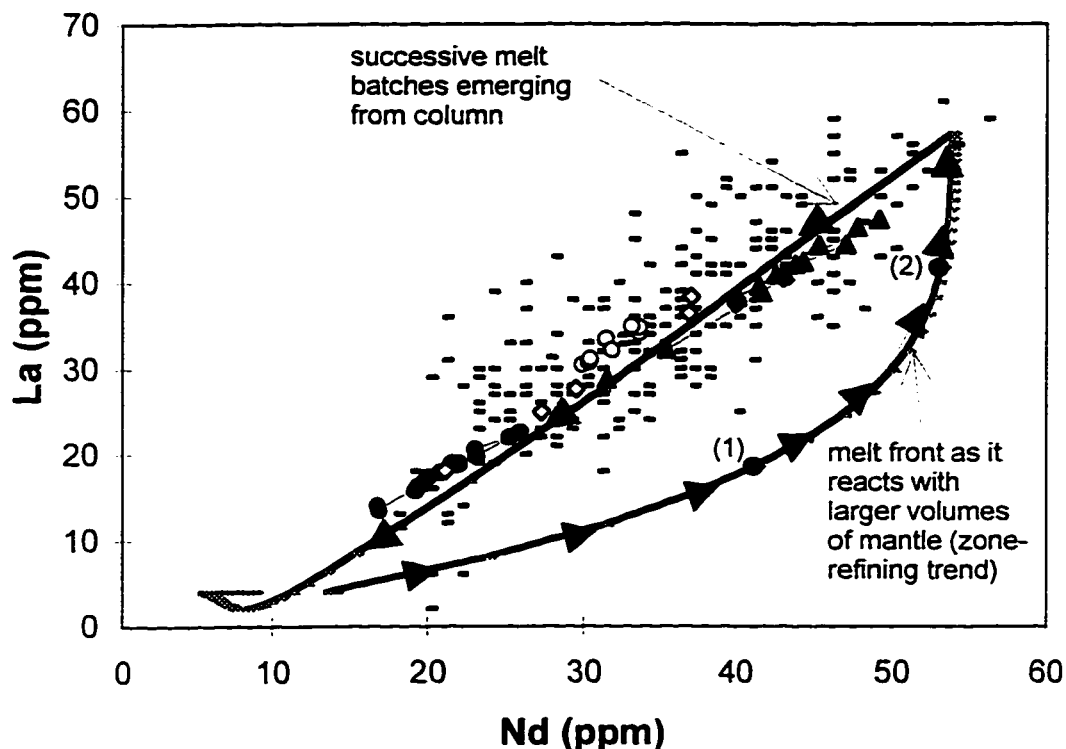


Figure 22. La and Nd concentrations of Koloa samples and predictions of reactive transport of 5% melt of depleted mantle through similar depleted mantle matrix

Matrix is assumed to react from lherzolite to pyroxenite as melt flows through and reacts with it. Symbols as in Figure 17 (modes and initial La and Nd concentrations in Table 4). As the melt front percolates into and reacts with progressively larger volumes of mantle, it follows a trend of increasing La and Nd, approaching the composition of an incipient partial melt of the matrix. Compositions of successive melts emerging from this reactive column then have decreasing, and highly correlated, La and Nd concentrations. No chromatographic effect is observed for these elements, because both are strongly partitioned into the matrix by the mineralogic reaction of lherzolite to pyroxenite in the matrix. This type of reactive transport generates a trend of compositions similar to the trend observed for the Koloa eruption sequences. If melts from different eruptions have reacted with different volumes of mantle (as suggested by their different isotopic compositions), then the trends of successive melt batches should begin at different points along the trend of melt front compositions (e.g., points 1 and 2, which represent hypothetical La and Nd concentrations of melts that have reacted and equilibrated with relatively small, and large, respectively, volumes of mantle matrix), which they do not. In contrast, La and Nd concentrations both within *and between* eruption sequences are highly linearly correlated in a very restricted region in this plot. This indicates that reactive melt transport, with or without mineralogic reaction, cannot accurately reproduce the La-Nd correlations of these lavas.

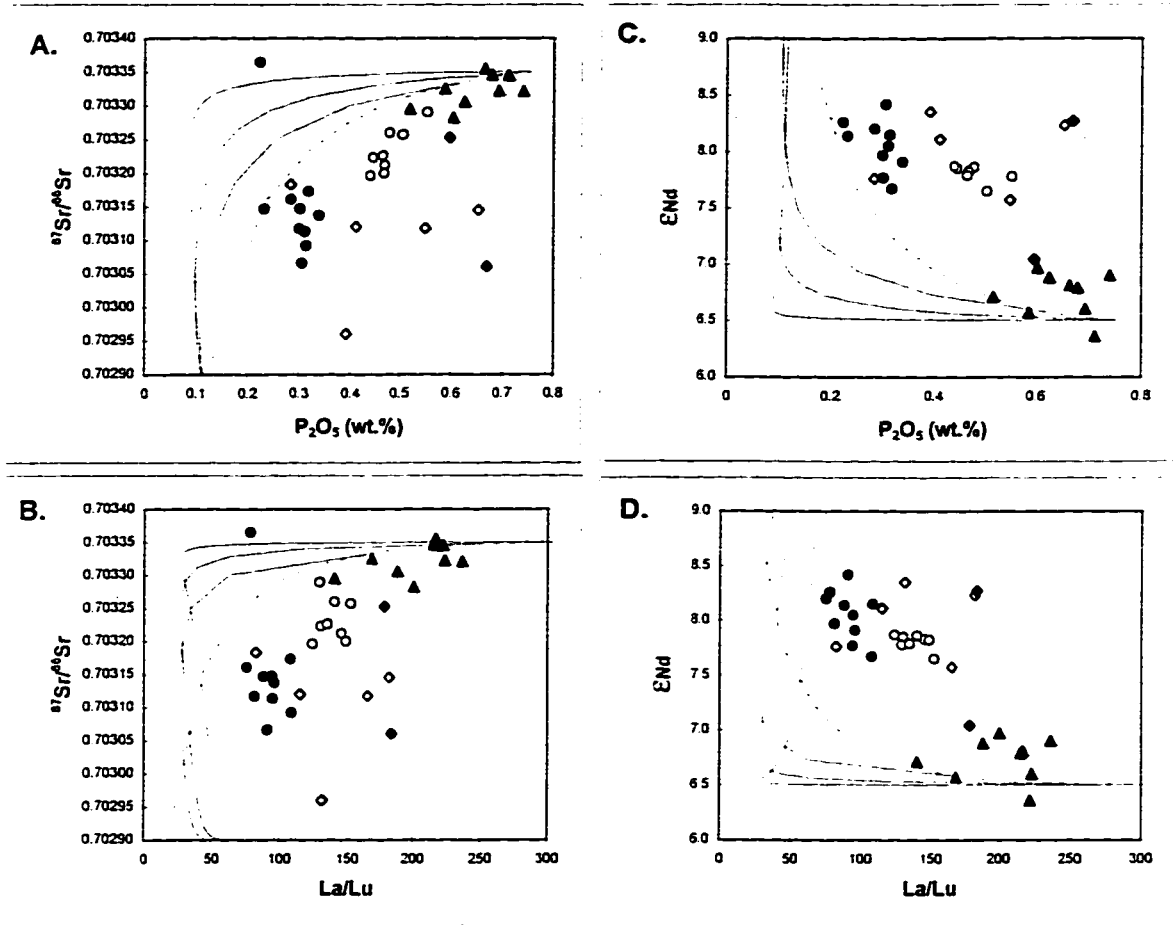


Figure 23. P_2O_5 and La/Lu versus $^{87}\text{Sr}/^{86}\text{Sr}$ and ϵ_{Nd} of samples with predictions of the reactive transport model.

Model uses the same initial melt and matrix compositions and parameters as in Figure 9 caption. Symbols as in Figure 17. Initial input melt has $^{87}\text{Sr}/^{86}\text{Sr}$ of 0.7029 and ϵ_{Nd} of +9.5, matrix has $^{87}\text{Sr}/^{86}\text{Sr}$ of 0.70335 and ϵ_{Nd} of +6.5. In each plot, dashed line is composition of melt front as it percolates through, and reacts with, progressively larger volumes of mantle, and solid lines are successive melt batches emerging from reactive column with varying lengths. **A.** P_2O_5 vs. $^{87}\text{Sr}/^{86}\text{Sr}$. **B.** La/Lu vs. $^{87}\text{Sr}/^{86}\text{Sr}$. **C.** P_2O_5 vs. ϵ_{Nd} . **D.** La/Lu vs. ϵ_{Nd} . The reactive transport model predicts strong decoupling between isotopic and trace element compositions in successive melt batch trends, due to the chromatographic effect. Because of the differing compatibility of P_2O_5 , Sr, La, Lu, and Nd, model trends of emerging melts do not show the excellent correlations between trace element and isotopic composition that the Koloa samples do. Thus the reactive transport model involving diffusive equilibration between melt and mantle (with or without mineralogic reaction) does not provide a satisfactory explanation for these trace element-isotopic correlations.

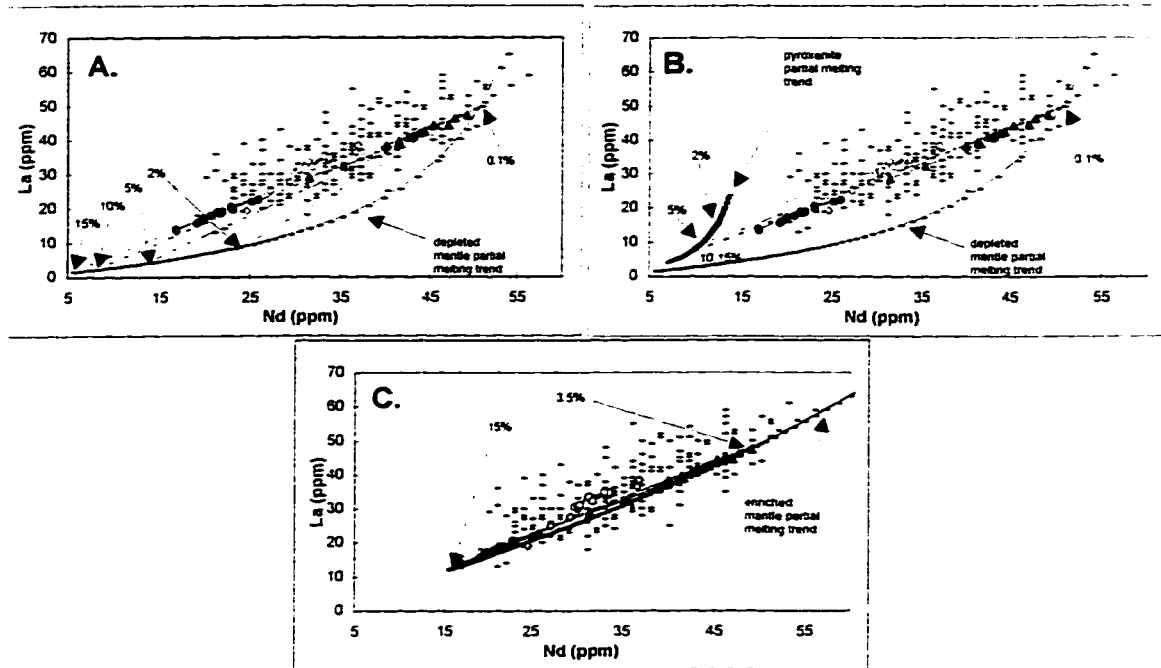


Figure 24. La and Nd concentrations of Koloa lavas with partial melting trends of depleted lherzolite, pyroxenite, and enriched lherzolite, and melt-mixing trends.

Symbols as in Figure 17, parameters, initial and endmember compositions in Table 4. **A.** Mixing between 0.1% lherzolite melt and larger-degree melts (2, 5, 10, and 15%) of lherzolite with the same incompatible element-depleted composition. **B.** Mixing between 0.1% lherzolite melt and larger-degree melts of pyroxenite with composition typical of Hawaiian pyroxenite xenoliths (Table 4). Mixing of low- and high-degree melts of typical depleted sources reproduce the linear correlation of these and other trace elements fairly well. While a 0.1% melt of typical depleted mantle with garnet lherzolite provides a reasonable choice for the low-degree melt endmember, there is little constraint on the initial La and Nd concentrations or mineralogy of high-degree melt endmember. For example, 5-15% melts of a pyroxenite source with a typical "pyroxenitic" (Frey, 1980; Hirschmann and Stolper, 1996) LREE-depleted pattern also has similar La-Nd concentrations as 6-12% melts of a lherzolitic source. **C.** Partial melting trend of LREE-enriched lherzolite (melt 1 source in Fig. 27), and mixing trend between 3.5% melt and 15% melt. It is impossible to distinguish from these data whether the melt mixing implied by the linear correlation of trace elements and trace element-isotopic correlations is produced by melting of mantle sources with LREE-enriched or LREE-depleted compositions.

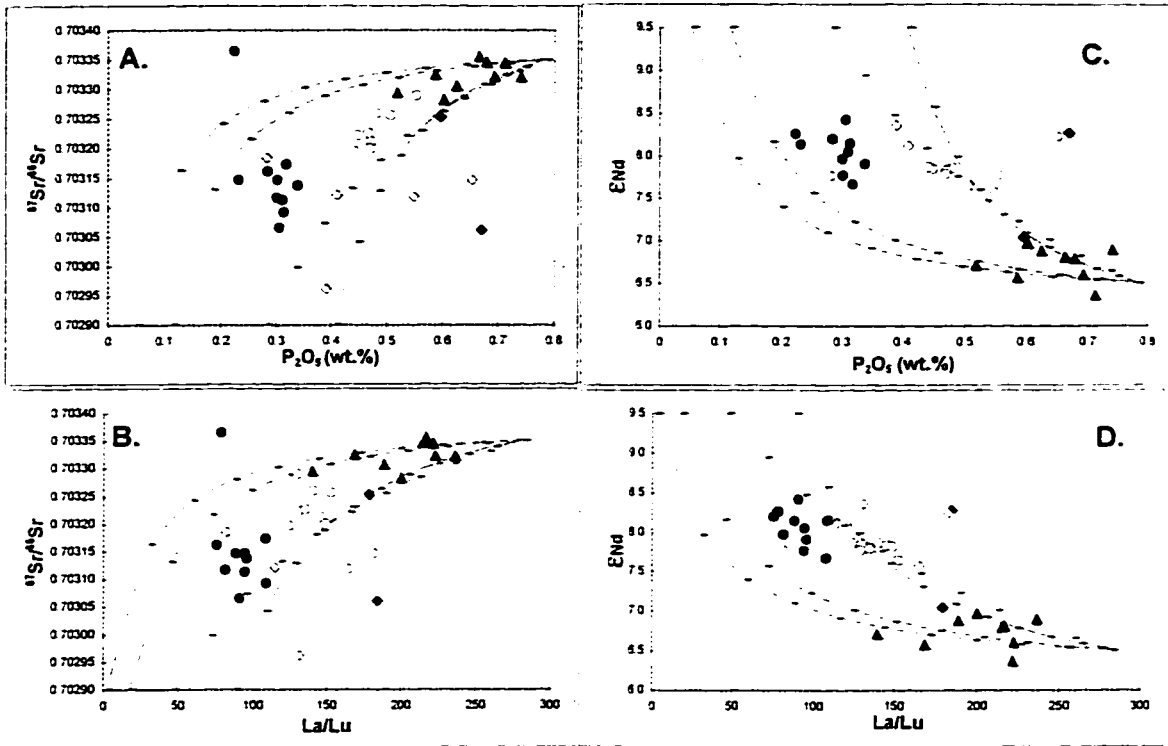


Figure 25. P_2O_5 and La/Lu versus $^{87}Sr/^{86}Sr$ and ϵ_{Nd} of samples with predictions of melt-mixing using melts derived from incompatible element-depleted mantle sources.

Symbols as in Fig. 17. Grey lines: mixtures of 0.1% depleted lherzolite melt with 2% (solid grey line) and 15% (dashed grey line) depleted lherzolite melt (see Table 4 for source compositions, distribution coefficients, and modes). Black lines: mixtures of 0.1% depleted lherzolite melt with 2% (solid black line) and 15% (dashed black line) melt of pyroxenite (Table 4). Tick marks are 10% mixing-proportion intervals. The high-degree melt endmember is assumed to have $^{87}Sr/^{86}Sr = 0.7029$, and $\epsilon_{Nd} = +9.5$, while the low-degree (0.1%) melt endmember is assumed to have $^{87}Sr/^{86}Sr = 0.70335$, and $\epsilon_{Nd} = +6.5$. Most of these data can be reproduced by assuming small variations in the degree of melting of the high-degree melt endmember.

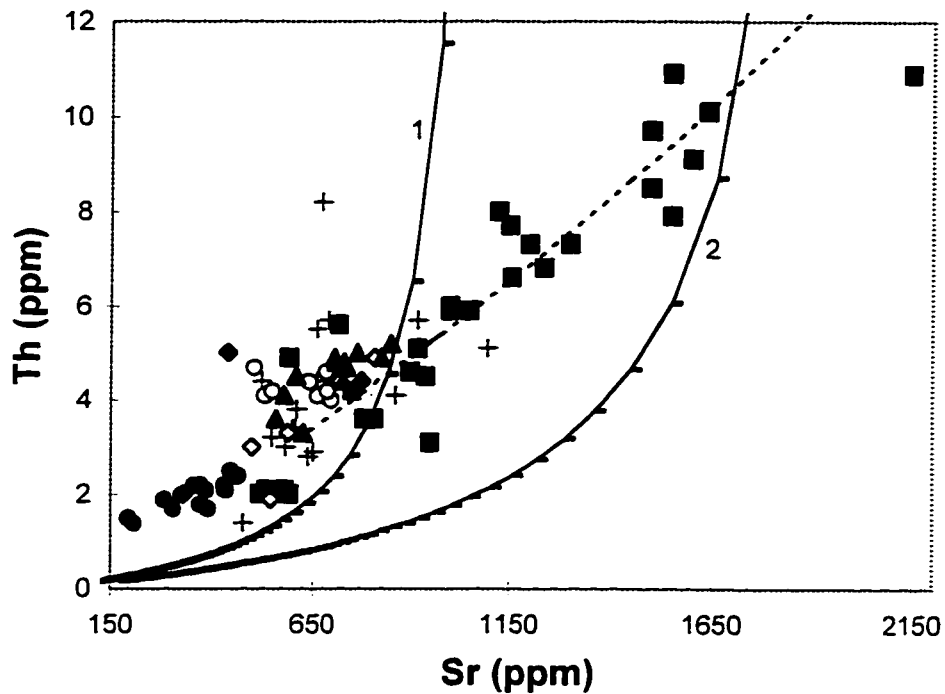


Figure 26. Th and Sr concentrations of lavas from the Koloa and Honolulu Volcanics.

Th and Sr concentrations (ppm) for Koloa samples from this study (symbols as in Figure 17) and from the literature (crosses, Maaløe et al., 1992; Clague and Dalrymple, 1988), as well as for samples from the Honolulu volcanics (black squares, Clague and Frey, 1982). Note the approximately linear correlation between and within Koloa and Honolulu volcanics samples. Th and Sr are highly, and moderately, incompatible elements, respectively, so explaining the overall correlation between Th and Sr concentrations in these samples with a single source partial melting model requires a source strongly enriched in incompatible elements (dashed line is non-modal batch partial melting trend for lherzolite source with 0.4 ppm Th and 80 ppm Sr—about 10 and 7.3 times chondrites, respectively) and a very large range in extent of partial melting (from about 3.5 to 35%). In contrast, mixing of low- and high-degree melts of depleted mantle sources explain the range of Koloa and Honolulu volcanics samples without invoking recent source metasomatism. The black lines are non-modal batch partial melting trends of lherzolite with 1) Th = 0.015 ppm and Sr = 12 ppm, and 2) Th = 0.02 ppm and Sr = 22 ppm. Bulk D for Th is assumed to be 0.0003 (Sims et al., 1995); using a Th bulk D of 0.003 instead does not change the results significantly.

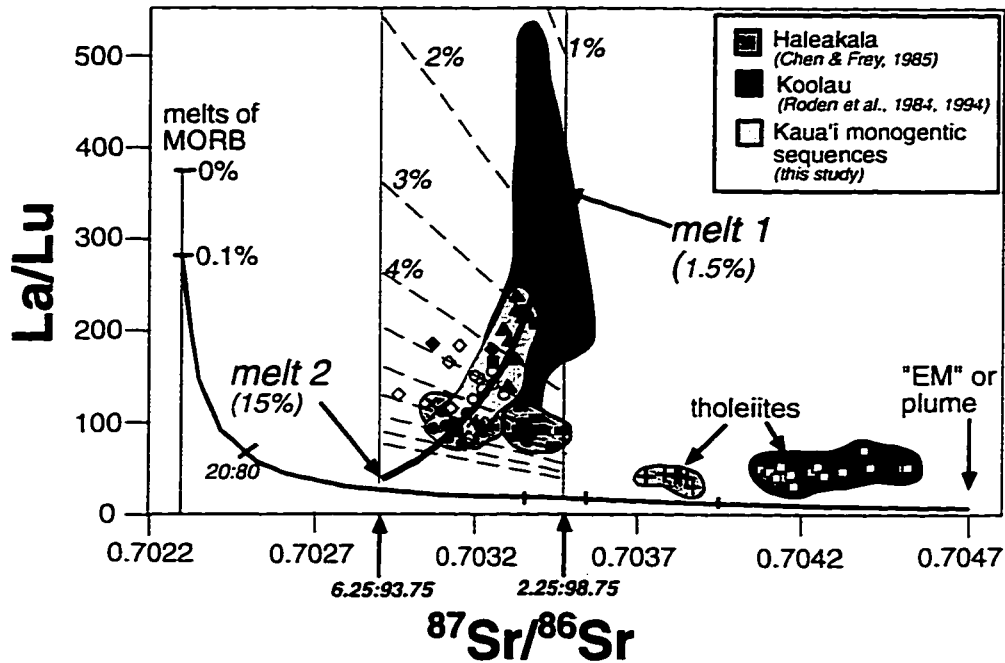


Figure 27. La/Lu versus $^{87}\text{Sr}/^{86}\text{Sr}$ of Koloa lavas and post-erosional, post-shield alkalic, and tholeiitic lavas from Haleakala and Koolau volcanoes.

La/Lu versus $^{87}\text{Sr}/^{86}\text{Sr}$ of samples in this study (symbols as in Fig. 17), and post-erosional, post-shield alkalic, and tholeiitic lavas from Haleakala (Chen and Frey, 1985) and Koolau (Roden et al., 1984, 1994) volcanoes. X's are post-erosional alkalic basalts of Haleakala (Hana series), dashes are post-shield cap alkalic basalts of Haleakala (Kula series), and + 's are tholeiitic basalts of Haleakala (Honomanu series). White squares are tholeiitic basalts (Koolau series), and black squares are post-erosional magmas (Honolulu volcanics) of Koolau volcano. Overall, from tholeiitic basalts to post-erosional magmas, there is an inverse correlation between La/Lu and $^{87}\text{Sr}/^{86}\text{Sr}$. However, variations *within* post-erosional magmas from these three volcanoes however, show the opposite trend between $^{87}\text{Sr}/^{86}\text{Sr}$ of approximately 0.70290 and 0.70347, which are inferred to be the isotopic compositions of melt 2 and melt 1, respectively. Also shown are the MORB and EM (plume) model sources of Chen and Frey (1983, 1985).

Fig. 27 (continued). Assuming typical depleted REE concentrations for the MORB source (McKenzie and O'Nions, 1991: La = 0.206 ppm, Lu = 0.054 ppm), and nonmodal batch melting (Table 4), melting of the MORB source generates the constant isotopic (vertical) partial melting trend shown on the left side of the plot. Tick marks are 0.1% melting increments. Mixing of a 0.1% MORB melt with solid EM mantle (using EM concentrations from Chen and Frey, 1985, and Lu = 0.1 ppm) generates the hyperbolic mixing trend. Tick marks on the 0.1% MORB-solid EM mixing trend are 0.25% intervals of 0.1% MORB added to solid EM, until 20%, then tick marks are every 10% mixing. Solid sources with the appropriate $^{87}\text{Sr}/^{86}\text{Sr}$ and La/Lu for melt 1 and melt 2 sources are generated by mixing the EM source with 2.25% and 6.25%, respectively of this 0.1% MORB melt. The melt 1 source has $^{87}\text{Sr}/^{86}\text{Sr} = 0.70347$, La = 1.81, and Lu = 0.08; melt 2 source has $^{87}\text{Sr}/^{86}\text{Sr} = 0.70290$, La = 3.77, and Lu = 0.09 (Table 4). 1% contours of non-modal batch melting increments of these metasomatized sources are denoted by the dashed lines. Mixing between a 15% melt of the melt 2 source and a 1.5% melt of the melt 1 source explain most of the post-erosional magmas from Kaua'i, Haleakala and Koolau volcanoes. Among samples from this study, alkalic basalts from the HTZ drillhole require mixing melt 2 with 10-25% melt 1, Lae O Kilauea samples require mixing melt 2 with 25-40% melt 1, and nephelinites from the HTZ drillhole require mixing melt 2 with 35-60% melt 1. It is appealing to postulate that the reason the melt 2 source melts to a larger degree than the melt 1 source (by a factor of 10) is because it mixed with a larger proportion of low-degree MORB melt (e.g., it was more extensively metasomatized by a factor of 2.7).

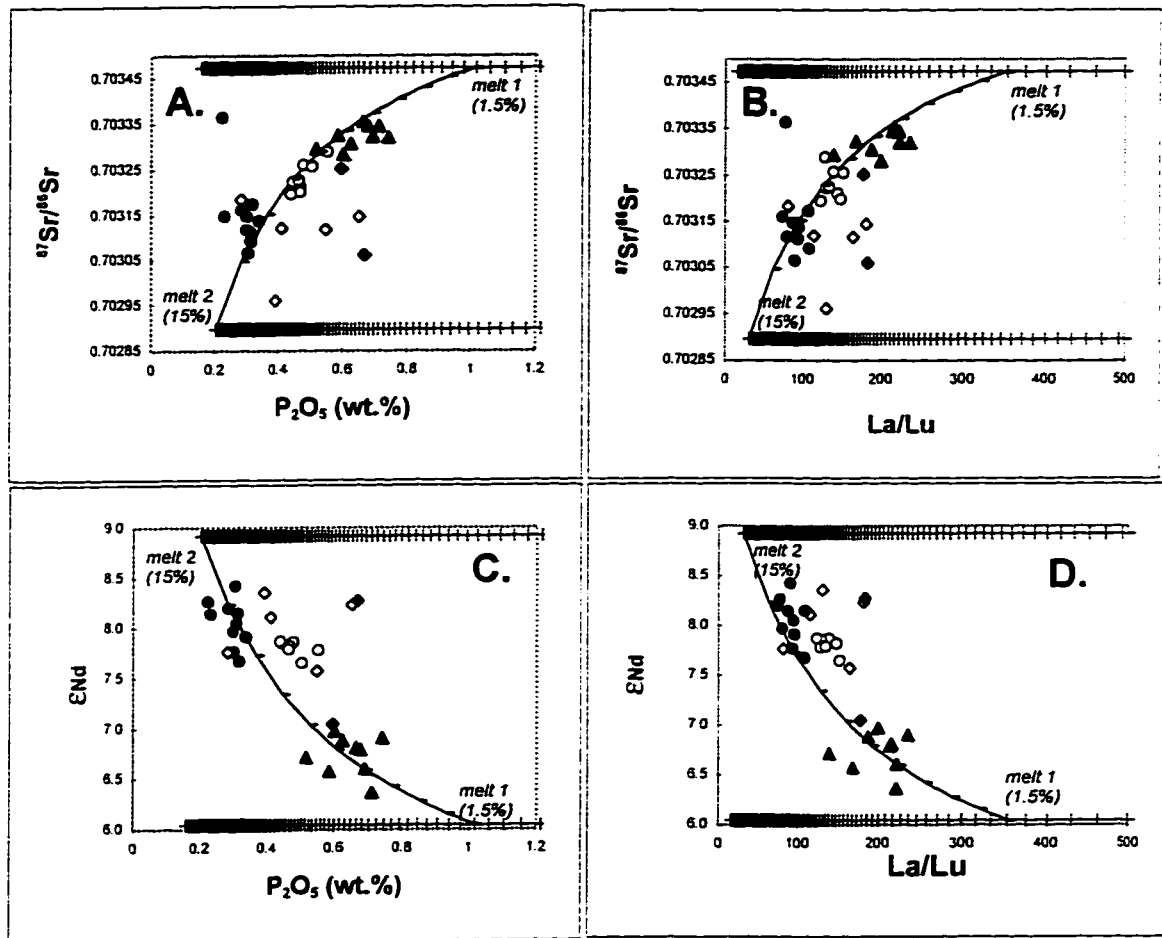


Figure 28. $^{87}\text{Sr}/^{86}\text{Sr}$ and ϵ_{Nd} of Koloa magmas versus P_2O_5 (wt.%) and La/Lu, with melt-mixing trends, enriched mantle sources.

$^{87}\text{Sr}/^{86}\text{Sr}$ and ϵ_{Nd} of Koloa magmas versus P_2O_5 (wt.%) and La/Lu (symbols as in Fig. 17). Horizontal lines are non-modal batch partial melting trends (Table 4) of melt 1 and melt 2 sources, where each source is produced by mixing 2.25% and 6.25%, respectively, of 0.1% MORB melt with solid EM mantle of Chen and Frey (1983, 1985). Mixing between a 1.5% melt of the melt 1 source, and a 15% melt of the melt 2 source, reproduce the Koloa magma compositions quite well. Tick marks on melting trends are 0.1% melting increments; tick marks on mixing trends are 10% mixing increments. La, Lu, Nd, P_2O_5 , and Sr concentrations and Sr- and Nd-isotope compositions of mixing endmembers are shown in Table 4.

CHAPTER 3: STRATIGRAPHY AND GEOCHEMISTRY OF VOLCANIC AND DEBRIS-FLOW DEPOSITS OF THE LIHUE BASIN AND EASTERN KAUA'I, HAWAII

ABSTRACT OF CHAPTER 3

The Lihue basin is a large (~110 km²) topographic depression bounded by steep cliffs and partly filled by late-stage post-erosional volcanics on the eastern side of the Hawaiian island of Kaua'i. While generally ascribed to some type of structural collapse, the origin of the basin and its subsurface geology are poorly-understood. New petrographic, geochemical, and isotopic analyses of samples from drillholes within the basin and from adjacent outcrops in eastern Kaua'i document important features of the geologic history and late-stage alkalic magmatism of the island. A thick (>300 m) sequence of post-erosional Koloa Volcanics within the Lihue basin shows systematic, basin-wide geochemical trends that indicate a gradual decrease in extent of partial melting of mantle sources with time. Beneath the post-erosional lavas in the basin, hawaiites, mugearites, and differentiated alkalic basalts typical of post-shield alkalic volcanics overlie older shield-stage tholeiitic lavas of the Napali member, documenting a more voluminous and widespread post-shield alkalic stage than inferred from the two hawaiites and one mugearite flow previously identified in the western part of the island. The presence of these lavas at the bottom of the basin suggest that the Lihue basin formed by structural collapse, not fluvial erosion. A large (~5 km³) matrix-supported breccia, interpreted as deposits of one or more debris flows, is also observed within the post-erosional volcanic sequence throughout the basin, and in surficial exposures on its western and northern margins. This matrix of the breccia is tholeiitic, with isotopic compositions similar to tholeiites from the east side of Kaua'i, and distinct from those on the west side. The clasts within the breccia however, are dominantly hawaiite and alkali gabbro. The great

thickness (at least 213 m) of the breccia on the western side of the basin indicates a source region in the steep cliffs and highlands of the island's central massif. This area of the island must contain magmatic products of an extensive post-shield alkalic stage, including hawaiite flows and one or more large intrusive bodies or calderas of alkali gabbro.

INTRODUCTION TO CHAPTER 3

The Lihue basin of eastern Kaua'i is a large (~ 110 km²) topographic depression enclosed by steep-walled cliffs and open to the east (Figs. 29, 30). Such U-shaped basins are common features of ocean islands, including Hawai'i, Réunion, and the Canary Islands, and have been interpreted as both remnant calderas (Stearns & Vaksvik, 1935; Marti et al., 1994) and down-dropped blocks resulting from giant landslides or slumps (Presley et al., in press; Gillot et al., 1994; Carracedo, 1994, 1996). The origin of the Lihue basin is particularly enigmatic because of the enormous topographic relief (as much as 1 km) on its western margin and the presence of a positive Bouguer gravity anomaly (typically observed at shield volcano summit calderas) in the northwest part of the basin (Krivoy et al., 1965), while the island's central summit caldera is centered about 20 km northwest of the middle of the basin (MacDonald et al., 1960). Here I present stratigraphic and geochemical results from sections and samples from the margins of the basin and from deep (>300 m) drillholes in the central and southern part of the basin that reveal several important features of the Lihue basin and the growth and evolution of Kaua'i, including the distribution and petrologic evolution of its post-shield and post-erosional alkalic volcanics.

GEOLOGY OF KAUA'I AND THE LIHUE BASIN

Kaua'i is the second oldest and most northwesterly of the main Hawai'ian islands, and is generally interpreted as the eroded remnants of a single large shield volcano (Dana 1849:

Hinds, 1930; MacDonald et al., 1960) whose main shield-building stage lasted from before about 5.1 Ma to about 4.3 Ma (McDougall, 1979). The lavas that compose the island have been divided into two main stratigraphic groups: the older Waimea Canyon Basalt comprising tholeiitic and a few rare hawaiitic and mugearitic lava flows, and the post-erosional, or rejuvenated-stage Koloa Volcanics, comprising highly alkalic, primitive lavas and related volcanics (Fig. 29) (MacDonald et al., 1960; Clague & Dalrymple, 1988). The older Waimea Canyon Basalt is further subdivided into four members, the oldest and most widespread of which is the tholeiitic lavas of the Napali member. The Ha'upu, Makaweli, and Olokele members are primarily younger lavas that apparently ponded within enclosed or partially enclosed structural features. The thick, flat-lying tholeiitic lava flows of the Ha'upu member are restricted to a small (~1.6 km²), ovoid, fault-bounded structure in the southeast corner of the island that is generally interpreted as a flank caldera or large pit crater. The Makaweli member is predominantly tholeiitic lavas, with two capping flows of hawaiite and mugearite (Clague & Dalrymple, 1988), all of which apparently ponded in a graben-like depression in the southern part of the island. The Olokele member is also dominantly tholeiitic lavas, with one recognized hawaiite flow, and comprises a thick section of flat-lying, apparently ponded lavas in the central part of the island. The inferred structural feature that bounds the Olokele member is interpreted as a lava-filled summit caldera (Clague & Dalrymple, 1988; MacDonald et al., 1960). The three hawaiite and mugearite lavas in the Olokele and Makaweli members represent the known extent of the post-shield alkalic stage, and have ages of about 3.9 Ma (Clague & Dalrymple, 1988). The post-erosional stage Koloa Volcanics represent the latest volcanism on Kaua'i, and consist of alkalic basalt, basanite, nephelinite, and melilitite lavas and tuffs erupted primarily in the the central and eastern parts of the island (MacDonald et al., 1960; Clague & Dalrymple, 1988; Maaløe et al., 1992). Radiometric ages of Koloa lavas range from about 0.5 to 3.6 Ma, with lavas from the eastern part of the island less than 1.5 Ma (Clague & Dalrymple, 1988).

Kaua'i is distinct from other Hawai'ian shield volcanoes in the abundance and scale of documented and inferred large faults and structural-topographic features. The caldera inferred from the distribution of thick, flat-lying flows of the Olokele member is more than 21 km in diameter, which would make it by far the largest in the Hawai'ian islands. A series of north-south trending normal faults bisect the western part of the island, delineating both the Makaweli graben in the south, and a scarp, at least 800 m high, against which younger flows ponded in the northwestern part of the island (the Kalalau fault, MacDonald et al., 1960). GLORIA side-scan sonar imagery indicates the presence of at least two large debris fields on the north, south, and possibly east sides of the island, resulting from giant landslides (Moore et al., 1994). All of these structural-topographic (and bathymetric) features suggest a geologic history of the island that may be more complicated than previously recognized. Recent work has established that Sr-, Nd-, and Pb-isotope compositions of tholeiites on the east and west sides of Kaua'i are distinct (Holcomb et al., 1995; Holcomb et al., in press), and has been used in conjunction with structural and paleomagnetic arguments to suggest the presence of two distinct shield volcanoes on the island (Holcomb et al., 1995; Holcomb et al., in press).

The Lihue basin is a broad, low-lying area of approximately 110 km² on the eastern side of Kaua'i with an average elevation of approximately 100-120 m above sea level (Figs. 29, 30). It is covered by lava flows of the Koloa Volcanics and bounded by steep cliffs of the Waimea Canyon Basalt. At the western margin of the basin steep cliffs of the central massif of the island rise abruptly from the basin floor to nearly 1600 m above sea level, supporting the highest points on the island. The northern margin of the basin is bounded by the Makaleha mountains, which are topped by a broad, flat plateau about 1000 m above sea level that has been interpreted as an erosive remnant of an ancient shield surface (MacDonald et al., 1960). The south side of the basin is bounded by tholeiitic lavas of the Ha'upu ridge, including the Ha'upu caldera, which is covered by alluvium on the north side, towards the Lihue basin. The eastern boundary of the Lihue basin is less clear. Some workers place the edge of the basin at the base of two small ridges (Kalepa

and Nonou ridges, at 215 and 320 m above sea level) near the eastern edge of the island. But these ridges are discontinuous to the north and south, and the Lihue basin could also be interpreted as open to the sea on its eastern side. The southern ridge (Kalepa) has a distinctly curvilinear north-south trend, concave to the west, possibly suggestive of caldera boundary morphology. Both the Kalepa and Nonou ridges comprise tholeiitic lava flows typical of the Napali member, but these flows have unusual orientations, dipping as steeply as 16 degrees to the east. Orientations of dikes within these ridges are also atypical, dipping shallowly into the center of the basin in contrast to the more common near-vertical dikes of Hawai'ian shields (MacDonald et al., 1960).

The Lihue basin is covered by lava flows of the Koloa Volcanics, some of which probably originated from the Kilohana shield, a large vent in the central-southern part of the basin that reaches an elevation of 320 m above sea level, some 220 m above the surrounding plains to the north, east, and south. In most places on the west and north sides of the Lihue basin, tholeiitic flows of the Napali member and alkalic lavas of the Koloa Volcanics are separated by a thick layer of massive, unsorted breccia. MacDonald et al. (1960) defined any breccia or conglomerate within or below the Koloa Volcanics as the Palikea formation; Langenheim & Clague (1987) suggested the term Palikea Breccia member of the Koloa Volcanics for the breccia and other sediments within and below Koloa flows. The Palikea breccia on the west margin of the Lihue basin is an unsorted and matrix-supported breccia and contains a variety of clast sizes and lithologies (discussed below). The type section of the breccia facies of the Palikea formation is the Palikea ridge, near the western margin of the Lihue basin, and is at least 213 m thick. The Palikea formation on the western margin of the Lihue basin is distinct from most other Palikea exposures on Kaua'i, which are most commonly clast-supported conglomerates less than 40 m thick.

SAMPLE LOCATIONS & ANALYSES

To supplement detailed geochemical and isotopic analyses from a single drillhole in the Lihue basin (the Hanamaulu, or HTZ drillhole, Chapter 2), I collected and analyzed 46 samples from four other drillholes in the Lihue basin for major-element compositions (Table 5). These are the Northwest Kilohana (NWK), Northeast Kilohana (NEK), Puakukui Reservoir (PKR), and South Wailua (SW) drillholes (Fig. 29). Drillhole samples taken for major-element analysis consist of cuttings averaging 1-3 cm in diameter, from splits of samples recovered from drilling every 1.5 m. Only the cuttings with the freshest appearance and representative of the macroscopically dominant lithology within each split were selected for analysis. Major- and trace-element and isotopic data from the HTZ drillhole (Chapter 2) indicate very little mixing of samples between splits from different levels in the drillhole. New analyses of major element compositions of forty-six Lihue basin drillhole samples are presented in Table 5, in addition to data from 39 samples from the HTZ drillhole (Chapter 2).

I also collected and analyzed three samples from the Palikea formation exposed at Palikea ridge, on the west side of the basin (Table 5). Palikea ridge breccia analyses include one sample of matrix and two samples of the dominant and distinct types of clasts within the breccia.

Sr- and Nd-isotope compositions of samples from the HTZ drillhole (Chapter 2) and from subaerial samples collected in various parts of the island were also determined and have been included to aid the interpretation of the provenance of Palikea breccia samples (Table 6).

The lithologic nomenclature used here generally follows that used by Clague & Dalrymple (1988) in their study of Kauaī volcanics. Where I distinguish among lithologies of the Koloa Volcanics I refer to basalt containing modal plagioclase but no nepheline as alkalic basalt, basalt containing modal nepheline and plagioclase as basanite.

and basalt containing nepheline but no plagioclase or melilite as nephelinite. A few of the post-shield alkalic stage rocks are hawaiite or mugearite, similar to compositions found by Clague & Dalrymple (1988), the hawaiites and mugearites having total alkalis greater than 5.7 wt.% and 6.9 wt.%, respectively. Post-shield stage alkalic basalts are distinguished from Koloa alkalic basalts by significantly lower MgO (< 8 wt.%), and from hawaiites by total alkalis less than 5.7 wt.%. Samples with alkalic basalt compositions and gabbroic textures are referred to as alkali gabbros.

RESULTS

PALIKEA RIDGE

The Palikea formation at Palikea ridge is a >213 m thick massive, unsorted matrix-supported breccia, with clast sizes ranging from less 1 cm to more than 3 m in diameter. Large clasts (> 0.5 m) are typically unaltered, hard, and fine-grained, with a trachytic texture (Fig. 31). They have a large modal proportion (>75%) of elongate, highly lined lathe-shaped plagioclase crystals and rare microcrysts of pyroxene and opaque phases. Smaller clasts (< 0.5 m) typically have either porphyritic or fine- to medium-grained gabbroic textures (Fig. 31). The porphyritic clasts contain abundant large plagioclase crystals in a fine-grained matrix of plagioclase, pyroxene, and opaque phases. Fine- to medium-grained gabbroic clasts contain plagioclase, pyroxene, opaque phases, and rare olivine crystals, with very little or no fine-grained matrix. Many have diktytaxitic textures, or an open miarolytic structure, as described by MacDonald et al. (1960, p. 101). Major element compositions of the Palikea ridge breccia indicate that the matrix has a composition close to that of tholeiitic basalt, while a fine-grained clast has a hawaiitic composition, and a medium-grained clast with a gabbroic texture has the composition of a (low-MgO) alkali basalt (Fig. 32).

LIHUE BASIN DRILLHOLE SAMPLES

Three main groups of samples are recognized within the Lihue basin drillholes based on major-element chemistry (Fig. 32): 1) Koloa lavas, 2) tholeiites and altered lithologies within a thick breccia layer, and 3) tholeiites, hawaiites, mugearites, and alkali basalt of the Waimea Canyon Basalt, near the bottom of three of the drillholes.

Koloa Volcanics

Most Lihue basin samples have compositions typical of the post-erosional lavas of the Koloa Volcanics (MacDonald et al., 1960; Feigenson, 1984; Clague & Dalrymple, 1988; Maaløe et al., 1992), with low SiO_2 and high MgO , P_2O_5 , and alkalis (Fig. 32). Within the Koloa lavas there appears to be an overall increase in concentrations of TiO_2 and P_2O_5 with stratigraphic height in all of the drillholes (Fig. 33). Other major elements show no trends.

Breccia layer

Between approximately 55 and 120 m depth, all drillholes contain an approximately 25-70 m thick layer of matrix-supported breccia with clasts of both fine-grained and gabbroic textures. Approximately 50% of the clasts have a fine- to medium-grained gabbroic texture. Analyzed breccia samples from the drillholes were not separated according to clast or matrix lithology and compositions probably represent average compositions of the breccia layer, containing matrix and a variety of clast lithologies. Compositions of samples from the breccia layer are quite different from those of Koloa lava samples. Many of the bulk breccia samples have compositions very similar to those of tholeiites (Fig. 32) from Kaua'i (MacDonald & Katsura, 1964). Some of the more weathered samples (especially the breccia samples in the SW and PKR drillholes) have unusual compositions with high Fe_2O_3 , TiO_2 , and P_2O_5 , and low CaO and SiO_2 . These compositions are unlike typical Hawaiian lavas, and probably reflect extensive alteration, as suggested by their deep-red color and the presence of significant amounts of clay in

some samples. Well-logs from macroscopic lithologic descriptions indicate that these breccia layers extend from 62.5-134.1 m below the ground surface in the NEK drillhole, 56.4-94.5 m in PKR, 64.0-111.2 m in HTZ, 53.3-77.7 m in SW, and 70.1-99.1 m in NWK. When integrated into a generalized composite stratigraphy for the basin (Fig. 34), these intervals appear to correlate with surface exposures of the Palikea breccia in the Waiahi Stream and at Palikea ridge, both in the western margin of the basin. Isotopic compositions of samples from this interval in the HTZ drillhole are similar to isotopic compositions of tholeiites from eastern Kaua'i and distinct from those of tholeiites from western Kaua'i (Table 6, Fig. 35).

Waimea Canyon Basalt

Sample at or near the bottom of three drillholes (PKR, NWK, and SW) have compositions very similar to subaerial tholeiite, hawaiiite, mugearite on Kaua'i (Table 5, Fig. 32). Apparently these drillholes penetrated through the Koloa Volcanics and into the underlying Waimea Canyon Basalt, consisting of tholeiitic and alkalic lavas of the late tholeiitic shield-building and post-shield alkalic stages of volcanism.

Subaerial Napali member lavas

Isotopic compositions of subaerial samples from east Kaua'i (Puu Kee and Nonou ridge) have higher $^{87}\text{Sr}/^{86}\text{Sr}$ and lower ϵ_{Nd} than samples from the northwestern (Haena dry cave) and north-central (Hanalei) parts of the island (Table 6, Fig. 35), supporting earlier isotopic work suggesting that tholeiites from the eastern side of the island are isotopically distinct from those on the west side (Holcomb et al., 1995; Holcomb et al., in press). A single sample of tholeiitic basalt from near the base of the Makaweli member, in Waimea Canyon (Table 6, Fig. 35) has an isotopic composition intermediate between those of the east and west sides of the island.

DISCUSSION

The wide variety of lithologies recovered from the Lihue basin drillholes and adjacent areas provides new stratigraphic and petrologic constraints on the origin of the basin and the geologic history of Kauaī. The following discussion focuses primarily on three aspects: 1) the geochemical compositions of Koloa Volcanics in the basin, 2) the stratigraphic relations of tholeiites and differentiated alkalic lavas (hawaiites, mugearites and alkali basalts) found deep in three of the drillholes, and 3) the thick layer of breccia found in all the drillholes and exposed on the western margin of the basin. The geologic implications of the structure and depth of the basin and the marine layers found in some of the drillholes will be discussed in a forthcoming paper.

STRATIGRAPHIC-GEOCHEMICAL TRENDS IN THE KOLOA VOLCANICS

Previous studies have emphasized the absence of spatial or temporal patterns to lithologies of post-erosional volcanism on Hawai'ian volcanoes (Clague & Frey, 1982; Clague & Dalrymple, 1988). In contrast, a detailed study of the HTZ drillhole documents a stratigraphic trend from alkali basalts to basanites, to nephelinites, from the older to younger lavas (Fig. 36) (Chapter 2). This lithologic sequence is accompanied by an overall increase in concentrations of incompatible elements such as P_2O_5 and TiO_2 throughout the sequence (Fig. 33). These stratigraphic trends are consistent with progressively decreasing extents of melting of mantle sources during formation of Koloa lavas that filled the Lihue basin. This trend exists not only in Koloa lavas of the HTZ drillhole, but for all of the drillholes that contain Koloa lavas (Fig. 33). Clague & Dalrymple (1988) found no correlations between age and lithology within the Koloa Volcanics elsewhere on Kauaī, suggesting that the stratigraphic-geochemical correlation observed in the Lihue basin may be restricted to this region of the island.

WAIMEA CANYON BASALT LAVAS NEAR THE BOTTOM OF THE BASIN

Recovery of tholeiite, hawaiite, mugearite, and low-MgO alkalic basalt lavas from the lower parts of the NWK, PKR, and SW drillholes (Table 5, Fig. 34) indicates that these drillholes penetrated through the Koloa Volcanics and into the underlying Waimea Canyon Basalt. The deepest lavas from the SW and PKR drillholes are tholeiitic, similar in composition to subaerial Napali member lavas (Table 5, Fig. 32). Flows with compositions similar to subaerial hawaiites and mugearites of the Makaweli and Olokele members overlie these tholeiites in the PKR drillhole (and are the deepest lavas recovered in the NWK drillhole). This is consistent with the subaerial stratigraphy of Waimea Canyon Basalt, in which hawaiitic and mugearitic lavas overlie tholeiites in the Makaweli and Olokele members. These observations suggest that Waimea Canyon Basalt flows in the Lihue basin lie some 200 m below sea level in the vicinity of the PKR drillhole.

The observed stratigraphy of samples with tholeiitic composition below Koloa lavas and above hawaiitic lava in the lower part of the NWK drillhole (Fig. 34) is unexpected, and has at least two possible explanations. First, these tholeiitic samples could be lava flows in a section of intercalated alkalic and tholeiitic lavas of a post-shield volcanic stage. Other Hawaiïan shields often erupt both tholeiitic and alkalic magmas during their post-shield, or alkalic-cap stages of growth (Chen & Frey, 1985; Presley et al., in press). Most of the tholeiitic samples recovered from the NWK drillhole are relatively fresh and do not appear, from macroscopic inspection, to be reworked or transported fragments within a breccia or talus pile, consistent with their being in-place lava flows. Other drillholes in the Lihue basin however, do not contain sections of intercalated tholeiitic and (post-shield, non-Koloa) alkalic lavas. The second possibility is that these tholeiitic samples represent a very thick layer of breccia or talus accumulated at the margin of the basin, and capped by Koloa lavas. The proximity of this drillhole to the steep cliffs on the western margin of the basin would be consistent with thick talus accumulations in this part of the basin.

The presence of hawaiitic and mugearitic lavas deep in the Lihue basin provides an important constraint on the origin of the basin, which has been attributed to either erosion by fluvial processes or structural collapse (MacDonald et al., 1960). Nearly flat-lying stratified rocks are present in the steep cliffs up to 1200 m above and to the west of the Lihue basin. If formed by erosion, removal of over one kilometer of vertical relief from the top of the shield would be required to form the Lihue basin. Given typical eruption and growth rates for Hawai'ian shield volcanoes (Bargar & Jackson, 1974; Shaw et al., 1980), it is unlikely that erosion rates could exceed lava accumulation rates to generate 1 km of relief during shield-building. This much erosion must have occurred after the shield-building tholeiitic and post-shield alkalic stages of volcanism when eruption rates were much lower. The presence of hawaiitic post-shield alkalic lavas in the base of the Lihue basin indicates that if fluvial erosion did remove one kilometer of rocks from the top of the shield, then the post-shield alkalic lavas were greater than one kilometer thick in this area. This is unlikely given the thicknesses of post-shield alkalic sequences on other Hawai'ian volcanoes (e.g., West & Leeman, 1994), as well as the thin cap of hawaiitic flows in other areas of Kaua'i (a maximum of 3 flows). It would also imply that erosion coincidentally removed all but a few meters to tens of meters of post-shield alkalic hawaiitic lavas now found in the bottom of the Lihue basin. Therefore the presence of hawaiites overlying tholeiites near the base of drillholes in the Lihue basin indicates that the basin formed by structural collapse, regardless of whether the hawaiites were erupted prior to, or following, collapse.

Provenance of the breccia layer

The presence of a 25-70 m thick breccia between about 55-120 m below ground-surface in each drillhole indicates that the breccia is laterally continuous throughout at least the southern and central parts of the Lihue basin. Recovered samples of the breccia are matrix-supported and contain clasts with both fine-grained and gabbroic textures. Although many of the breccia samples recovered from the drillholes are quite altered, and

drillhole sampling did not permit analyses of individual clasts, compositions of the least altered average (bulk) breccia samples are similar to those of subaerial tholeiites. Isotopic compositions of the least-altered samples are similar to those of tholeiites of east Kauaī. The breccia layer in the Lihue basin appears to be correlative between drillholes based on consistent dip and thickness, and also correlative with surface exposures of a thick breccia layer found along the western margin of the basin, most notably in the Waiahi river gorge and Palikea ridge (Figs. 29, 34). The Palikea ridge breccia is also matrix supported and contains both fine-grained hawaiite clasts and fine- to medium-grained alkali gabbros, while the matrix is tholeiitic. The petrographic and compositional similarities between the drillhole breccia layer and the Palikea ridge breccia, as well as the apparent stratigraphic correlation between the two (Fig. 34), are strong evidence that they are the same unit and that it is continuous beneath the Lihue basin.

The massive, unsorted character and great thickness of the breccia at the Palikea ridge, the matrix-supported texture of the breccia both at Palikea ridge and in the drillholes throughout the basin, the lateral continuity of the breccia throughout the basin, and the major-element and isotopic composition of both the matrix and clasts within the breccia, indicate that this unit represents one or more debris flows derived from the steep cliffs and highlands west of the Lihue basin. Assuming that the debris flows covered the entire Lihue basin (about 110 km² if the Kalepa and Nonou ridges form the eastern boundary), and an average thickness of 42 m (from the average thickness in the drillholes and neglecting the Palikea ridge section of at least 213 m), then the debris layer would have an approximate volume of 4.6 km³. Assuming it covered only the area delimited by the drillholes, about one-third to one-half of the basin, the estimated volume would be 0.9 to 2.3 km³. If the deposit is much thicker in the western part of the basin, as suggested by the minimum thickness of 213 m at Palikea ridge, then this volume could be much larger.

Isotopic compositions of the breccia suggest that its source region in the cliffs or highlands to the west contains lavas with isotopic compositions similar to those of east

Kauaī tholeiites, and distinct from those of west Kauaī tholeiites (Fig. 35). The hawaiite clasts in the breccia also require that somewhere in these cliffs and highlands there is (or was) a large volume of hawaiitic lava that has not been recognized. The volume of hawaiitic lavas in this source region is probably much larger than the volume represented by the two hawaiite flows recognized by Clague & Dalrymple (1988) at the tops of the Olokele and Makaweli members.

The clasts of alkali gabbro in the breccia also suggest a somewhat unusual source region for this breccia. Approximately 50% of the clasts in the breccia layer in the basin and in the Palikea ridge are gabbroic (Fig. 31). Many have diktytaxitic or open-miarolytic structures. These textures are not typical of Hawaiīan lava flows. MacDonald et al. (1960) reported that pebbles of fine-grained gabbro are common in several stream beds on Kauaī, but that few corresponding intrusive bodies have been found. The gabbros described by MacDonald et al. most commonly are petrographically very similar to those in the Lihue basin breccia, showing diktytaxitic textures, and containing phases typical of alkalic volcanics, consisting predominantly of plagioclase (labradorite to andesine), with clinopyroxene, magnetite, ilmenite, apatite, alkali feldspar and rare olivine.

Several small intrusive bodies of alkali gabbro near Puu Lua, on the west rim of Waimea Canyon, provide a possible analogue for the source region of the gabbroic clasts of the breccia. Gabbro samples from these plugs are very similar to the alkali gabbro clasts within the Lihue basin breccia (Fig. 37). They are grey, fine- to medium-grained granular gabbros with diktytaxitic textures, consisting chiefly of plagioclase and clinopyroxene, with lesser amounts of opaque phases and alkali feldspar. One or more intrusive bodies of alkali gabbro, similar to those at Puu Lua, in the cliffs or central massif west of the Lihue basin could be a source of the alkali gabbro clasts in the Lihue basin breccia. The abundance of fine-grained hawaiitic clasts in association with the alkali gabbros also suggests that the source region(s) of the clasts (but not the tholeiitic matrix) consisted of lavas and intrusives of the post-shield alkalic stage of the Waimea Canyon Basalt. The

textures of the alkali gabbros also resemble textures of magmas that cooled slowly in lava lakes (e.g., Helz et al., 1989). Instead of or in addition to intrusive bodies, the source region for the hawaiite and alkali gabbro clasts may be one or more calderas or pit craters filled with post-shield stage alkalic lavas in the steep cliffs and highlands west of the Lihue basin.

CONCLUSIONS

Samples from drillholes within the Lihue basin and adjacent areas of eastern Kauaï provide a variety of constraints on the distribution and evolution of late-stage post-shield and post-erosional alkalic magmatism on Kauaï. Regional stratigraphic-geochemical trends within >300 m of Koloa post-erosional lavas in the basin indicate a gradual decrease in the extent of partial melting of mantle sources during the post-erosional stage. Hawaiite, mugearite, and differentiated alkalic basalt lavas overlying tholeiites of the Napali member in the bottom of the basin indicate a more voluminous and widespread post-shield alkalic stage of volcanism on Kauaï than previously recognized. The presence of these lavas at the bottom of the basin also indicate an origin of the Lihue basin by structural collapse, not fluvial erosion. Several 25-70 m thick breccia layers within the basin and a correlative breccia layer at least 213 m on the western margin of the basin represent large (~ 5 km³) deposits from debris flows derived from the central massif of the island. Compositions and petrographic textures of samples from this breccia reflect the presence of significant volumes of post-shield alkalic magmatic products, and one or more large intrusive bodies or calderas comprising alkali gabbro and associated hawaiite lava flows, within the island's massif west of the Lihue basin.

Table 5 (continued).

sample name	depth (m)	lithology	SiO ₂	Al ₂ O ₃	Fe ₂ O ₃ *	Cr ₂ O ₃	MgO	CaO	MnO	Na ₂ O	K ₂ O	TiO ₂	P ₂ O ₅
91TT2980	266.2-269.7	Kolua	44.05	10.41	16.23	0.18	15.35	10.52	0.21	0.73	0.34	1.71	0.22
91TT2990	271.3-272.8	Kolua	44.27	10.47	16.40	0.16	15.54	9.88	0.18	0.63	0.35	1.76	0.19
91TT2905	273.8-277.4	Kolua	44.63	12.08	15.60	0.13	12.41	10.99	0.19	1.21	0.50	2.03	0.23
91TT2915	278.9-280.4	Kolua	44.94	13.04	15.05	0.07	11.13	11.02	0.16	1.53	0.54	2.18	0.30
91TT2925	281.9-283.5	Kolua	44.94	12.89	14.75	0.11	11.93	10.48	0.19	1.64	0.61	2.16	0.30
91TT2935	285.0-286.5	Kolua	44.40	11.80	15.70	0.10	13.97	9.68	0.21	1.27	0.55	1.98	0.26
91TT2940	289.6-291.1	Kolua	44.86	12.08	14.75	0.10	15.54	10.24	0.21	1.26	0.60	2.06	0.28
91TT2948	292.6-294.1	Kolua	43.92	11.36	15.10	0.11	16.28	9.17	0.20	1.04	0.56	1.98	0.26
91TT2975	297.2-298.7	Kolua	44.11	11.88	14.48	0.12	14.67	10.43	0.20	1.15	0.55	2.11	0.30
91TT2980	298.7-300.2	Kolua	43.90	11.66	14.97	0.11	14.80	10.36	0.21	1.06	0.51	2.12	0.30
91TT2985	300.2-301.8	Kolua	44.33	12.13	14.53	0.11	14.29	10.16	0.20	1.23	0.60	2.12	0.31
91TT2990	301.8-303.3	Kolua	44.20	13.19	15.36	0.12	11.31	10.92	0.20	1.26	0.65	2.52	0.32
91TT2995	303.3-304.8	Kolua	44.39	12.82	14.94	0.10	11.54	11.19	0.20	1.29	0.69	2.50	0.34
91TT21000	304.8-306.3	Kolua	44.34	11.70	14.20	0.09	14.47	10.57	0.20	1.36	0.63	2.14	0.31
Palikea ridge													
97PRQKP2		tholeiite (matrix)	49.41	13.33	13.25	0.07	12.21	6.93	0.19	1.30	0.52	2.50	0.29
97PRQKP5		alkali gabbro (clast)	47.56	15.78	12.57	0.01	5.74	9.68	0.11	2.58	1.18	3.77	0.71
97PRQKP6		basanite (clast)	40.32	17.19	11.30	0.04	4.17	7.25	0.17	3.73	2.18	2.61	1.05

Note: All major element oxides reported as weight % volatile free. FeO* is total iron.

Table 6. Isotopic compositions of Lihue basin and Waimea Canyon Basalt samples

Sample locality	Sample name	lithology/formation	$^{87}\text{Sr}/^{86}\text{Sr}$	2 σ	$^{143}\text{Nd}/^{144}\text{Nd}$	2 σ	ϵ_{Nd}
HTZ drillhole	95HTZ265	breccia (Palikea)	0.703709	8	0.512912	8	5.34
	95HTZ290	breccia (Palikea)	0.703748	8	0.512929	13	5.67
	95HTZ315	breccia (Palikea)	0.703792	8	0.512939	6	5.88
	95HTZ335	breccia (Palikea)	0.703770	8	0.512921	9	5.52
Wiliwili Camp	94PRMK56	tholeiite (Makaweli)	0.703699	8	0.512942	6	5.93
Puu Kee	94PRNP24	tholeiite (Napali)	0.703710	8	0.512943	7	5.94
Nonou Ridge	94PRNP33	tholeiite (Napali)	0.703826	8	0.512899	8	5.10
	94PRNP34	tholeiite (Napali)	0.703890	8	0.512889	8	4.89
Haena dry cave	94PRNP17	tholeiite (Napali)	0.703569	9	0.513001	7	7.08
Hanalei	94PRNP16	tholeiite (Napali)	0.703623	8	0.512956	8	6.21

Notes: Isotopic analyses performed at University of Washington, using procedures described in Nelson (1995). Subsamples analyzed for isotopes were leached for 2 hours in 6.2 N HCl in an ultrasonic bath to avoid weathering effects on Sr- and Nd-isotope compositions. ϵ_{Nd} is deviation of $^{143}\text{Nd}/^{144}\text{Nd}$ from that of inferred bulk earth (0.512638): $\epsilon_{\text{Nd}} = [(^{143}\text{Nd}/^{144}\text{Nd})_{\text{sample}}/0.512638 - 1] \times 10^4$. Analytical error (2 σ) of isotopic analyses is +/- in last digit of ratio. Long-term reproducibility of Sr and Nd isotopic measurements are 41 ppm and 26 ppm (2 σ), respectively. NBS 987 yields an average $^{87}\text{Sr}/^{86}\text{Sr} = 0.710266$ (n=85 over 2 yrs.) and La Jolla Nd averages $^{143}\text{Nd}/^{144}\text{Nd} = 0.511841$ (n=34 over 2 yrs.).

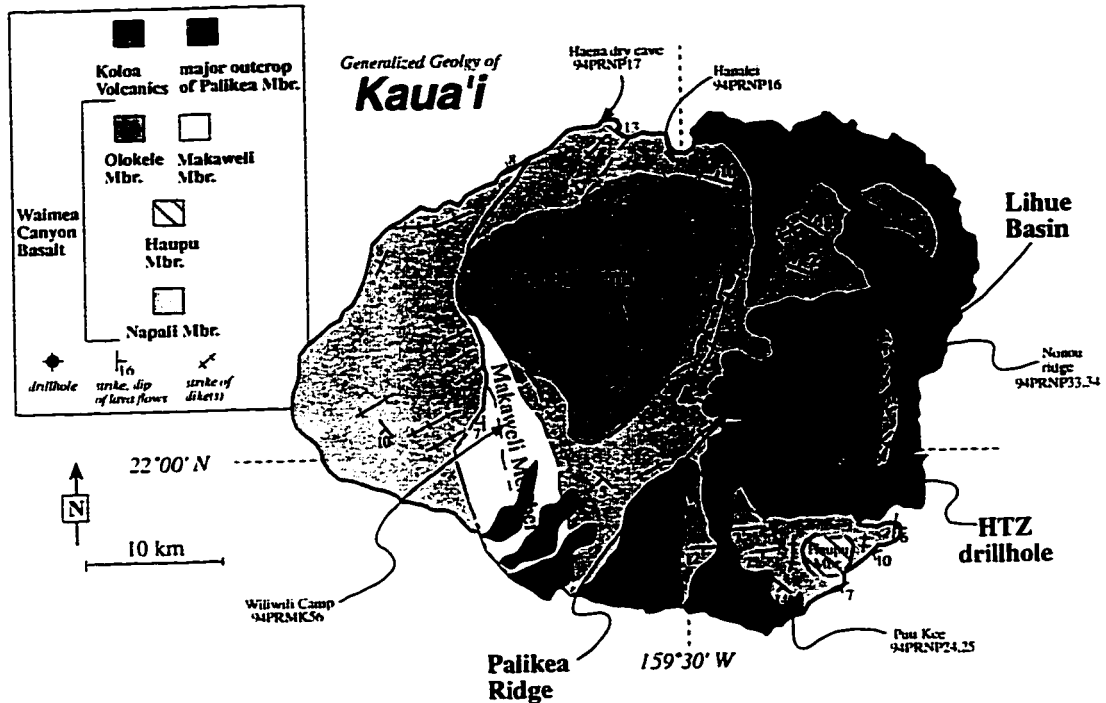


Figure 29. Generalized geologic map of Kaua'i.

Map adapted from MacDonald et al., 1960; Clague & Dalrymple, 1988, showing the primary lithologies and locations of the drillholes and other sample locations in and around the Lihue basin. The main shield and post-shield alkalic stage volcanics are termed the Waiimea Canyon Basalt, and include the Napalai member tholeiitic lavas, and the ponded lavas of the Olokele, Makaweli, and Haupu members. The Haupu member is defined as tholeiitic lavas ponded within a small caldera in the southeast part of the island. The Olokele and Makaweli members are dominantly tholeiites, with at least three hawaiite and mugearite flows in the uppermost sections. Lavas of the Olokele member form a high, erosion-resistant plateau, in some places bounded by faults, and have been interpreted as the remnants of a central caldera. Lavas of the Makaweli member have flowed from the northeast, down into a graben-like valley, where they ponded (MacDonald et al., 1960). The post-erosional Koloa Volcanics are mainly restricted to the central and eastern parts of the island, although a few flows are found in the western parts. They reach great thicknesses in the eastern part of the island, especially in the Hanalei river valley and in the Lihue basin. A generalized cross-section through the trace of A to A' is shown in Figure 34.



Figure 30. Landsat MSS image of Kaua'i.

Landsat MultiSpectral Scanner image of Kaua'i taken in 1978, provided courtesy of NASA's Virtually Hawaii project, sponsored by the Hawaii Space Grant Consortium. The flat, low-lying, semi-circular area on the eastern side of the island is the Lihue basin. The high cliffs on the western margin of the basin are the eastern side of the island's central massif, including the peaks of Kawaikini and Waialeale. The large post-erosional volcanic vent, Kilohana shield (or crater, as it is called here), can be seen in the middle of the Lihue basin. Also note the two small ridges on the eastern margin of the basin (Kalepa and Nonou ridges), the Ha'upu ridge to the south, and the Makaleha mountains, with the summit plateau, to the north of the basin.

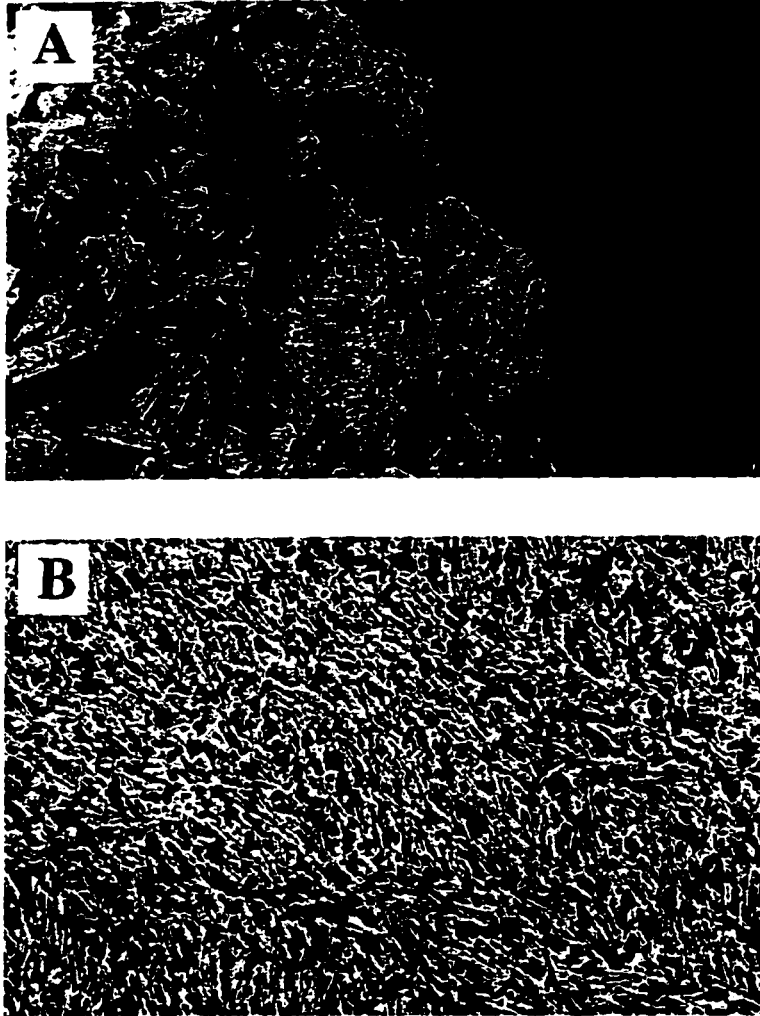


Figure 31. Photomicrographs of breccia samples from the Lihue basin and Palikea ridge.

Horizontal field of view in all images is 4 mm. **A.** Matrix and clasts within breccia sample from Palikea ridge. Light colored matrix is in center of image, consisting of very fine-grained clasts and clay minerals. Fine-grained gabbroic clast is on left side of image; phases are plagioclase, clinopyroxene, olivine, and oxides. Fine-grained clast with trachytic texture is on right side, consisting of lineated plagioclase crystals in an extremely fine-grained matrix. Analyses of larger clasts from the Palikea breccia with similar textures as these smaller clasts, the gabbroic clast is probably alkali gabbro and the trachytic texture clast is hawaiiite. **B.** Hawaiiite clast (sample 97PRQKP6, Table 5) from Palikea ridge. Note excellent alignment of lath-shaped plagioclase feldspars. Phases are plagioclase, clinopyroxene, oxides, and apatite.

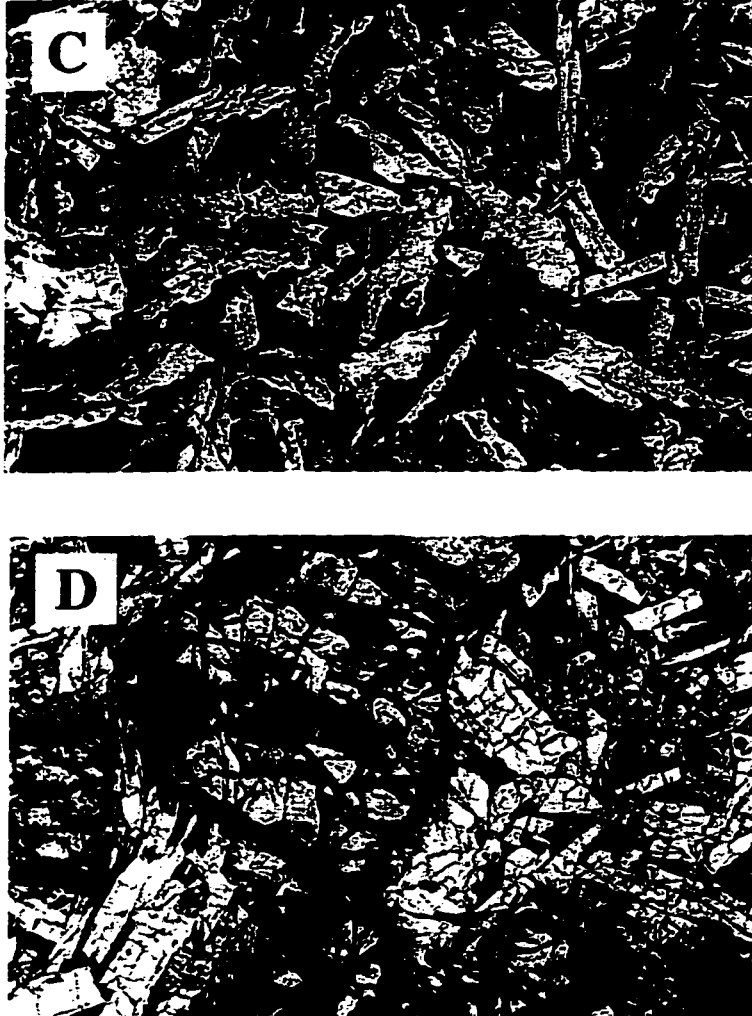


Fig. 31 (continued). **C.** Alkali gabbro clast from Palikea ridge. Note lack of fine-grained matrix. Phases are plagioclase, clinopyroxene, oxides, and apatite. **D.** Gabbroic clast from HTZ drillhole. Phases are plagioclase, olivine, clinopyroxene, and oxides.

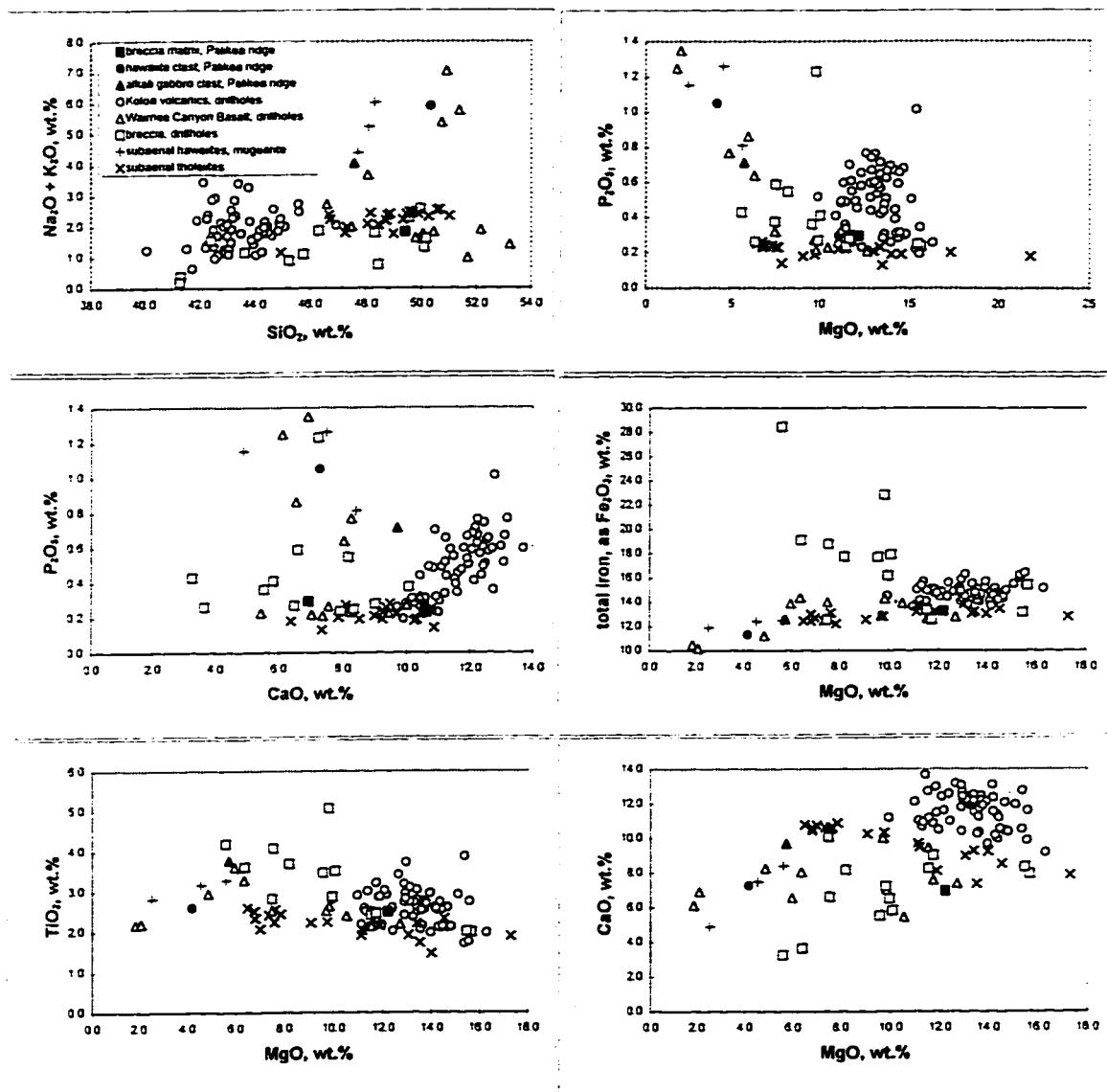


Figure 32. Major-element compositions of samples from Palikea ridge and the Lihue basin drillholes.

Also shown are compositions of Kaua'i tholeiites, two hawaiites, and one mugearite from the literature (Clague & Dalrymple, 1988; MacDonald & Katsura, 1964; MacDonald et al., 1960). Samples from the Lihue basin drillholes of this study are subdivided into Koloa Volcanics, Waimea Canyon Basalt (including tholeiites, hawaiites, differentiated alkali basalts, and one mugearite), and the breccia layer (which correlates with the Palikea ridge breccia). Some of the breccia samples from the drillholes have unusual compositions (high Fe_2O_3 , TiO_2 , and low SiO_2 , CaO) that reflect extensive weathering.

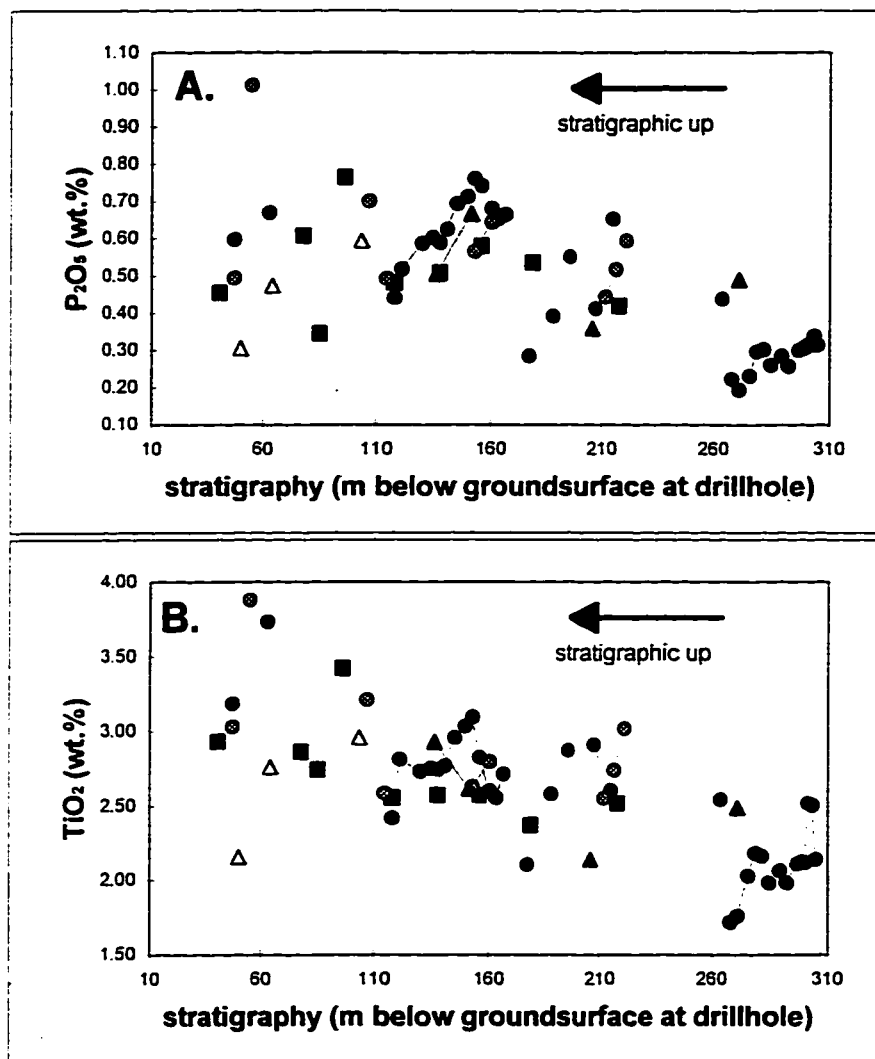


Figure 33. P_2O_5 and TiO_2 versus stratigraphic position for Koloa lavas in each drillhole.

P_2O_5 (A.) and TiO_2 (B.) versus stratigraphic position (depth below ground surface) for Koloa lavas from each drillhole. Symbols are: black circles, HTZ; black triangles, NEK; grey circles, PKR; black squares, SW; white triangles, NWK. Samples that appear to be from the same flow or similar flows, without interbedded alluvium or sediments, are joined by solid lines. There is an overall increase in P_2O_5 and TiO_2 concentrations in Koloa lavas in all of the drillhole samples, from bottom to top of the basin.

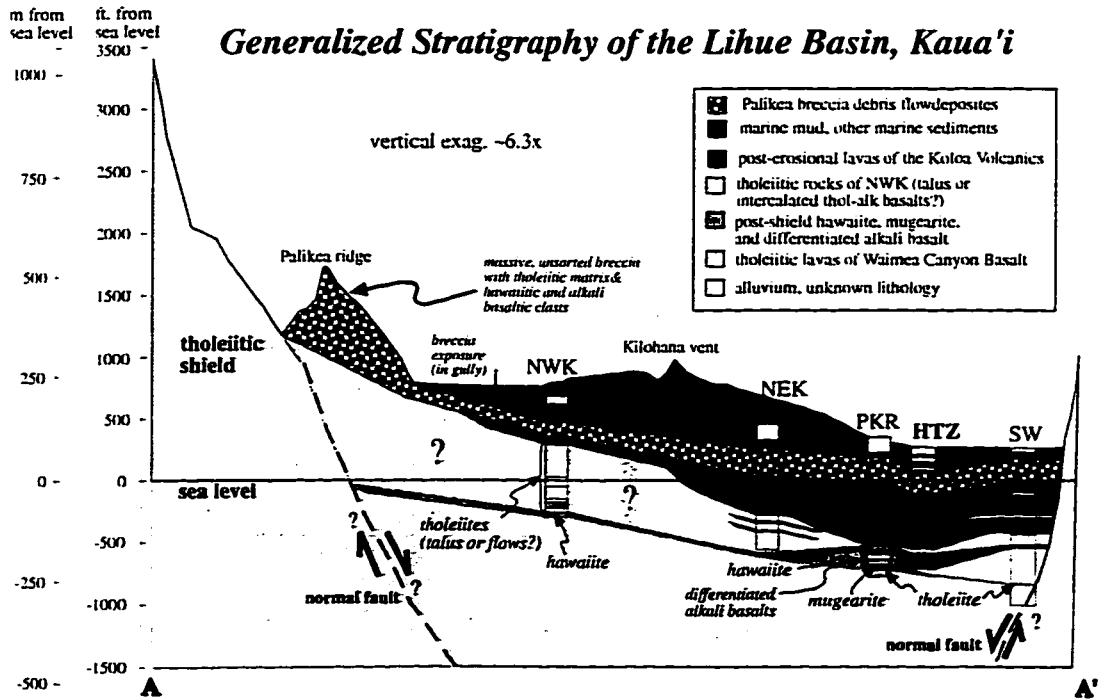


Figure 34. Generalized stratigraphic section of the Lihue basin.

Cross-section is through the trace A-A' in Figure 29, and is based on surface outcrops and drillhole samples. See text for discussion.

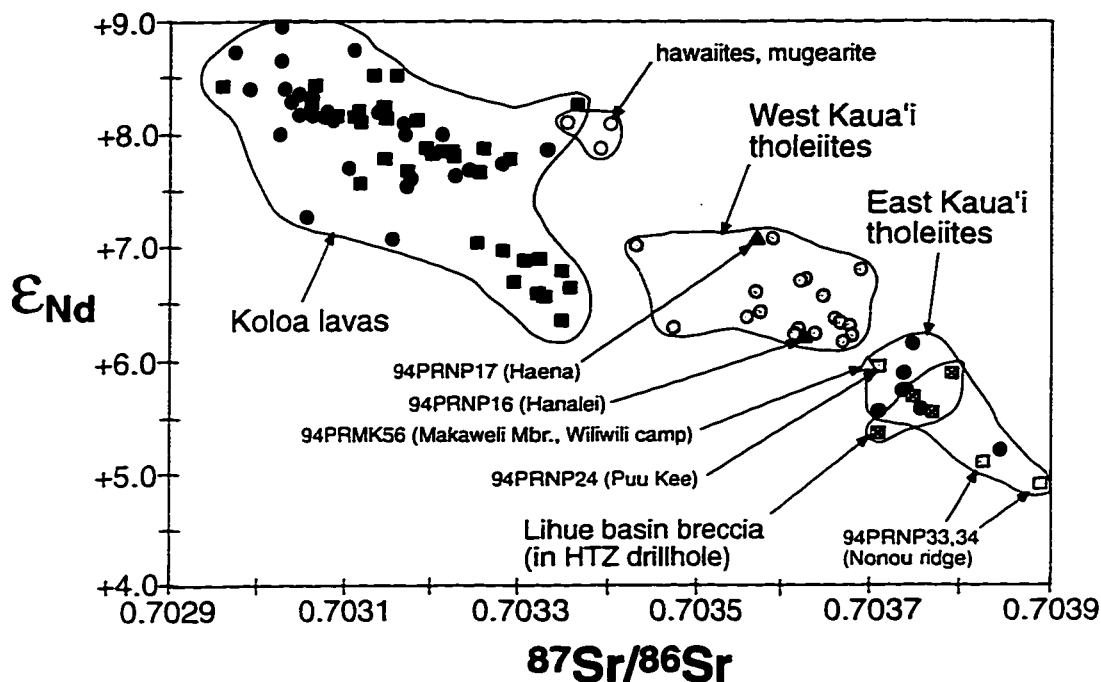


Figure 35. Sr- and Nd- isotope compositions of Kaua'i lavas.

Koloa field includes data from the literature (black circles) (Park, 1990; Maaløe et al., 1992, Clague & Dalrymple, 1988; Feigenson, 1984; Chapter 2) and from the Koloa lavas of the HTZ drillhole (black squares) (Chapter 2). Hawaiite and mugearite data (open circles) are from the three flows identified and analyzed by Clague & Dalrymple (1988) in the upper Olokele and Makaweli members. West Kaua'i (grey circles) and East Kaua'i (black circles) tholeiite data fields are from the literature (Holcomb et al., in press; Park, 1990; Feigenson, 1984 (with reinterpretations of Clague & Dalrymple, 1988); Stille et al., 1986; White & Hoffman, 1982). Tholeiitic lavas from the north and west sides of Kaua'i (Haena and Hanalei) plot in the West Kaua'i field. Samples from the east side of Kaua'i (Puu Kee and Nonou ridge) plot in the East Kaua'i field. The tholeiite from the lower Makaweli member, collected at Wiliwili camp in Waimea Canyon, has isotopic compositions intermediate between the West and East Kaua'i fields. Bulk breccia samples from the HTZ drillhole plot in the East Kaua'i field, suggesting that the source of the breccia contained lavas with isotopic compositions similar to East, not West, Kaua'i.

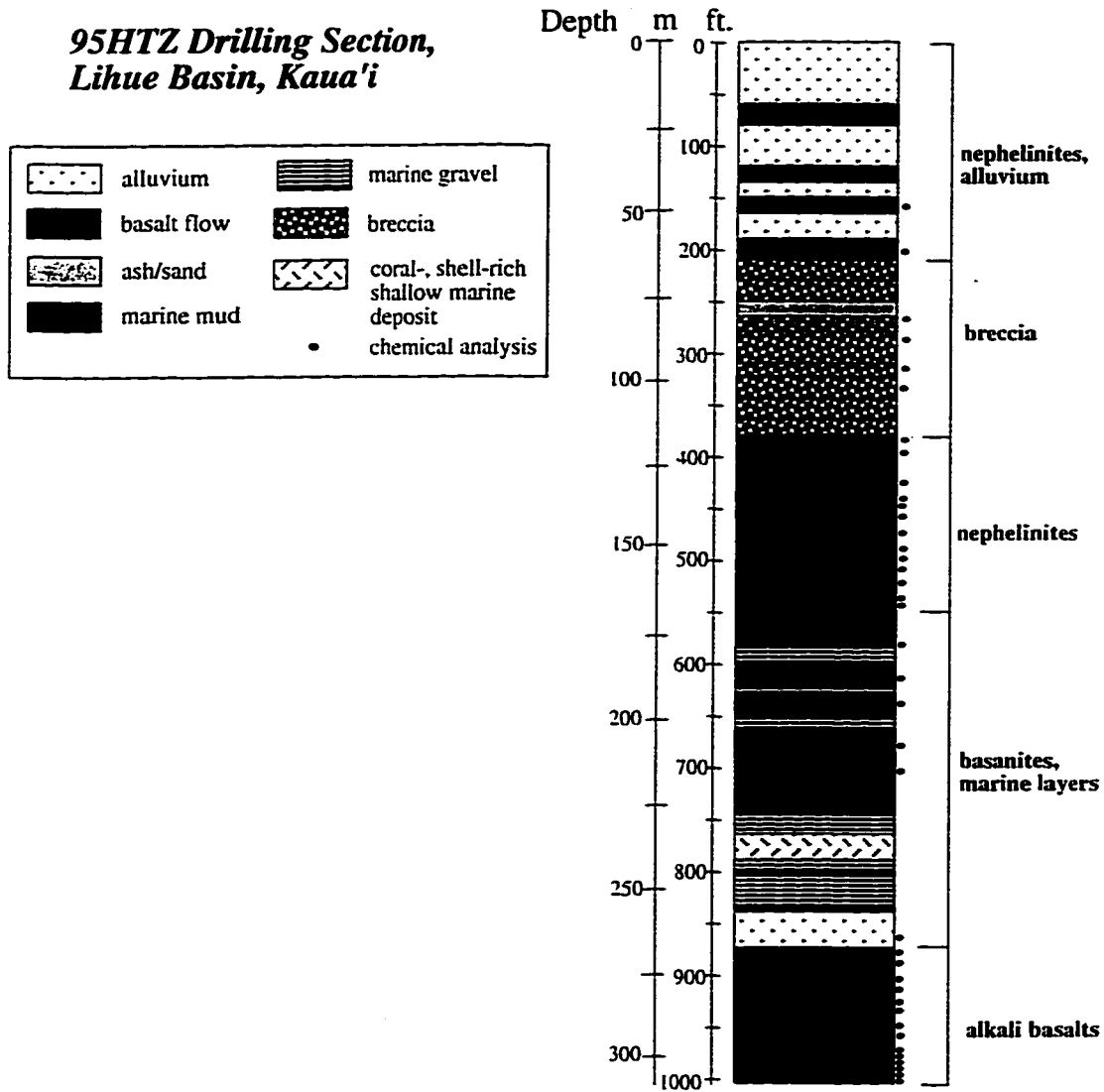


Figure 36. Detailed stratigraphy of the HTZ drillhole, Lihue basin.

There is an overall trend in lithology of Koloa lavas, from bottom to top, of alkali basalts, basanites, to nephelinites. The fact that other drillholes show the same stratigraphic trend in P_2O_5 and TiO_2 as the HTZ drillhole (Fig. 33) suggests that this lithologic sequence may be present in other drillholes as well, and possibly basin-wide.



Figure 37. Photomicrograph of alkali gabbro from one of the intrusive bodies at Puu Lua, on the west rim of Waimea Canyon.

Horizontal field of view is 4 mm. Gabbro samples from these plugs are very similar to the alkali gabbro clasts within the Lihue basin breccia (Fig. 31), and provide a possible analogue for the source region of the breccia. Phases are plagioclase, clinopyroxene, olivine, and oxides.

BIBLIOGRAPHY

- Alibert, C., Michard, A., & Albarede, F., 1983. The transition from alkali basalts to kimberlites: Isotope and trace element evidence from melilitites. *Contributions to Mineralogy and Petrology* **82**: 176-186.
- Baker, J. & Spiegelman, M., 1995. Modelling an infiltration-driven geochemical front. *Earth and Planetary Science Letters* **136**: 87-96.
- Bargar, K.E. & Jackson, E.D., 1974. Calculated volumes of individual shield volcanoes along the Hawaiian-Emperor chain, U.S. Geological Survey *Journal of Research*, **2**: 545-550.
- Bodinier, J.L., Dupuy, C., & Dostal, J., 1988. Geochemistry and petrogenesis of Eastern Pyrenean peridotites. *Geochimica et Cosmochimica Acta* **52**: 2893-2907.
- Bodinier, J.L., Vasseur, G., Vernieres, J., Dupuy, C., & Fabries, J., 1990. Mechanisms of mantle metasomatism: Geochemical evidence from the Lherz orogenic peridotite. *Journal of Petrology* **31**: 597-628.
- Bowan, J.R., Willett, S.D., & Cook, S.J., 1994. Oxygen isotopic transport and exchange during fluid flow: One-dimensional models and applications. *American Journal of Science* **294**: 1-55.
- Brearley, M. & Scarfe, C.M., 1986. Dissolution rates of upper mantle minerals in an alkalic basalt melt at high pressure: An experimental study and implications for ultramafic xenolith survival. *Journal of Petrology* **27**: 1157-1182.
- Carracedo, J.C., 1994. The Canary Islands: An example of structural control on the growth of large oceanic-island volcanoes. *Journal of Volcanology and Geothermal Research* **60**: 225-241.
- Carracedo, J.C., 1996. Morphological and structural evolution of the western Canary Islands: Hotspot-induced three-armed rifts or regional tectonic trends?. *Journal of Volcanology and Geothermal Research* **72**: 151-162.

- Chen, C.-Y. & Frey, F.A., 1983. Origin of Hawaiian tholeiite and alkalic basalt. *Nature* **302**: 785-789.
- Chen, C.-Y. & Frey, F.A., 1985. Trace element and isotopic geochemistry of lavas from Haleakala Volcano, East Maui, Hawaii: Implications for the origin of Hawaiian basalts. *Journal of Geophysical Research* **90**: 8743-8768.
- Clague, D.A., 1987. Hawaiian alkaline volcanism. In: Fitton, J.G. & Upton B.G.J. (eds) *Alkaline Igneous Rocks. Geological Society Special Publication* **30**: 227-252.
- Clague, D.A. & Dalrymple, G.B., 1988. Age and petrology of alkalic postshield and rejuvenated-stage lava from Kauai, Hawaii. *Contributions to Mineralogy and Petrology* **99**: 202-218.
- Clague, D.A. & Frey, F.A., 1982. Petrology and trace element geochemistry of the Honolulu volcanics, Oahu: Implications for the oceanic mantle below Hawaii. *Journal of Petrology* **23**: 447-504.
- Cohen, A.S., O'Nions, R.K., & Kurz, M.D., 1996. Chemical and isotopic variations in Mauna Loa tholeiites. *Earth and Planetary Science Letters* **143**: 111-124.
- Dana, J.D., 1849. *Geology: U.S. Exploring Expedition Report*, v. **10**, 756 pp.
- DePaolo, D.J., 1981. Trace element and isotopic effects of combined wallrock assimilation and fractional crystallization. *Earth and Planetary Science Letters* **53**: 189-202.
- Edwards, B.R. & Russell, J.K., 1996. A review and analysis of silicate mineral dissolution experiments in natural silicate melts. *Chemical Geology* **130**: 233-245.
- Feigenson, M.D, 1984. Geochemistry of Kauai volcanics and a mixing model for the origin of Hawaiian alkali basalts. *Contributions to Mineralogy and Petrology* **87**: 109-119.
- Frey, F.A., 1980. The origin of pyroxenites and garnet pyroxenites from Salt Lake Crater, Oahu, Hawaii: Trace element evidence. *American Journal of Science* **280-A**: 427-449.

- Frey, F.A., Green, D.H., & Roy, S.D., 1977. Integrated models of basalt petrogenesis: A study of quartz tholeiites to olivine melilitites from South Eastern Australia utilizing geochemical and experimental petrological data. *Journal of Petrology* **19**: 463-513.
- Frey, F.A. & Roden, M.F., 1987. The Mantle source for the Hawaiian Islands: Constraints from the lavas and ultramafic inclusions. In: Menzies, M (ed) *Mantle Metasomatism*. London: Academic Press, 423-463.
- Gast, P.W., 1968. Trace element fractionation and the origin of tholeiitic and alkaline magma types. *Geochimica et Cosmochimica Acta* **32**: 1057-1086.
- Ghiorso, M.S. & Sack, R.O., 1995. Chemical Mass Transfer in Magmatic Processes. IV. A Revised and Internally Consistent Thermodynamic Model for the Interpolation and Extrapolation of Liquid-Solid Equilibria in Magmatic Systems at Elevated Temperatures and Pressures. *Contributions to Mineralogy and Petrology* **119**: 197-212
- Gillot, P.-Y., Lefèvre, J.-C., and Nativel, P.-E., 1994. Model for the structural evolution of the volcanoes of Réunion Island. *Earth and Planetary Science Letters* **122**: 291-302.
- Godard, M., Bodinier, J.-L., & Vasseur, G., 1995. Effects of mineralogical reactions on trace element redistributions in mantle rocks during percolation processes: A chromatographic approach. *Earth and Planetary Science Letters* **133**: 449-461.
- Green, D.H., & Ringwood, A.E., 1967. The genesis of basaltic magmas. *Contributions to Mineralogy and Petrology* **15**: 103-190.
- Green, T.H., 1994. Experimental studies of trace-element partitioning applicable to igneous processes--Sedona 16 years later. *Chemical Geology* **117**: 1-36.
- Greenrough, J.D., 1988. Minor phases in the earth's mantle: Evidence from trace- and minor-element patterns in primitive alkaline magmas. *Chemical Geology* **69**: 177-192.

- Halliday, A.N., Lee, D.-C., Tommasini, S., Davies, G.R., Paslick, C.R., Fitton, J.G., & James, D.E., 1995. Incompatible trace elements in OIB and MORB and source enrichment in the sub-oceanic mantle. *Earth and Planetary Science Letters* **133**: 379-395.
- Harris, P.G., 1957. Zone refining and the origin of potassic basalts. *Geochimica et Cosmochimica Acta* **12**: 195-208.
- Hart, S.R., Hauri, E.H., Oschmann, L.A., & Whitehead, J.A., 1992. Mantle plumes and entrainment: Isotopic evidence. *Science* **256**: 517-520.
- Hart, S.R., 1993. Equilibration during mantle melting: A fractal tree model. *Proceedings of the National Academy of Sciences* **90**: 11914-11918.
- Hauri, E.H. & Hart, S.R., 1994. Constraints on melt migration from mantle plumes: A trace element study of peridotite xenoliths from Savai'i, Western Samoa. *Journal of Geophysical Research* **99**: 24301-24321.
- Hauri, E.H., Lassiter, J.C., & DePaolo, D.J., 1996. Osmium isotope systematics of drilled lavas from Mauna Loa, Hawaii. *Journal of Geophysical Research* **101**: 11793-11806.
- Helz, R.T., Kirschenbaum, H., and Marinenko, J.W., 1989. Diapiric transfer of melt in Kilauea Iki lava lake, Hawaii: A quick, efficient process of igneous differentiation. *Geological Society of America Bulletin* **101**: 578-594.
- Hinds, N.E.A., 1930. The geology of Kauai and Niihau. *Bulletin of the B.P. Bishop Museum*, v. **71**, 103 pp.
- Hirschmann, M.M. & Stolper, E., 1996. A possible role for garnet pyroxenite in the origin of the "garnet signature" in MORB. *Contributions to Mineralogy and Petrology* **124**: 185-208.
- Hofmann, A., 1972. Chromatographic theory of infiltration metasomatism and its application to feldspars. *American Journal of Science* **272**: 69-90.
- Hofmann, A.W., 1997. Mantle geochemistry: The message from oceanic volcanism. *Nature* **385**: 219-229.

- Hofmann, A.W. & Hart, S.R., 1978. An assessment of local and regional isotopic equilibrium in the mantle. *Earth and Planetary Science Letters* **38**: 44-62.
- Holcomb, R.T., Reiners, P.W., Nelson, B.K., and Anders, N.-L., Isotopic evidence for two shield volcanoes on the island of Kaua'i, Hawai'i. *Geology*. In press.
- Irving, A.J., 1980. Petrology and geochemistry of composite ultramafic xenoliths in alkalic basalts and implications for magmatic processes within the mantle. *American Journal of Science* **280-A**: 389-426.
- Iwamori, H., 1993a. A model for disequilibrium mantle melting incorporating melt transport by porous and channel flows. *Nature* **366**: 734-737.
- Iwamori, H., 1993b. Dynamic disequilibrium melting model with porous flow and diffusion-controlled chemical equilibration. *Earth and Planetary Science Letters* **114**: 301-313.
- Jin, Z.-M., Green, H.W., & Zhou, Y., 1994. Melt topology in partially molten mantle peridotite during ductile deformation. *Nature* **372**: 164-167.
- Kay, R.W. & Gast, P.W., 1973. The rare earth content and origin of alkali-rich basalts. *Journal of Geology* **81**: 653-682.
- Kelemen, P.B., 1986. Assimilation of ultramafic rock in subduction-related magmatic arcs. *Journal of Geology* **94**: 829-843.
- Kelemen, P.B. & Dick, H.J.B., 1995. Focused melt flow and localized deformation in the upper mantle: Juxtaposition of replacive dunite and ductile shear zones in the Josephine peridotite, SW Oregon. *Journal of Geophysical Research* **100**: 423-438.
- Kelemen, P.B., Dick, H.J.B., & Quick, J.E., 1992. Formation of harzburgite by pervasive melt/rock reaction in the upper mantle. *Nature* **358**: 635-641.
- Kelemen, P.B., Shimizu, N., & Salters, V.J.M., 1995a. Extraction of mid-ocean-ridge basalt from the upwelling mantle by focused flow of melt in dunite channels. *Nature* **375**: 747-753.

- Kelemen, P.B., Whitehead, J.A., Aharonov, E., & Jordahl, K.A., 1995b. Experiments on flow focusing in soluble porous media, with applications to melt extraction from the mantle. *Journal of Geophysical Research* **100**: 475-496.
- Krivoy, H.L., Baker, M., Jr., and Moe, E.E., 1965. A reconnaissance gravity survey of the Island of Kauai, Hawaii. *Pacific Science* **19**: 354-360.
- Langenheim, V.A.M. & Clague, D.A., 1987. The Hawaiian-Emporer Volcanic chain Part II. Stratigraphic framework of volcanic rocks of the Hawaiian Islands, U.S. Geological Survey Professional Paper **1350**: 55-84.
- Liang, Y. & Elthon, D., 1990. Geochemistry and petrology of spinel lherzolite xenoliths from Xalapasco de La Joya, San Luis Potosi, Mexico: Partial melting and mantle metasomatism. *Journal of Geophysical Research* **95**: 15859-15877.
- Lundstrom, C.C., Gill, J., Williams, Q., & Perfit, M.R., 1995. Mantle melting and basalt extraction by equilibrium porous flow. *Science* **270**: 1958-1961.
- Maaløe, S., James, D., Smedley, P., Petersen, S., & Garmann, L.B., 1992. The Koloa volcanic suite of Kauai, Hawaii. *Journal of Petrology* **33**: 761-784.
- MacDonald, G.A., Abbott, A.T., and Peterson, F.L., 1983. *Volcanoes in the sea: The geology of Hawaii*, 2nd ed., University of Hawaii Press, Honolulu, 517 pp.
- MacDonald G.A., Davis D.A., and Cox D.C., 1960. Geology and groundwater resources of the island of Kauai, Hawaii. Hawaii Division of Hydrography. Bulletin **13**. 212 pp.
- Macdonald, G.A., and T. Katsura, 1964. Chemical composition of Hawaiian lavas. *Journal of Petrology* **5**: 82-133.
- Macdougall, J.D., 1995. Using short-lived U and Th series isotopes to investigate volcanic processes. *Annual Review of Earth and Planetary Science* **23**: 143-167.
- Marti, J., Ablay, G.J., and Bryan, S., 1996. Comment on "The Canary Islands: An example of structural control on the growth of large oceanic-island volcanoes" by J.C. Carracedo. *Journal of Volcanology and Geothermal Research* **72**: 143-149.

- McDougall, I., 1979. Age of shield-building volcanism of Kauai and linear migration of volcanism in the Hawaiian Island chain, *Earth and Planetary Science Letters* **46**: 31-42.
- McKenzie, D., 1984. The generation and compaction of partially molten rock. *Journal of Petrology* **25**: 713-765.
- McKenzie, D., 1985. ^{234}Th - ^{238}U disequilibrium and the melting processes beneath ridge axes. *Earth and Planetary Science Letters* **72**: 149-157.
- McKenzie, D., 1989. Some remarks on the movement of small melt fractions in the mantle. *Earth and Planetary Science Letters* **95**: 53-72.
- McKenzie, D. & O'Nions, R.K., 1991. Partial melt distributions from inversion of rare earth element concentrations. *Journal of Petrology* **32**: 1021-1091.
- Menzies, M., Kempton, P., & Dungan, M., 1985. Interaction of continental lithosphere and asthenospheric melts below the Geronimo Volcanic Field, Arizona, U.S.A. *Journal of Petrology* **26**: 663-693.
- Moore, J.G., Nomark, W.R., and Holcomb, R.T., 1994. Giant Hawaiian landslides. *Annual Review of Earth and Planetary Science Letters* **22**: 119-144.
- Navon, O. & Stolper, E., 1987. Geochemical consequences of melt percolation: The upper mantle as a chromatographic column. *Journal of Geology* **95**: 285-307.
- Navon, O, Frey, F.A., & Takazawa, E., 1996. Magma transport and metasomatism in the mantle: A critical review of current geochemical models--Discussion. *American Mineralogist* **81**: 754-759.
- Nelson, B.K., 1995. Fluid flow in subduction zones: Evidence from Nd- and Sr-isotope variations in metabasalts of the Franciscan Complex, California. *Contributions to Mineralogy and Petrology* **119**: 247-262.
- Nielson, J.E. & Wilshire, H.G., 1993. Magma transport and metasomatism in the mantle: A critical review of current geochemical models. *American Mineralogist* **78**: 1117-1134.

- Nielson, J.E. & Wilshire, H.G., 1996. Magma transport and metasomatism in the mantle: A critical review of current geochemical models—Reply to Navon et al. *American Mineralogist* **81**: 760-765.
- Park, K.-H., 1990. Strontium, neodymium, and lead isotope studies of ocean island basalts: Constraints on their origin and evolution. Ph.D. dissertation. Columbia University. 252 pp.
- Pfann, W.G., 1952, Principles of zone-melting. *Trans. AIME* **194**: 747-753.
- Pearson, D.G., Davies, G.R., & Nixon, P.H., 1993. Geochemical constraints on the petrogenesis of diamond facies pyroxenites from the Beni Bousera peridotite massif, North Morocco. *Journal of Petrology* **34**: 125-172.
- Richter, F.M., 1986. Simple models for trace element fractionation during melt segregation. *Earth and Planetary Science Letters* **77**: 333-344.
- Richter, F.M. & McKenzie, D., 1984. Dynamical models for melt segregation from a deformable matrix. *Journal of Geology* **92**: 729-740.
- Riley, G.N. Jr. & Kohlstedt, D.L., 1991. Kinetics of melt migration in upper mantle-type rocks. *Earth and Planetary Science Letters* **105**: 500-521.
- Rivalenti, G., Mazzucchelli, M., Vannucci, R., Hofmann, A.W., Ottolini, L., Bottazzi, P., & Obermiller, W., 1995. The relationship between websterite and peridotite in the Balmuccia peridotite massif (NW Italy) as revealed by trace element variations in clinopyroxene. *Contributions to Mineralogy and Petrology* **121**: 275-288.
- Roden, M.F., Frey, F.A., and Clague, D.A., 1984. Geochemistry of tholeiitic and alkalic lavas from the Koolau Range, Oahu, Hawaii: Implications for Hawaiian volcanism. *Earth and Planetary Science Letters* **69**: 141-158.
- Roden, M.F. & Murthy, V.R., 1985. Mantle Metasomatism. *Annual Review of Earth and Planetary Science* **13**: 269-296.
- Roden, M.F., Trull, T., Hart, S.R., and Frey, F.A., 1994. New He, Nd, Pb, and Sr isotopic constraints on the constitution of the Hawaiian plume: Results from Koolau Volcano, Oahu, Hawaii, USA. *Geochimica et Cosmochimica Acta* **58**: 1431-1440.

- Sen, C. & Dunn, T., 1994. Experimental modal metasomatism of a spinel lherzolite and the production of amphibole-bearing peridotite. *Contributions to Mineralogy and Petrology* **119**: 422-432.
- Sen, G., 1983. A petrologic model for the constitution of the upper mantle and crust of the Koolau shield, Oahu, Hawaii, and Hawaiian magmatism. *Earth and Planetary Science Letters* **62**: 215-228.
- Sen, G., 1987. Xenoliths associated with the Hawaiian hot spot. In: Nixon, P.H. (ed) *Mantle Xenoliths*. London: Wiley, 359-375.
- Sen, G., 1988. Petrogenesis of spinel lherzolite and pyroxenite suite xenoliths from the Koolau shield, Oahu, Hawaii: Implications for petrology of the post-eruptive lithosphere beneath Oahu. *Contributions to Mineralogy and Petrology* **199**: 61-91.
- Sen, G., Frey, F.A., Shimizu, N., and Leeman, W.P., 1993. Evolution of the lithosphere beneath Oahu, Hawaii: Rare earth element abundances in mantle xenoliths. *Earth and Planetary Science Letters* **119**: 53-69.
- Sen, G. & Jones, R.E., 1990. Cumulate xenolith in Oahu, Hawaii: Implications for deep magma chambers and Hawaiian volcanism. *Science* **249**: 1154-1157.
- Sen, G. & Leeman, W.P., 1991. Iron-rich lherzolititic xenoliths from Oahu: Origin and implications for Hawaiian magma sources. *Earth and Planetary Science Letters* **102**: 45-57.
- Shaw, H.R., Jackson, E.D., and Bargar, K.E., 1980. Volcanic periodicity along the Hawaiian-Emperor chain. *American Journal of Science* **280-A**: 667-708.
- Sims, K.W.W., DePaolo, D.J., Murrell, M.T., Baldrige, W.S., Goldstein, S.J., & Clague, D.A., 1995. Mechanisms of magma generation beneath Hawaii and mid-ocean ridges: Uranium/Thorium and Samarium/Neodymium isotopic evidence. *Science* **267**: 508-512.
- Spiegelman, M., & Elliott, T., 1993. Consequences of melt transport for uranium series disequilibrium in young lavas. *Earth and Planetary Science Letters* **118**: 1-20.

- Spiegelman, M., 1996. Geochemical consequences of melt transport in 2-D: The sensitivity of trace elements to mantle dynamics. *Earth and Planetary Science Letters* **139**: 115-132.
- Spera, F.J., 1984. Carbon dioxide in petrogenesis III: Role of volatiles in the ascent of alkaline magma with special reference to xenolith-bearing mafic lavas. *Contributions to Mineralogy and Petrology* **88**: 217-232.
- Spera, F.J., 1987. Dynamics of translithospheric migration of metasomatic fluid and alkaline magma. In: Menzies, M. (ed) *Mantle Metasomatism*. London: Academic Press, 1-20.
- Stearns, H.T. & Vaksvik, K.N., 1935. Geology and groundwater resources of the island of Oahu, Hawaii. Hawaii Division of Hydrography. *Bulletin* **1**. 198 pp.
- Stille, P., Unruh, D.M., and Tatsumoto, M., 1986. Pb, Sr, Nd, and Hf isotopic constraints on the origin of Hawaiian basalts and evidence for a unique mantle source. *Geochimica et Cosmochimica Acta* **50**: 2303-2319.
- Sun, S.S. & Hanson, G.H., 1975. Origin of Ross Island basanitoids and limitations upon the heterogeneity of mantle sources for alkali basalts and nephelinites. *Contributions to Mineralogy and Petrology* **52**: 77-106.
- Vasseur, G., Vernieres, J., & Bodinier, J.-L., 1991. Modelling of trace element transfer between mantle melt and heterogranular peridotite matrix. *Journal of Petrology Special Lherzolites Issue*: 41-54.
- Van der Wal, D. & Bodinier, J.-L., 1996. Origin of the recrystallization front in the Ronda peridotite by km-scale pervasive porous melt flow. *Contributions to Mineralogy and Petrology* **122**: 387-405.
- Vollmer, R., 1987. Metasomatism of the continental lithosphere: Simulation of isotope and element abundance behavior and case studies. In: Helgeson, H.C. (ed) *Chemical Transport in Metasomatic Processes*. Hingham, Mass: Reidel, 53-90.

- Weaver, B.L., 1991. The origin of ocean island basalt end-member compositions: Trace element and isotopic constraints. *Earth and Planetary Science Letters*. **104**: 381-397.
- West, H.B. & Leeman, W.P., 1994. The open-system geochemical evolution of alkalic cap lavas from Haleakala Crater, Hawaii, USA. *Geochimica et Cosmochimica Acta* **58**: 773-796.
- White, W.M. & Hofmann, A.W., 1982. Sr and Nd isotope geochemistry of oceanic basalts and mantle evolution. *Nature* **296**: 821-825.

APPENDIX A: MASS-BALANCE INCREMENTAL METHOD

Consider an initially solid column of mantle with density ρ_s , infiltrated with melt with density ρ_f from below. As the melt propagates upwards into the column it establishes porosity ϕ in the column in a way that could be imagined as either melt pushing open voids in the rock, or shouldering aside portions of the solid rock on either side. At any point in the column then, the total concentration of any trace element in the melt-solid system C_m , can be related to the concentrations of the element in the solid C_s , and in the melt C_f by simple mass balance:

$$\left[\rho_f \phi + \rho_s (1 - \phi) \right] C_m = \rho_f \phi C_f + \rho_s (1 - \phi) C_s \quad (\text{A1})$$

The column is divided into a series of finite cells numbered 0 through i , and the melt propagates into and through these cells in a series of finite time steps numbered 0 through j . In each time step, melt propagates forward one cell while the solid remains stationary, so in cell j at time step i the mass balance is:

$$\rho_f \phi_{i-1}^{j-1} C_{f_{i-1}}^{j-1} + \rho_s (1 - \phi_i^{j-1}) C_{s_i}^{j-1} = \rho_f \phi_i^j C_{f_i}^j + \rho_s (1 - \phi_i^j) C_{s_i}^j \quad (\text{A2})$$

If the solid and melt are in trace element equilibrium in each cell, then the trace element concentration in the solid is related to the concentration in the liquid by the solid-melt bulk distribution coefficient D of the element:

$$C_s = DC_f \quad (\text{A3}),$$

so equation A2 becomes

$$\rho_f \phi_{i-1}^{j-1} C_{f_{i-1}}^{j-1} + \rho_s (1 - \phi_i^{j-1}) DC_{f_i}^{j-1} = \rho_f \phi_i^j C_{f_i}^j + \rho_s (1 - \phi_i^j) DC_{f_i}^j \quad (\text{A4}).$$

Solving for the concentration of the element in the melt in cell i and time step j yields:

$$C_{f_i}^j = \frac{\rho_f \phi_{i-1}^{j-1} C_{f_{i-1}}^{j-1} + \rho_s (1 - \phi_i^{j-1}) C_{s_i}^{j-1}}{\rho_f \phi_i^j + \rho_s (1 - \phi_i^j) D} \quad (\text{A5}).$$

This simple equation can be solved for a sequence of cells in a sequence of timesteps to simulate equilibrium transport of melt with an initial concentration C_f , through a column with an initial solid concentration C_s .

The simplest case of reactive transport that can be modeled with this equation is one of purely diffusive exchange in the column with constant ϕ and D (no mineralogic reaction, no change in melt fraction). But this equation also allows for different ϕ and D in different cells and time steps in the reactive column, and thus can be used to simulate mineralogic reaction, via dissolution and reprecipitation and the accompanying reactive exchange, simultaneously with diffusive exchange. In order to satisfy mass balance constraints in models with changing porosity however, porosity changes need to occur uniformly throughout the column at any give time when this model is used. In other words, while the porosity in all cells changes with time, the porosity in each cell in any given timestep is the same.

The isotopic composition of the melt-solid system within any cell can also be calculated using this model, where ε_i^j is the isotopic ratio of an element in cell i in timestep j :

$$\varepsilon_i^j = \frac{\varepsilon_{i-1}^{j-1} \rho_f \phi_{i-1}^{j-1} C_{f_{i-1}}^{j-1} + \varepsilon_{s_i}^{j-1} \rho_s (1 - \phi_i^{j-1}) C_{s_i}^{j-1}}{\rho_f \phi_{i-1}^{j-1} + \rho_s (1 - \phi_i^{j-1}) C_{s_i}^{j-1}} \quad (\text{A6}).$$

This equation was used by Vollmer (1987) in modeling metasomatic processes.

APPENDIX B: CONTINUUM METHOD DERIVATION AND FINITE DIFFERENCE SOLUTION

Another way of modeling reactive transport in a melt-mantle column involves a continuum approach, solved by a finite difference method. This scenario requires the assumption of a column of solid mantle with pre-existing porosity ϕ , already filled with melt in equilibrium with the solid with bulk distribution coefficient D . The total masses of melt and solid must be conserved in any representative elementary volume of this reactive column, although melt and solid can be created or destroyed at an equal and opposite rate r .

Conservation of melt can be written as:

$$\frac{\partial(\phi\rho_f)}{\partial t} + \frac{\partial}{\partial z}(\phi\rho_f v) = -r \quad (\text{B1}),$$

where v is the velocity of melt with respect to the solid. Conservation of solid can be written as:

$$\frac{\partial[(1-\phi)\rho_s]}{\partial t} = r \quad (\text{B2}).$$

Adding these two equation together yields the general conservation of mass statement:

$$\frac{\partial}{\partial t}[\phi\rho_f + (1-\phi)\rho_s] + \frac{\partial}{\partial z}(\phi\rho_f v) = 0 \quad (\text{B3}).$$

With the assumption that a trace element is sufficiently dilute in the solid and melt so that it does not affect mass of the melt or solid, conservation of the trace element can be stated as

$$\frac{\partial}{\partial t} [\phi \rho_f C_f + (1-\phi) \rho_s C_s] + \frac{\partial}{\partial z} (\phi \rho_f v C_f) = 0 \quad (\text{B4}).$$

Using the usual equilibrium assumption $C_s = C_f D$, and defining $\rho = \rho_f / \rho_s$ yields:

$$\frac{\partial}{\partial t} [\phi C_f + (1-\phi) \rho D C_f] + \frac{\partial}{\partial z} (\phi v C_f) = 0 \quad (\text{B5}).$$

Expanding the last term of the left side and rearranging yields:

$$\frac{\partial}{\partial t} [(1-\phi) \rho D C_f] + C_f \left[\frac{\partial \phi}{\partial t} + \frac{\partial (\phi v)}{\partial z} \right] + \phi \left[\frac{\partial C_f}{\partial t} + v \frac{\partial C_f}{\partial z} \right] = 0 \quad (\text{B6}).$$

From equation B3,

$$\frac{\partial \phi}{\partial t} + \frac{\partial}{\partial z} (\phi v) = \rho \frac{\partial \phi}{\partial t} \quad (\text{B7}).$$

Substituting the right-hand side of B7 in for the terms inside the brackets of the middle term of equation B6 and pulling the ρ 's out of the derivatives (assuming constant melt and solid densities) yields:

$$\rho \frac{\partial}{\partial t} [(1-\phi) D C_f] + C_f \rho \frac{\partial \phi}{\partial t} + \phi \left[\frac{\partial C_f}{\partial t} + v \frac{\partial C_f}{\partial z} \right] = 0 \quad (\text{B8}).$$

Applying the chain rule to the first term:

$$\rho(1-\phi) D \frac{\partial C_f}{\partial t} + C_f \rho(1-\phi) \frac{\partial D}{\partial t} - \rho D C_f \frac{\partial \phi}{\partial t} + C_f \rho \frac{\partial \phi}{\partial t} + \phi \left(\frac{\partial C_f}{\partial t} + \frac{\partial C_f}{\partial z} \right) = 0 \quad (\text{B9}),$$

and grouping of terms yields:

$$[\rho(1-\phi)D + \phi] \frac{\partial C_f}{\partial t} + \phi v \frac{\partial C_f}{\partial z} = \rho(\phi-1)C_f \frac{\partial D}{\partial t} + \rho(D-1)C_f \frac{\partial \phi}{\partial t} \quad (\text{B10}),$$

and finally:

$$[\rho(1-\phi)D + \phi] \frac{\partial C_f}{\partial t} + \phi v \frac{\partial C_f}{\partial z} = \rho C_f \left[(\phi-1) \frac{\partial D}{\partial t} + (D-1) \frac{\partial \phi}{\partial t} \right] \quad (\text{B11}).$$

This equation was used by Godard et al. (1995) and Van der Wal & Bodinier (1996) in modeling trace element changes of residual mantle in recrystallization fronts of mantle massifs, and works equally well for simulating flow of melt through reactive solid.

An additional complication arises however, when porosity changes in a column of reactive mantle, such that:

$$\frac{\partial \phi}{\partial t} \neq 0 \quad (\text{B12}).$$

In this case the flux ϕv , must vary spatially in a way given by equation B7,

$$\frac{\partial \phi}{\partial t} + \frac{\partial}{\partial z}(\phi v) = \rho \frac{\partial \phi}{\partial t} \quad (\text{B13}).$$

If $\frac{\partial \phi}{\partial z} \neq 0$ (porosity changes at a single rate in all cells of the column), then equation B7

simplifies to

$$\frac{\partial v}{\partial z} = \frac{(\rho-1)}{\phi} \frac{\partial \phi}{\partial t} \quad (\text{B14}),$$

and the velocity in each cell can be approximated by

$$v = v_0 + zc \left(\frac{\rho - 1}{\phi} \right) \quad (\text{B15}),$$

where $c = \frac{\partial \phi}{\partial t}$ for each time and position in the column.

Numerical solution

A finite difference method is used to solve for the concentration of a trace element in the melt (C_f) in equation B11. Equation B11 is rewritten for simplicity as:

$$k_1 \frac{\partial C_f}{\partial t} + k_2 \frac{\partial C_f}{\partial z} = k_3 C_f \quad (\text{B16}),$$

where

$$k_1 = [\rho(1 - \phi)D + \phi], \quad (\text{B17})$$

$$k_2 = \phi v, \quad (\text{B18}), \text{ and}$$

$$k_3 = \rho \left[(\phi - 1) \frac{\partial D}{\partial t} + (D - 1) \frac{\partial \phi}{\partial t} \right] \quad (\text{B19}).$$

Assume i cells in the column and j timesteps of melt flow and reaction, so that the concentration in the cell to be solved for is c_i^{j+1} . Spatial and temporal gradients in melt concentration are approximated as:

$$\frac{\partial c}{\partial t} = \frac{c_i^{j+1} - \frac{1}{2}(c_{i-1}^j + c_{i+1}^j)}{\Delta t} \quad (\text{B20}), \text{ and}$$

$$\frac{\partial c}{\partial z} = \frac{1}{2} \left[\frac{c_{i+1}^j - c_{i-1}^j}{2\Delta z} + \frac{c_{i+1}^{j+1} - c_{i-1}^{j+1}}{2\Delta z} \right] \quad (\text{B21}),$$

where Δt and Δz are appropriately small increments of time and length. Substituting equations B20 and B21 into equation B11 and rearranging yields

$$c_i^{j+1} = \left(\frac{1}{1 - \frac{k_3}{k_1} \Delta t} \right) \left[\frac{1}{2} (c_{i-1}^j + c_{i+1}^j) - \frac{k_2}{k_1} \frac{\Delta t}{4\Delta z} (c_{i+1}^j - c_{i-1}^j + c_{i+1}^{j+1} - c_{i-1}^{j+1}) \right] \quad (\text{B22}).$$

A similar approach to solving the homogeneous version of equation B11 (the case without changes in ϕ or D) yields a finite difference solution whose results compare well to this solution with $\frac{\partial \phi}{\partial t} = \frac{\partial D}{\partial t} = 0$, and to the analytic solution of Navon & Stolper (1987).

VITA

Peter William Reiners

University of Washington

1997

EDUCATION

- 1991 **B.A.**, Geology, Carleton College, Northfield, Minnesota (Cum Laude, Distinction in department, Distinction on thesis), Thesis: Shocked quartz at the Triassic-Jurassic boundary in Italy, Advisor: David M. Bice
- 1993 **M.S.**, Geological Sciences, University of Washington, Seattle, Thesis: Evidence for multiple mechanisms of crustal contamination of magma from compositionally zoned plutons of the Alaska Range, Alaska, Advisor: Bruce K. Nelson
- 1997 **Ph.D.**, Geological Sciences, University of Washington, Seattle
Dissertation: Reactive melt transport in the mantle and petrogenesis of Hawaiian post-erosional magmas, Advisor: Bruce K. Nelson

HONORS, SCHOLARSHIPS, FELLOWSHIPS

- 1989 NAGT/USGS Field Research Appointment
- 1991-92 Laurence M. Gould Scholar, Carleton College
- 1992 NSF Graduate Research Fellowship Honorable Mention Award
- 1992 Livingston Wernecke Award, University of Washington
- 1994 Peter Misch and David Johnston Fellow, University of Washington
- 1996 Howard Coombs Fellow, University of Washington
- 1997-98 Texaco Postdoctoral Scholar in Geochemistry, California Institute of Technology, Pasadena, California